Geoeffectiveness of interplanetary shocks controlled by impact angles: A review

D. M. Oliveira[a,b,*], A. A. Samsonov[c]

[a] *NASA Goddard Space Flight Center, Greenbelt, MD USA*
[b] *Goddard Planetary Heliophysics Institute, University of Maryland Baltimore County, Baltimore, MD USA*
[c] *Saint Petersburg State University, Saint Petersburg, Russia*

Abstract

The high variability of the Sun's magnetic field is responsible for the generation of perturbations that propagate throughout the heliosphere. Such disturbances often drive interplanetary shocks in front of their leading regions. Strong shocks transfer momentum and energy into the solar wind ahead of them which in turn enhance the solar wind interaction with magnetic fields in its way. Shocks then eventually strike the Earth's magnetosphere and trigger a myriad of geomagnetic effects observed not only by spacecraft in space, but also by magnetometers on the ground. Recently, it has been revealed that shocks can show different geoeffectiveness depending closely on the angle of impact. Generally, frontal shocks are more geoeffective than inclined shocks, even if the former are weaker than the latter. This review is focused on results obtained from modeling and experimental efforts in the last 15 years. Some theoretical and observational background are also provided.

Keywords: Solar disturbances, interplanetary shocks, shock impact angle, geomagnetic activity

Contents

1. Introduction

The Sun is the nearest star to the Earth. As a gigantic sphere of magnetized gas, the Sun is constantly active with large variations in its magnetic field. For example, based on historical and modern observations, it is well known today that the Sun presents a 22-year period of a dynamic solar cycle which corresponds to a double magnetic field reversal of its magnetic field polarity, but the time interval between two consecutive minima or maxima numbers of sunspots existing on the Sun's surface corresponds

*Corresponding author
Email addresses: denny.m.deoliveira@nasa.gov (D. M. Oliveira), a.samsonov@spbu.ru (A. A. Samsonov)

to approximately 11 years. However, these time intervals vary from cycle to cycle (*Eddy*, 1976). This variability of the solar magnetic field controls the flow of an ionized gas named plasma, or a stream of charged particles, from the solar outer atmosphere, or the corona, into the interplanetary space. This stream of particles is called the solar wind which flows away from the Sun in all directions. The first detailed measurements of the solar wind properties were obtained from the Mariner 2 spacecraft (*Neugebauer and Snyder*, 1962), following theoretical predictions by E. N. Parker (see, e.g. *Parker*, 1958, 1961) and previous attempts by other spacecraft. For early references and historical perspectives, see reviews by *Parker* (1999) and *Neugebauer* (2003). While traveling in the interplanetary space, the solar wind encounters several bodies in the solar system, such as planets, moons, comets, asteroids, and many others. Most interesting effects occur when the solar wind interacts with magnetized bodies, such as planetary magnetospheres, in particular the terrestrial magnetosphere (*Tsurutani et al.*, 2011).

During solar maxima, a high variability of the solar magnetic field is often responsible for ejections of plasma from the surface of the Sun, and this plasma carries a great amount of kinetic energy and momentum with it. Since these perturbations have the origin at the solar corona, they are called coronal mass ejections, or CMEs (*Gosling*, 1997; *Webb and Howard*, 2012). CMEs traveling in the interplanetary space generally drive shock waves ahead of their leading edges. These shock waves, or interplanetary (IP) shocks, occur when CME shock speeds with respect to the upstream solar wind are larger than the medium magnetosonic speed (*Kennel et al.*, 1985).

Due to the fact that solar wind streams from different solar regions have different speeds, frequently fast speed streams (associated with coronal holes) push low speed streams (associated with the heliospheric current sheet) generating a compression region between the two streams. This is the cause of the formation of another large scale solar wind perturbation called corotating interacting regions (CIRs), first discovered by *Smith and Wolfe* (1976). The first CIR-driven shock observation was discussed by *Tsurutani et al.* (1982), who were the first to show that particles can be accelerated by shocks. If the relative speed between the fast and slow streams is greater than the local magnetosonic speed, IP shocks can be driven by CIRs as well. However, CIR shocks are more frequently driven in the heliosphere away from the Earth's orbit (see, e.g., *Richter et al.*, 1985; *Tsurutani et al.*, 2006, and references therein).

Impacts of IP shocks on the Earth's magnetosphere are associated with many disturbance effects that can be detected in the geospace and on the ground. The first dramatic effect triggered by IP shock impacts results from abrupt compressions of the magnetosphere/magnetotail leading to intensifications of the Chapman-Ferraro currents, which in turn cause abrupt increases in the horizontal magnetic field measured by magnetometers on the ground. This effect corresponds to the sudden impulse signatures (*Patel and Cahill*, 1974; *Kokubun et al.*, 1977). If the solar wind dynamic pressure increases, a positive jump will be created (SI^+), and if it decreases, a negative jump (SI^-) will be created (see, e.g., *Araki*, 1994). However, when geomagnetic activity followed shock impacts, early researchers thought that a different event was associated with compressions, namely the storm sudden commencement (SSC) (*Chao and Lepping*, 1974; *Smith et al.*, 1986). Moreover, in this paper, we will use the terms SI^+/SI^-, even though the papers here reviewed originally used SSC. For a discussion on the comparison between SI^+/SI^- and SSC, we refer the reader to *Joselyn and Tsurutani* (1990) and *Gonzalez et al.* (1992)..

Strong IP shocks especially with southward IMF (interplanetary magnetic field) preconditions are often followed by intense geomagnetic storms (e.g., *Lugaz et al.*, 2016), but the direct causes of the storms are the occurrence of magnetic reconnection (*Gonzalez and Tsurutani*, 1987; *Tsurutani et al.*, 1992; *Gonzalez et al.*, 1994, 1999, 2007; *Echer et al.*, 2008a,b). Other effects triggered by IP shocks in the magnetosphere-ionosphere-thermosphere system are radiation belt perturbations (*Blake et al.*, 1992; *Hudson et al.*, 1997; *Zong et al.*, 2009; *Horne et al.*, 2013; *Halford et al.*, 2015), heating and upwelling of the highest layers of the Earth's upper atmosphere, or the thermosphere (*Connor et al.*, 2016; *Shi et al.*, 2017; *Oliveira and Silveira*, 2017; *Oliveira et al.*, 2017), triggering of substorms (*Heppner*, 1955; *Schieldge and Siscoe*, 1970; *Kokubun et al.*, 1977; *Akasofu and Chao*, 1980; *Craven et al.*, 1986; *Lyons*, 1995; *Zhou and Tsurutani*, 1999, 2001; *Liou et al.*, 2003; *Tsurutani et al.*, 2008; *Yue et al.*, 2010; *Echer et al.*, 2011), and many others. For example, *Kokubun et al.* (1977) showed that intense auroral activity was triggered by SI^+ events whose amplitudes were larger than 40 nT. *Kamide and Slavin* (1986) and *Zhou and Tsurutani* (1999) showed that preconditioning imposed by IMF $B_z < 0$ afftected the intensity of substorms.

The interaction of IP shocks with the Earth's magnetosphere may also impose threats to human assets on and in the ground. For example, strong IP shocks accompanied with a large increase of the solar wind dynamic pressure compress the whole magnetosphere resulting in more strong magnetic field enhancements on the dayside than on the nightside (*Russell et al.*, 1994a,b). This also intensifies the magnetospheric-ionospheric (MI) currents which produce large magnetic field perturbations on the ground, especially in high-latitude regions, and generate geomagnetically induced currents (GICs) (*Lehtinen and Pirjola*, 1985; *Allen et al.*, 1989; *Molinski*, 2002; *Bolduc*, 2002; *Kappenman*, 2010; *Pirjola*, 2012; *Oliveira and Ngwira*, 2017). Another ionospheric current system greately affected by shock impacts is the equatorial electroject (EEJ) current system, located in well confined low latitude regions (see reviews by *Forbes*, 1981; *Reddy*, 1989, for early references). GICs can also be intensified in low-latitude regions due to enhancements of the EEJ caused by IP shock impacts

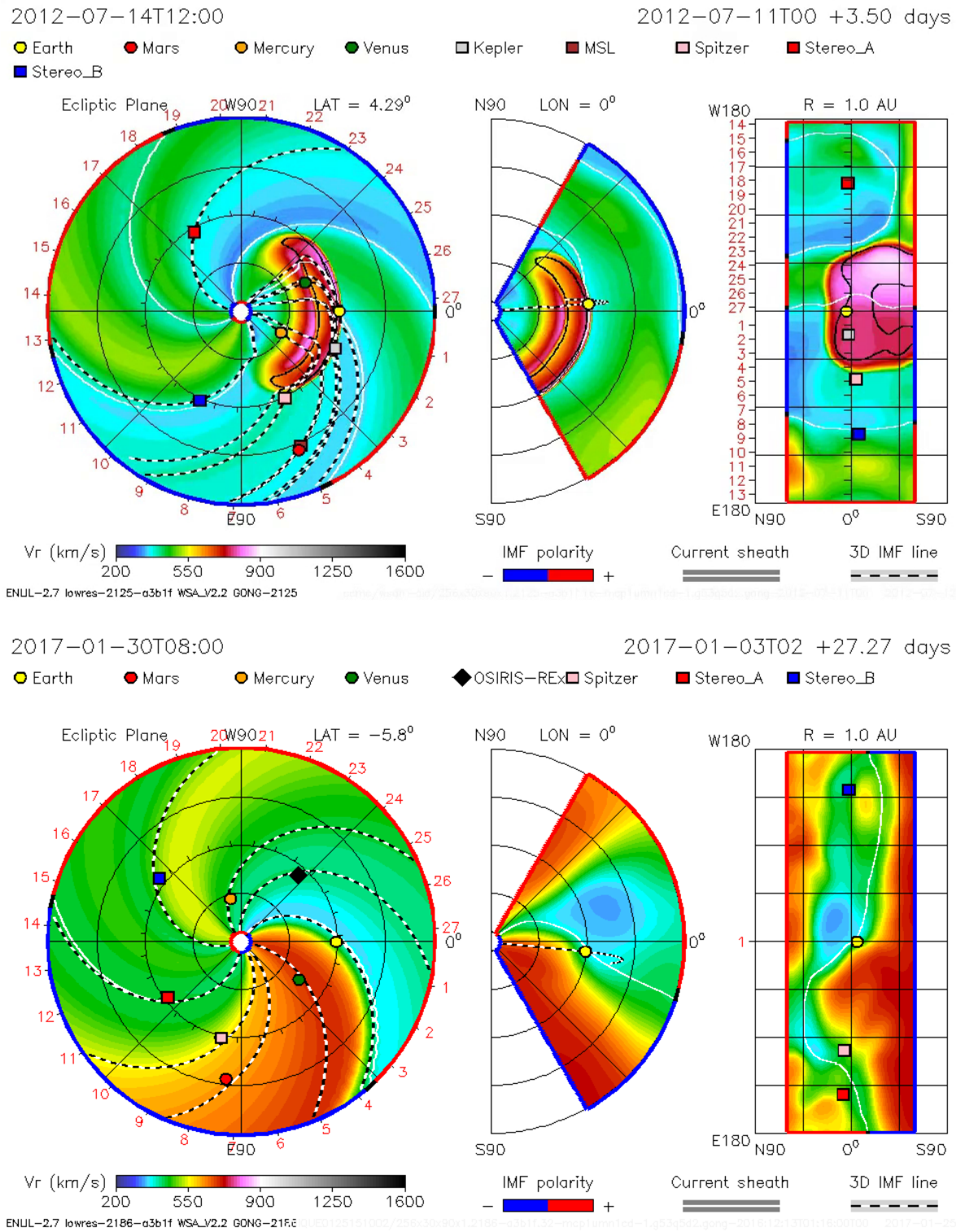

Figure 1: ENLIL simulations of two real events that occurred on 14 July 2012 for a CME (upper panels), and on 30 January 2017 for a CIR (lower panels). All panels show the radial velocity of both solar disturbances. Note that both solar disturbances are represented at moments before they reach the Earth (yellow large dot). The CME-driven shock hits the Earth almost frontally in both equatorial plane (left panel), and meridional plane (middle panel). In contrast, the CIR strikes the magnetosphere with a larger impact angle in both planes. Asymmetric radial velocity is also seen in the east-west/north-south plane cut at 1 AU, as shown in the right column panels. Courtesy of image: Dr. Yihua Zheng and NASA/Goddard CCMC.

(*Anderson et al.*, 2002; *Yizengaw et al.*, 2012; *Carter et al.*, 2015). Pipeline corrosions are frequently asociated with intensifications of GICs (*Gideon et al.*, 1970; *Banach*, 1987; *Martin*, 1993; *Gummow and Eng*, 2002; *Viljanen et al.*, 2006). GICs created by telluric voltages can also be responsible for disruption in power grid equipments caused by extreme heating surpassing all cooling and isolation schemes (*Lanzerotti*, 1979; *Boteler et al.*, 1998; *Bolduc*, 2002; *Kappenman*, 2010; *Oliveira and Ngwira*, 2017), leading to severe economic losses reaching at leat $10 billion (for a modern perspective, see *National Research Council (NRC)*, 2008; *Hapgood and Thomson*, 2010; *Schrijver et al.*, 2014; *Oughton et al.*, 2017).

Although usually IP shocks are assumed to be planar structures traveling in the interplanetary space at near 1 AU (astronomic unit) (*Russell et al.*, 1983a, 2000), nonplanarity conditions have also been observed (*Neugebauer and Giacalone*, 2005). A vector perpendicular to the shock fronts, the shock normal vector, can be computed for all IP shocks if data from at least one spacecraft are available. In general, IP shocks driven by CMEs have their shock normals close to the Sun-Earth line since CMEs tend to travel in the radial direction in the heliosphere (*Klein and Burlaga*, 1982; *Lindsay et al.*, 1994; *Jian et al.*, 2006a). In contrast, shocks driven by CIRs have their shock normals often inclined in relation to the Sun-Earth line (*Jian et al.*, 2006b) since the region of the compression of slow streams by fast streams tend to follow the Parker spiral (*Pizzo*, 1991).

Figure 1 shows examples of shock fronts driven by a CME (14 July 2012, shown in upper row) and a CIR (30 January 2017, shown in lower row). This figure was obtained from ENLIL, a three-dimensional MHD (magnetohydrodynamic) model of the heliosphere available for runs on demand at the NASA Goddard Space Flight Center's Coordinated Community Modeling Center (CCMC) website (`https://ccmc.gsfc.nasa.gov/index.php`). Radial velocity is shown in the first column in the equatorial pane, in the middle column in the meridional plane, and in the right column an east-west/north-south cut at 1 AU. The yellow circles indicate the Earth located at 1 AU (see other planets and spacecraft in their orbits as well). The CME and the CIR are represented in the moment just before striking the Earth. In the case of the CME, it is clear that due to its radial propagation the CME strikes Earth almost head-on in the equatorial plane. However, the CME-shock normal is slightly inclined northward in the meridional plane. In the case of the CIR, the shock inclination is about 30° in relation to the X line in the XY plane. The shock normal also has a large inclination in the XZ plane. In the CME case, radial velocity intensifications seem to be more symmetric in the equatorial plane in comparison to intensifications in the north-south direction, being more intense in the northern hemisphere due to the slight northward CME inclination. In contrast, in the CIR case, as seen in the lower right panel, radial velocity increases in the east heliospheric sector because the CIR shock was highly inclined toward that direction. Radial velocity also increases more in the southern hemisphere due to the southward shock inclination. Therefore, these simulation results show with excellent clarity examples of the general morphology of shocks driven by CMEs or CIRs and the inclination of their shock normal vectors with respect to the equatorial and meridional heliospheric planes.

In addition to other shock parameters, such as shock speed, Mach numbers, and downstream plasma and IMF parameters, the shock normal has been shown to be a geometric parameter that may affect the geomagnetic activity triggered by IP shock impacts on the Earth's magnetosphere. It should be noted the angle the shock normal performs with the Sun-Earth line, the shock impact angle, is different from the angle between the shock normal and the upstream magnetic field vector, the shock angle or simply obliquity. Their individual features will be discussed later in this review. Although many researchers are interested in geomagnetic effects within time intervals corresponding to hours after shock impacts, we focus only on the shock geoeffectiveness close to the shock impact. In general, works in the past 15 years have shown that the more frontal the shock impact, the higher the geomagnetic activity followed by the shock impact. Such results come both from modeling investigations and experimental observations. The ultimate goal of this paper is to review as much accurately as possible all the results obtained on this topic over the last decade and a half. A list of acronyms and abbreviations can be found at the end of the paper.

2. Early prediction and first observations of collisionless shocks in the solar wind

Gold (1955) suggested in a conference held in Cambridge, England, that geomagnetic SI^+ events result from IP shock impacts that generate jumps in the interplanetary gas (plasma) velocity, magnetic field, thermal pressure, and density. Such disturbances are heliospheric structures of large scale. According to *Gold* (1955)'s words,

> I should like to discuss, in connection with the subject of shock waves, some of the magnetic disturbances on the Earth that are caused by solar outbursts. The initial magnetic disturbance at Sudden Commencement of a magnetic storm can be accounted for very roughly by an increase of pressure of the tenuous gas around the Earth. This increase of pressure may perhaps be described as the effect of a wave sent out by the Sun through the tenuous medium between Sun and Earth. In the complete absence of any such medium this description would then correspond to that of a stream of particles, while in the presence of a medium the correct description may lie anywhere between an acoustic wave, a supersonic shock

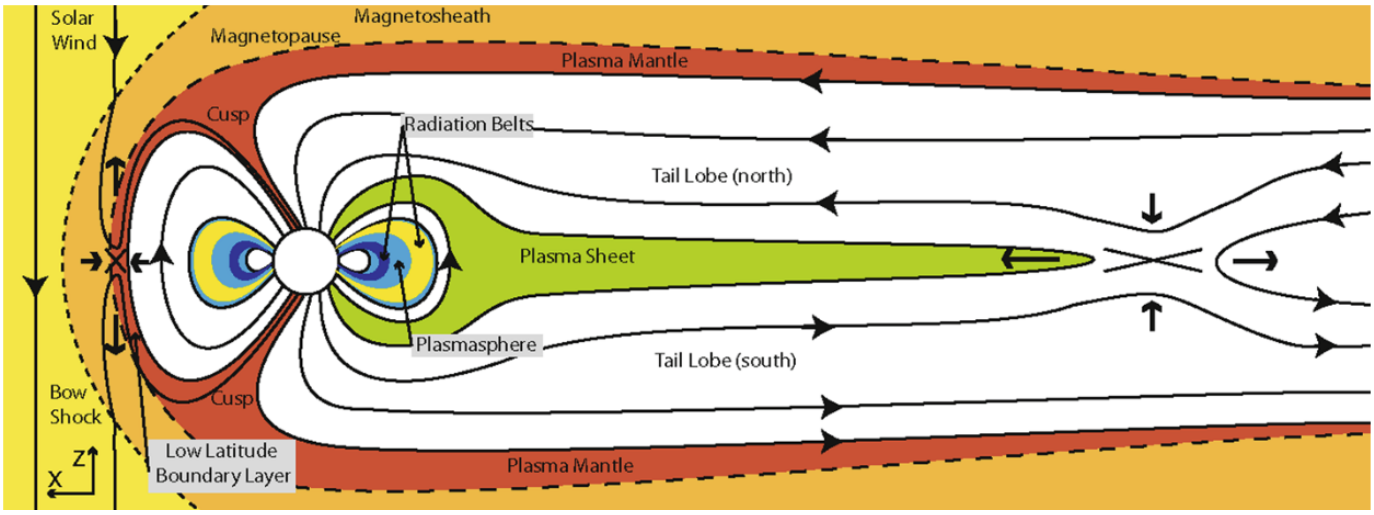

Figure 2: Noon-meridian cut representation of the Earth's magnetosphere, with some of its main regions. Figure extracted from *Eastwood et al.* (2014).

> wave or an unimpeded corpuscular stream. The observations of magnetic storms may hence give us a fairly direct proof of the existence of shock waves in the interplanetary medium.

The possibility of the existence of shocks in the interplanetary space was then accepted. *Parker* (1961) suggested a model for shock propagation in the interplanetary space. His idea was further extended by *Hundhausen and Gentry* (1969). However, the first evidences of collisionless shocks in nature were observed in the interplanetary space. As seen above, the existence of the magnetosphere suggested the formation of a stationary collisionless shock at the front of the magnetosphere. Curiously, the existence of a stationary shock, i.e., a shock at rest in the Earth's reference frame, was suggested in the same edition of the *Journal of Geophysical Research* by *Axford* (1962) and *Kellogg* (1962). The bow shock was first observed by the Mariner 2 spacecraft as irreversible changes in the solar wind and IMF which were interpreted as hydromagnetic shocks (*Ness et al.*, 1964; *Sonett et al.*, 1964). The bow shock is formed if a supersonic flow interacts with an obstacle, and it separates the pristine solar wind from the subsonic plasma flow in the magnetosheath. Another magnetospheric boundary is the magnetopause, a current layer whose position is determined by the pressure balance condition between the solar wind dynamic pressure and the magnetospheric magnetic pressure, first observed by *Heppner et al.* (1963) and *Cahill and Amazeen* (1963). The region between the bow shock and the magnetopause is called the magnetosheath. The magnetosheath in the subsolar region for typical solar wind conditions is located approximately at a distance between $10R_E$ and $13R_E$ (Earth radius of ∼6400 km) from the Earth (*Cahill and Amazeen*, 1963; *Heppner et al.*, 1963; *Russell*, 1984). This region is highly turbulent because it is formed by the shocked solar wind (*Russell*, 1984; *Paschmann et al.*, 2005). The bow shock, magnetopause, and magnetosheath are shown in Figure 2, as seen in *Eastwood et al.* (2014). The numerical gas dynamic model of *Spreiter et al.* (1966) reasonably well predicted the bow shock formation and magnetosheath flow between the bow shock and magnetopause obstacle. For a broader perspective on the discovery of the magnetosphere, see, e.g., *Russell* (1984) and *Gillmor and Spreiter* (1997).

3. Brief description of theoretical background

3.1. Classification of shocks

In a magnetized plasma, three propagating MHD wave modes are fast, Alfvén, and slow, while entropy waves move with the same speed as a local medium. Correspondingly, there are three charactestic velocities in the plasma, fast (V_f), Alfvén (V_f), and slow (V_s) speeds. MHD waves under certain conditions evolve to shocks, and these shocks are classified as fast, intermediate, and slow shocks according to their upstream and downstream speeds. If plasma flow is superfast (i.e. the flow velocity V is larger than V_f) upstream of a shock, but subfast and superalfvenic (i.e., $V_A < V < V_f$) downstream of a shock in the shock reference frame, this is a fast shock (*Landau and Lifshitz*, 1960). Slow shocks are characterized by a superslow and subalfvenic upstream speed ($V_s < V < V_A$), and a subslow downstream speed ($V < V_s$). There are four other shock types characterized by certain combinations of upstream and downstream speeds and an entropy increase through the shock, e.g., a type with subfast and superalfvenic speed upstream and subalfvenic and superslow speed downstream. All these shocks are called intermediate; they do not satisfy the evolutionary condition in the ideal MHD theory, therefore it was suggested that they immediately evolve into other stable MHD discontinuities (*Akhiezer et al.*, 1959; *Jeffrey and Taniuti*, 1964;

Kantrowitz and Petschek, 1966). However subsequent analytical (*Kennel et al.*, 1989; *Hada*, 1994) and numerical (*Wu*, 1988, 1990; *De Sterck and Poedts*, 2000) studies showed that intermediate shocks are evolutionary in dissipative MHD, but may be still non stationary in hybrid simulations (*Lee et al.*, 1989). Some observations in the solar wind also confirmed the existence of intermediate shocks (*Chao et al.*, 1993; *Feng and Wang*, 2008; *Feng et al.*, 2016). *Tsurutani et al.* (2005) suggested that investigations of Alfvén waves may be an excellent pathway to identify the plasma properties of eventual intermediate shocks. However, both intermediate and slow shocks have been rarely observed in the solar wind. Moreover, only much stronger fast IP shocks result in significant magnetospheric response, therefore our review is mainly limited to fast shocks. For more details on intermediate shocks, see review by *Tsurutani et al.* (2011).

Shocks are classified in terms of their direction of propagation with respect to the Sunas well. If, in the shock frame of reference, shocks propagate antisunwards/sunwards, they are classified as forward/reverse shocks (*Burlaga*, 1971; *Kennel et al.*, 1985; *Tsurutani et al.*, 2011; *Oliveira*, 2017). CME-driven shocks are usually fast and forward shocks (*Klein and Burlaga*, 1982; *Lindsay et al.*, 1994; *Berdichevsky et al.*, 2000; *Oh et al.*, 2007; *Kilpua et al.*, 2015), while fast and reverse shocks are driven, for example, by overexpanding CMEs (*Gosling et al.*, 1994) and CIRs near Earth's orbit (*Jian et al.*, 2006b; *Kilpua et al.*, 2015), which makes them very rare to be observed (see, e.g. *Chao and Olbert*, 1970; *Burlaga and Chao*, 1971; *Whang*, 1982; *Smith et al.*, 1984; *Whang et al.*, 1996; *Lin et al.*, 2009). At 1 AU, most IP shocks are fast and forward shocks (*Richter et al.*, 1985). However, a few slow shocks can be observed beyond 1 AU since in most cases they are completely driven there (*Richter et al.*, 1985). Since this paper focuses on fast forward shocks, we refer *Stone and Tsurutani* (1985) and references there for discussions on slow mode shocks. At the Earth's orbit, most IP shocks are CME-driven shocks, and only a few shocks are CIR-driven, because CIR-driven shocks are usually completely developed beyond 1 AU (*Smith and Wolfe*, 1976; *Richter et al.*, 1985; *Smith*, 1985).

Theoretical aspects of MHD shocks were reviewed in many publications (see, e.g. *Landau and Lifshitz*, 1960; *Kantrowitz and Petschek*, 1966; *Kennel et al.*, 1985; *Oliveira*, 2017). In particular, all plasma parameters, speed (V), proton density (N), thermal pressure (P) and total magnetic field (B) increase for a fast forward shock (FFS). For a fast reverse shock (FRS), all parameters decrease, except V because all shocks are dragged away by the solar wind. In the case of slow forward shocks (SFSs), N, P and V increase, while B decreases. Finally, N and P decrease and B and V increase for slow reverse shocks (SRSs). The summary of these shock properties are plotted in Figure 3 from *Oliveira* (2017).

The shock speed may also be related to the strength of IP shocks, since IP shocks with high Mach numbers drive

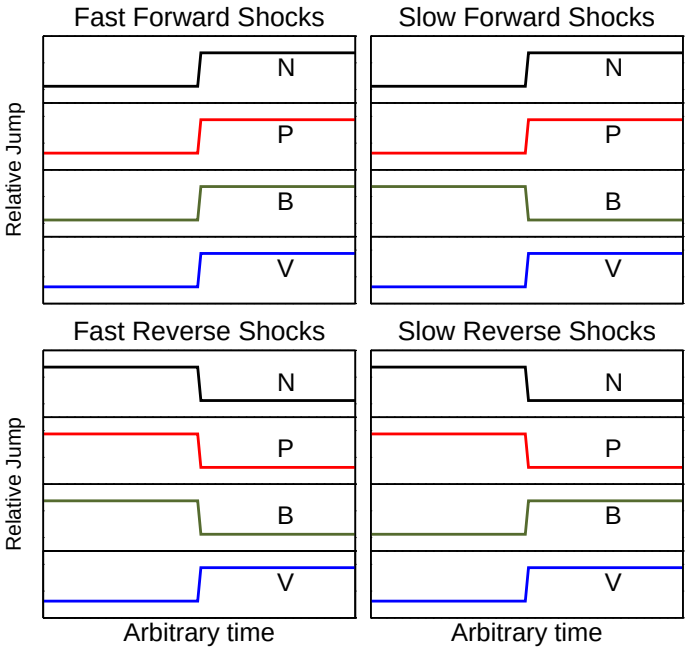

Figure 3: Theoretical jump conditions of proton density (N), thermal plasma pressure (P), total magnetic field (B), and total plasma velocity (V) for all types of IP shocks deduced from MHD shock theory. After *Oliveira* (2017).

large increases of entropy and dynamic pressure anhead of them. Another way to measure IP shock strength is the compression ratio X, the ratio of downstream to upstream plasma density which can theoretically reach the maximum value of 4 (*Kennel et al.*, 1985; *Tsurutani and Stone*, 1985). However, most IP shocks at 1 AU have X no larger than 1.5 (*Tsurutani and Stone*, 1985; *Echer et al.*, 2003; *Kilpua et al.*, 2015; *Oliveira and Raeder*, 2015). As will be discussed later, FFSs are not only more abundant, but also trigger more intense geomagnetic activity, e.g. intensifications in field aligned currents, cross polar cap potential, and auroral precipitation, when they impact the Earth's magnetosphere (*Zhou and Tsurutani*, 2001; *Echer et al.*, 2004, 2011; *Oliveira and Raeder*, 2014, 2015; *Oliveira et al.*, 2016).

Since the space plasma moves away from the Sun with a frozen-in solar magnetic field, or the IMF, a geometric factor is crucial for determining downstream (shocked region) plasma parameters as functions of the upstream (non-shocked) plasma parameters. This factor is the shock normal which is perpendicular to the shock front. Thus, IP shocks can be classified in terms of the angle θ_{B_n} between the shock normal and the upstream magnetic field vector. In the shock frame of reference, in general, the IP shocks with θ_{B_n} close to 90° are classified as perpendicular shocks, whereas shocks are classified as parallel if this angle is almost null. In this case, heating of plasma in the direction parallel to magnetic field and magnetic fluctuations of large amplitude will occur (*Tsurutani and Rodriguez*, 1981; *Tsurutani et al.*, 1983; *Kennel et al.*, 1984a,b). If this angle is arbitrarily in between, the shock is said to

be an oblique shock. Modeling and experimental results have shown that perpendicular shocks are generally more geoeffective than parallel or oblique shocks since they tend to compress the downstream plasma more effectively (*Jurac et al.*, 2002; *Oliveira and Raeder*, 2014; *Oliveira*, 2015, 2017).

Transient IP shocks can accelerate charged particles to energies of scales of tens of MeV. Such accelerated particles are usually associated with solar energetic particle events and depend upon the θ_{B_n} angle (*Tylka and Lee*, 2006; *Richardson and Cane*, 2010). At quasi-parallel shocks, particles are scattered and accelerated by diffusion processes related to first-order Fermi processes as first suggested by *Fermi* (1949) (see also *Toptyghin*, 1980; *Lee*, 1983). In the case of quasi-perpendicular shocks, particles accelerate along the shock front in the direction of the electric field given by $-\mathbf{v}\times\mathbf{B}$ (*Pesses et al.*, 1979). Parallel and perpendicular shocks enhance turbulence energies in the solar wind across the shock as well (*Tsurutani et al.*, 1983; *Adhikari et al.*, 2016). However, plasma waves had been detected before at the bow shock in both upstream and downstream regions (see references in *Tsurutani and Rodriguez*, 1981). These high energetic particles play an important role in space weather investigations since they pose serious threats to human assets in space, such as satellites, and human activities in space as well (*Reames*, 1999; *Manchester IV et al.*, 2005). Particles that are gradually accelerated during shock propagation from the Sun to the Earth are very important for space weather purposes (*Reames*, 1999). Quasi-parallel shocks are generally weaker than quasi-perpendicular shocks since the magnetic field vector hardly changes across the shock surface (*Burgess et al.*, 2005). Moreover, quasi-parallel shocks are rarely observed in the solar wind at the Earth's orbit, and perhaps their lackness there is complemented by the difficulty in determining their properties (*Kruparova et al.*, 2013; *Kilpua et al.*, 2015; *Oliveira and Raeder*, 2015).

Planar magnetic structures (PMSs) are found in the intermediate downstream regions of quasi-perpendicular shocks with high upstream plasma beta (*Kataoka et al.*, 2005; *Palmerio et al.*, 2016). The planar part of the sheaths associated with these shocks are expected to be more geoeffective since they have large magnetic fields out of the ecliptic plane (*Palmerio et al.*, 2016). In addition, *Kilpua et al.* (2013) showed that the solar wind/MI coupling is amplified by these sheaths, which in turn produces the largest power in ULF range magnetic fluctuation within the sheaths of strong CMEs.

MHD shocks correspond to a particular type of MHD discontinuities where all plasma parameters and magnetic field undergo increases across the discontinuity surface. However, there are other discontonuities that are not shocks, i.e., not all IMF and plasma parameters vary across the discontinuity. Such discontinuities discussed, e.g., by *Landau and Lifshitz* (1960) correspond to contact, rotational and tangential discontinuities. While FFSs are detected at a rate of 50 per year during solar maximum and 7.5 per year during solar minimum (*Echer et al.*, 2003; *Kilpua et al.*, 2015; *Oliveira and Raeder*, 2015), rotational and contact discontinuities are observed at a rate of 1-2 per hour (*Tsurutani and Smith*, 1979; *Lepping and Behannon*, 1986; *Tsurutani et al.*, 2011). However, the observations of contact discontinuities near Earth's orbit are very rare (*Colburn and Sonett*, 1966; *Hudson*, 1970; *Smith*, 1973; *Hsieh et al.*, 2014) because the plasma along their surfaces diffuse very fast. That is why studies of contact discontinuities are subject of modeling investigations (*Tsai et al.*, 2009). Since MHD discontinuities other than FFSs are outside the scope of this review paper, we refer the reader to many reviews of their properties in the literature (see, e.g. *Landau and Lifshitz*, 1960; *Kennel et al.*, 1985; *Tsurutani and Stone*, 1985; *Tsurutani et al.*, 2011; *Oliveira*, 2017).

3.2. Computation of shock normals and speeds

IP shock normals are often calculated by solving the Rankine-Hugoniot (RH) equations which are deduced from a straightforward assumption of planar discontinuities and the conservations of mass, momentum and energy through the discontinuity surface, in addition to the continuity of normal magnetic field and tangential electric field. The variables involved in those calculations are the upstream and downstream IMFs, plasma parameters and shock velocity. Since there have been many textbooks and reviews on the subject, we will only summarize important expressions used in this review (see, e.g. *Petschek*, 1958; *Landau and Lifshitz*, 1960; *Jeffrey and Taniuti*, 1964; *Kantrowitz and Petschek*, 1966; *Burlaga*, 1971; *Priest*, 1981; *Kennel et al.*, 1985; *Schwartz*, 1998; *Gurnett and Bhattacharjee*, 2005; *Tsurutani et al.*, 2011; *Oliveira*, 2017, and references therein).

The most common normal determination methods obtained from single spacecraft data are classified as follows. If a shock is almost parallel, the magnetic coplanarity (MC) method, which uses only IMF data, as described by *Colburn and Sonett* (1966) and *Lepping and Argentiero* (1971), produces more reliable results. For almost perpendicular shocks, the velocity coplanarity (VC) method yields more adequate results (*Abraham-Shrauner and Yun*, 1976). In the case of oblique shocks, the use of a set of three equations that mix solar wind and IMF data (MD1,MD2,MD3) gives more adequate results (*Abraham-Shrauner*, 1972; *Abraham-Shrauner and Yun*, 1976). *Viñas and Scudder* (1986) increased the accuracy of shock normal determination using the least squares technique for a reduced set of RH conservation laws, and later *Szabo* (1994) and *Koval and Szabo* (2008) extended this technique to the whole set of RH equations. However, it is important to emphasize that the determination of shock normals is subject to large uncertanties despite the method used. See, e.g., *Schwartz* (1998) for discussions on this subject.

In summary, IP shock normals are computed by the following equations (the 1 and 2 indices correspond to IMF

Earth's reference frame[a]: $\theta_{x_n} \rightarrow 180^\circ - \theta_{x_n}$		
impact	frontal	$< 45^\circ$ or $> 135^\circ$
angle	inclined	$\geq 45^\circ$ or $\leq 135^\circ$
Shock reference frame[b]: θ_{B_n}		
magnetic	parallel	close to 0°
obliquity	oblique	around 45°
angle	perpendicular	close to 90°

[a] Generally fixed. It can be Earth or a spacecraft.
[b] Moves with the shock.

Table 1: Summary of the geometric properties of IP shocks reviewed in this paper in terms of the angle θ_{x_n}, in the Earth's or spacecraft's reference frame, and θ_{B_n}, in the shock's reference frame.

and plasma parameters in the upstream and downstream regions, respectively):

$$\mathbf{n}_{\rm MC} = \frac{\mathbf{B}_2 \times \mathbf{B}_1 \times (\Delta\mathbf{B}_{21})}{|\mathbf{B}_2 \times \mathbf{B}_1 \times (\Delta\mathbf{B}_{21})|} \quad (1)$$

$$\mathbf{n}_{\rm MD1} = \frac{(\mathbf{B}_1 \times \Delta\mathbf{v}_{21}) \times \Delta\mathbf{B}_{21}}{|[\mathbf{B}_1 \times \Delta\mathbf{v}_{21}] \times \Delta\mathbf{B}_{21}|} \quad (2)$$

$$\mathbf{n}_{\rm MD2} = \frac{[\mathbf{B}_2 \times \Delta\mathbf{v}_{21}] \times \Delta\mathbf{B}_{21}}{|[\mathbf{B}_2 \times \Delta\mathbf{v}_{21}] \times \Delta\mathbf{B}_{21}|} \quad (3)$$

$$\mathbf{n}_{\rm MD3} = \frac{[\Delta\mathbf{B}_{21} \times \Delta\mathbf{v}_{21}] \times \Delta\mathbf{B}_{21}}{|[\Delta\mathbf{B}_{21} \times \Delta\mathbf{v}_{21}] \times \Delta\mathbf{B}_{21}|} \quad (4)$$

$$\mathbf{n}_{\rm VC} = \frac{\Delta\mathbf{v}_{21}}{|\Delta\mathbf{v}_{21}|} \quad (5)$$

where $\Delta\mathbf{B}_{21} = \mathbf{B}_2 - \mathbf{B}_1$ and $\Delta\mathbf{v}_{21} = \mathbf{v}_2 - \mathbf{v}_1$.

Usually, shock normals are calculated with data obtained from a single spacecraft. However, shock normals calculated with data from several spacecraft correspond to more reliable results (see, e.g., *Burlaga et al.*, 1980; *Russell et al.*, 1983a,b; *Russell and Alexander*, 1984; *Thomsen*, 1988; *Russell et al.*, 2000; *Szabo*, 2005; *Koval and Szabo*, 2010; *Grygorov et al.*, 2014). However, multiple spacecraft data are relatively rare and their use in a large statistical study would be inconsistent. Their use ought to be desirable only in isolated events, if data allow.

In GSE (Geocentric Solar Ecliptic) coordinates, the X axis points radially from the Earth to the Sun. From equations (1-4) above, θ_{x_n}, the angle between the shock normal and the X line, is calculated by the expression:

$$\theta_{x_n} = \arccos(n_x)\,. \quad (6)$$

Once the shock normal vector has been calculated, the obliquity θ_{B_n}, the angle between the upstream magnetic field vector and the shock normal vector is given by

$$\theta_{B_n} = \frac{\mathbf{n}\cdot\mathbf{B}}{|\mathbf{B}|} \quad (7)$$

The shock speed is calculated from the upstream (1) and downstream (2) plasma parameters according to the RH jump conditions:

$$v_s = \frac{(\rho_2\mathbf{v}_2 - \rho_1\mathbf{v}_1)\cdot\mathbf{n}}{\rho_2 - \rho_1} \quad (8)$$

Finally, the shock strength is usually determined by Mach numbers given by

$$M_i = \frac{v_r}{v_i}\,, \quad (9)$$

where v_r is the relative velocity between the shock and the solar wind, and M_i and v_i are the Mach numbers and speeds for sound, Alfvénic and fast magnetosonic waves (as denoted by subscript i). In fact, the main frame of reference for physical purposes is the one moving with the plasma. However, the use of the Earth or a spacecraft as a frame of reference is only applied for practical applications.

3.3. A note on terminologies

The geometry of IP shocks is often discussed in the literature from a point of view of two different frame of references, namely the shock itself and the Earth or a satellite. Then, to avoid confusion, we will use terminologies connected to these two frames. The terminologies *parallel*, *oblique* and *perpendicular* refer to the angle between the upstream magnetic field and the shock normal, namely θ_{B_n}, *in a frame of reference moving with the shock*. On the other hand, the terminologies *inclined* and *frontal* are associated with the angle between the shock normal and the GSE Sun-Earth line, θ_{x_n}, as *measured by an observer at Earth or a spacecraft*. Nevertheless, it should be noted that other authors may use these terminologies interchangeably.

The shock normal vector is usually defined pointing either in the sunward or anti-sunward directions. In the former case, a frontal shock has $\theta_{x_n} = 180^\circ$, and in the latter case, $\theta_{x_n} = 0^\circ$. In this paper, inclinations of shocks where $\theta_{x_n} \rightarrow 180^\circ - \theta_{x_n}$ are assumed to be the same. Table 1 summarizes the shock angle nomenclature used in this review paper.

4. Data and models

4.1. Plasma and IMF data

In this section we briefly describe the solar wind plasma and IMF measurements that have primarily been used in the studies that are discussed in this review. The solar wind data at the L1 Lagrangian point upstream of the Earth were often obtained from two spacecraft, Wind and ACE (Advanced Composition Explorer). The Wind plasma data, with time resolution of 3 seconds, were obtained from the Solar Wind Experiment (SWE) instrument, described by *Ogilvie et al.* (1995), while the IMF data were recorded by the Magnetic Fields Investigation Instrument (MFI) (*Lepping et al.*, 1995). The ACE 64-second time resolution data were obtained from the Solar Wind Electron, Proton and Alpha Monitor (SWEPAM), described by *McComas et al.* (1998) and *Smith et al.* (1998). The ACE magnetometer instrument (MAG) provides 16-second time resolution data as explained by *Smith et al.* (1998). The Wind and ACE data can be downloaded from

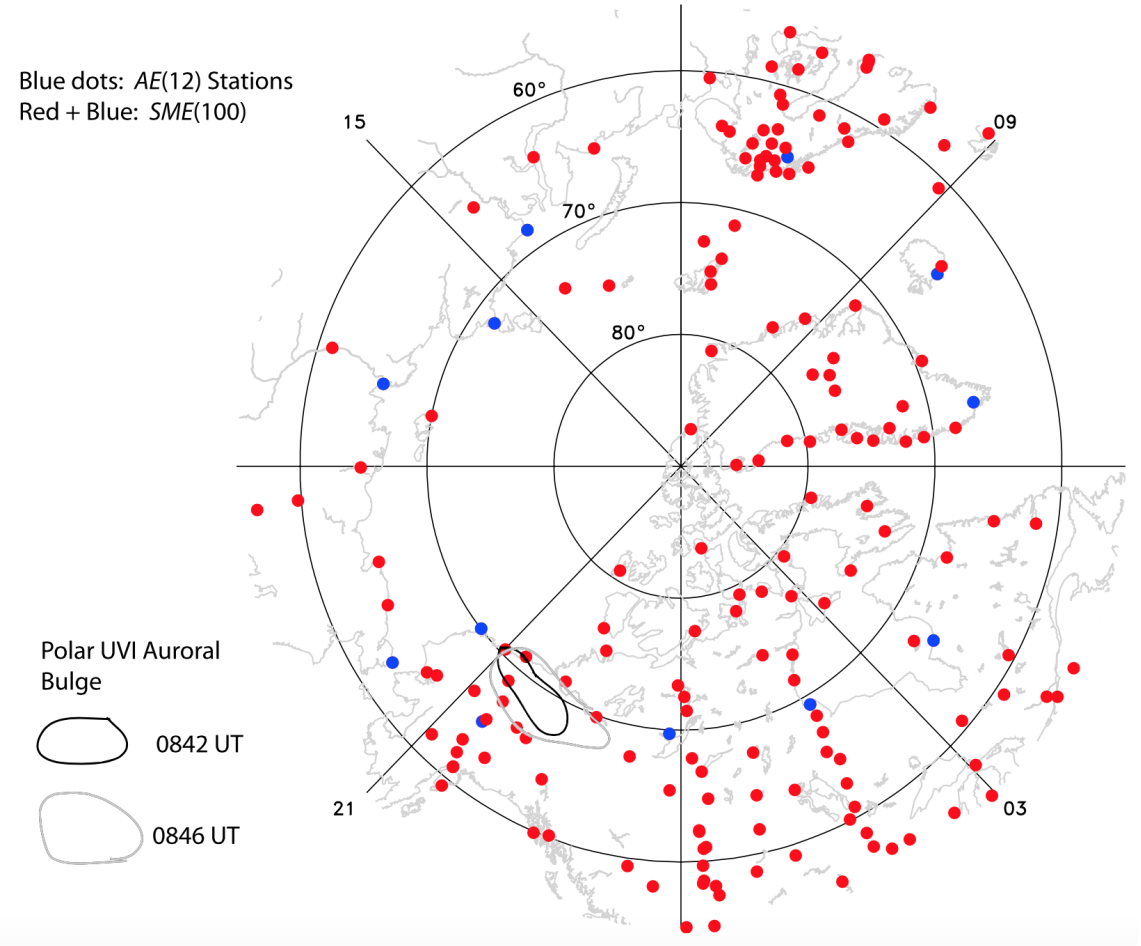

Figure 4: IAGA (blue dots) and SuperMAG (red dots) station distribution in the northern hemisphere. As discussed by *Newell and Gjerloev* (2011a), a sharp increase in the SML index was measured by the SuoerMAG index stations, but AL enhancements were not detected by the IAGA stations. There were no IAGA stations under the auroral bulge for that event. This figure was taken from *Newell and Gjerloev* (2011a).

the CDAWeb (Coordinated Data Analysis Web) interface website (`http://cdaweb.gsfc.nasa.gov`).

Data from STEREO (Solar Terrestrial Relations Observatory), a constellation of two identical satellites, STEREO-A and STEREO-B, were also used in the calculation of shock properties, but in a smaller scale. STEREO obtains magnetic field measurements by the magnetometer IMPACT (In-situ Measurements of Particles and CME Transients), with time resolution of 0.125 second, plasma measurements by the PLASTIC (Plasma and Suprathermal Ion Composition), with time resolution of 60 seconds. Technical aspects and functionalities of IMPACT and PLASTIC were detailed by *Acuña et al.* (2008) and *Galvin et al.* (2008), respectively. STEREO-A orbits the Sun at approximately 0.96 AU.

4.2. Geomagnetic index data

The understanding of determined geomagnetic activity depends on the choice of the most convenient geomagnetic index (*Rostoker*, 1972; *Huttunen et al.*, 2002). For example, the logarithmic index Kp introduced by *Bartels* (1949) (and its linear counterpart Ap) is a good indicator of geomagnetic activity in regions of middle geomagnetic latitudes whose contributions come from the auroral electrojets and the ring current. If one is interested in measuring disturbances in the ring current, the Dst (disturbance storm time) index, introduced by *Sugiura* (1964), is a good choice. The Dst index was accepted after the International Geophysical Year (IGY) in 1964. The time resolution of the Dst data is 1 hour. However, for events with a time range smaller than a day, the 1-minute time resolution symmetric ring current index, SYM-H, first suggested by *Iyemori* (1990), is preferred over the Dst index. Both Dst and SYM-H index data are avaiblable for downloading from the website of the World Data Center (WDC) located in Kyoto, Japan (`http://wdc.kugi.kyoto-u.ac.jp`).

Auroral zone disturbances have been measured throughout the decades by geomagnetic indices first introduced by *Davis and Sugiura* (1966). The initial number of geomagnetic stations was 7, and in the following years this number was increased to 12, and sometimes there were many more stations used (see, e.g., *Rostoker*, 1972, for more details).

The current 12 ground stations record geomagnetic perturbations in different locations around the globe and the results are superposed. The resulting upper and lower envelopes of this superposition give rise to two indices, the amplitude upper (AU, always positive) index, and the amplitude lower (AL, always negative) index. Usually, the AL index is associated with substorm activity, whereas the AE (auroral electroject) index is associated with nightside auroral activity. The AE index is defined as AE = AU − AL. These indices are recognized by the International Association of Geomagnetism and Aeronomy (IAGA) as official geomagnetic indices, and have been heavily used by the space science community. The IAGA indices, with time cadence of 1 minute, are readily available for downloading from the WDC website (`http://wdc.kugi.kyoto-u.ac.jp`). Years later, *Kamide et al.* (1982) used 70 magnetometer stations to derive the AE index. However, they did not report quantitative results of their analyses. More surprisingly, *Kamide* (2005) even suggested the community to stop deriving and using the AE index because of its non-sense physical meaning for auroral electroject descriptions.

Sometimes the IAGA indices fail to produce a realistic measurement of strong substorm activity due to the limited number of ground magnetometers used for their computation. In order to overcome this deficiency, amongst others, a large worldwide collaboration named SuperMAG, with over 300 ground magnetometers came about to compute enhanced AU, AL, and AE indices (*Gjerloev*, 2009). The SuperMAG enhanced AU, AL and AE indices, or SMU, SML and SME indices, are essentially the same as the IAGA indices, but they consist in an enhanced index version since they are calculated from data from over 300 ground magnetometers. The 1-minute time resolution SuperMAG indices were used to investigate substorm and nightside auroral activities triggered by IP shocks with different impact angles and are reviewed in this paper. The SuperMAG data are readily available for download from the very convenient SuperMAG website `http://supermag.jhuapl.edu/info/?page=acknowledgement`. A summary of all SuperMAG collaborators found at the SuperMAG website is represented by Table 2. Several useful plotting tools are available there as well.

An example of an auroral substorm event observed by different numbers of IAGA and SuperMAG stations is represented by Figure 4 extracted from *Newell and Gjerloev* (2011a). In that figure, blue dots represent IAGA stations, whereas red dots represent SuperMAG stations. In their event, *Newell and Gjerloev* (2011a) show with Polar UVI imagery that the expansion of the auroral bulge traveled over no AE ground stations, but instead passed over almost ten of the SME ground stations. This auroral substorm was underestimated by the AE stations, as shown by Figure 5 from *Newell and Gjerloev* (2011a). Polar UVI images identified an auroral onset on 30 January 1997 at 0841 UT. The AL stations did not detect this substorm event; however, the SML stations recorded a substorm onset 37

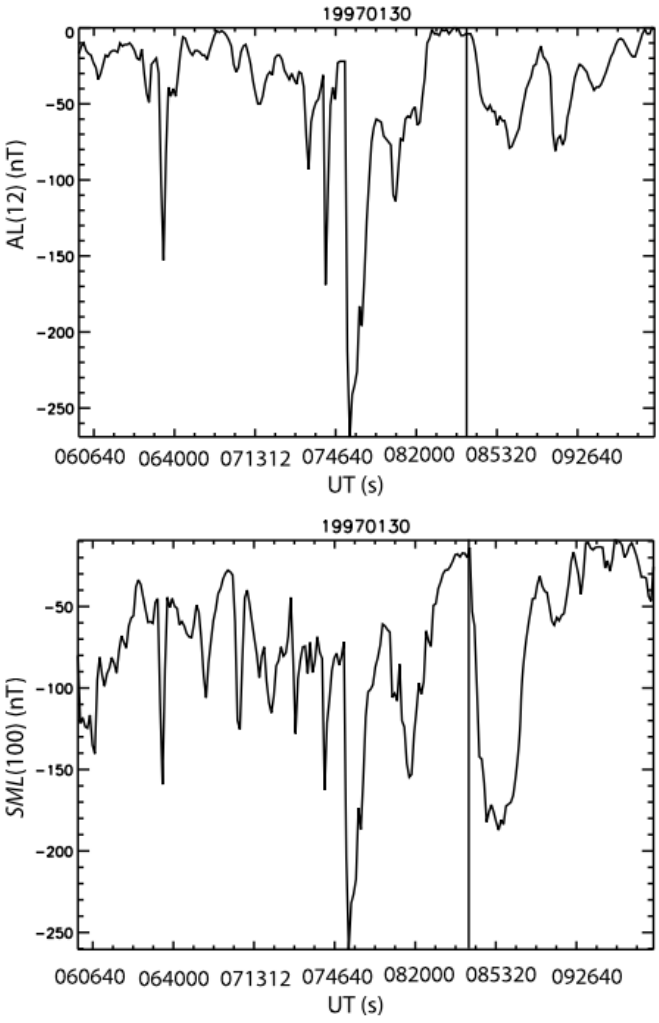

Figure 5: Auroral substorm event observed by IAGA and SuperMAG stations on 30 January 1997. Polar UVI images identified an auroral substorm onset at 0841 UT. AL did not detect this onset, but SML did 37 seconds after the onset determined by Polar UVI images. Figure from *Newell and Gjerloev* (2011a).

seconds after the onset registered by Polar UVI observations. Therefore it is important to mention that AE and SME, besides the other SuperMAG indices, are primarily of the same nature, but with the SuperMAG indices being enhanced by the higher number of ground based stations used to build the SuperMAG indices. More details about the SuperMAG initiative can be found in *Gjerloev* (2009); *Newell and Gjerloev* (2011a,b), and an explanation about data techniques and assimilation is reported by *Gjerloev* (2012).

A statistical study of IP shock geoeffectiveness with different shock impact angles involving over 450 FFSs was conducted by *Oliveira and Raeder* (2015) and *Oliveira et al.* (2016). These authors carefully analyzed enhancements of SuperMAG indices followed by shock impact events in a time interval of January 1995 to December 2013. The review of the results found by these studies is in the scope of this paper.

Table 2: The SuperMAG project collaborators as seen at the SuperMAG website http://supermag.jhuapl.edu.

Magnetometer chain	PI/SuperMAG collaborator[a]
Intermagnet	USGS, Jeffrey J. Love
CARISMA	Ian Mann
CANMOS	D. Boteler
The S-RAMP Database	K. Yumoto and Dr. K. Shiokawa
The SPIDR database	NOAA/NGDC
AARI	Oleg Troshichev
The MACCS program	M. Engebretson, GUGSC[b]
GIMA MEASURE	UCLA IGPP and Florida Institute of Technology
SAMBA	Eftyhia Zesta
210 Chain	K. Yumoto
SAMNET	Farideh Honary
IMAGE magnetometer array maintenance	Eija Tanskanen
PENGUIN/AUTUMN	Martin Conners
DTU Space	Dr. Jürgen Matzka
South Pole and McMurdo Magnetometer	L. J. Lanzarotti and A. T. Weatherwax
ICESTAR/RAPIDMAG/PENGUIn	British Artarctic Survey
McMac	Dr. Peter Chi
BGS	Dr. Susan Macmillan
IZMIRAN/GFZ	Dr. Jürgen Matzka
MFGI	B. Heilig
IGFPAS	J. Reda
University of L'Áquila	M. Vellante
SuperMAG	Jesper W. Gjerloev

[a] This list of collaborators may change as new magnetometer chains join the SuperMAG team.
[b] Geomagnetism Unit of the Geological Survey of Canada.

4.3. Numerical MHD models

In space physics, local satellite observations are almost always not enough to draw general and global conclusions of plasma effects. In order to alleviate this deficiency, a powerful tool corresponding to numerical global MHD models has been extensively used in space plasma physics investigations. In this section some of the most popular models used by the space physics community will be briefly reviewed.

The PPMLR-MHD (Piecewise Parabolic Method with a Lagrangian Remap) is a Lagrangian version of the PPM (Piecewise Parabolic Method) that was developed by the University of Science and Technology of China (USTC) and the Center for Space Science and Applied Research (CSSAR), Chinese Academy of Sciences (see, e.g. *Hu et al.*, 2005; *Guo and Hu*, 2007, and references therein). This code uses a numerical scheme with second order accuracy in time and third order accuracy in space to solve a set of conservative ideal MHD equations (*Wang et al.*, 2013). The ionospheric part of the code is assumed to be a sphere of radius approximately $1R_E$ and is connected to the magnetosphere through field-aligned currents (*Guo and Hu*, 2007).

The BATS-R-US (Block Adaptive-Tree Solar wind Roe-type Upwind Scheme) MHD code (*Powell et al.*, 1999) was developed by the Computational Magnetohydrodynamics Group at the University of Michigan, now Center for Space Environment Modeling (CSEM). BATS-R-US solves the three-dimensional MHD equations by using a numerical method described by *Powell et al.* (1999). The MHD part of the code is connected by field-aligned currents to the ionospheric part of the code which calculates the distribution of electric potential in the northern and southern hemispheres, as described by *Ridley et al.* (2004). Later, BATS-R-US was coupled into the Space Weather Modeling Framework (SWMF) (*Tóth et al.*, 2005). The SWMF is a model that self-consistently couples different regions from the solar corona to the Earth's upper atmosphere. For instance, the SWMF is capable of calculating magnetic perturbations measured by artificial magnetometer stations located in any point of the Earth's surface. The SWMF scheme is outlined by *Tóth et al.* (2007).

The OpenGGCM (Open Geospace General Circulation Model) is a global coupled model of Earth's magnetosphere and ionosphere. The first versions of the OpenGGCM code came about back in the 1990's at the University of California in Los Angeles (UCLA). The OpenGGCM is currently located at the University of New Hampshire (UNH). The model solves the resistive MHD equations in the magnetospheric part of the code and couples the magnetospheric and ionospheric parts through field-aligned currents as well (*Raeder*, 2003). The OpenGGCM uses an MI coupling

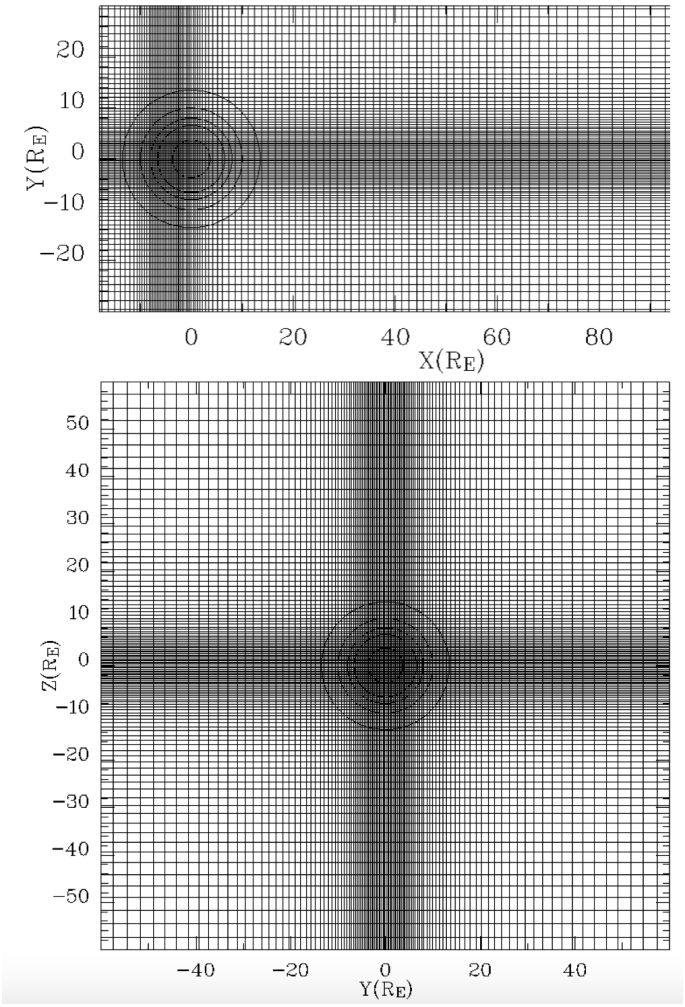

Figure 6: Typical streched cartesian grids used by OpenGGCM simulations. Upper panel: XY plane; lower panel: YZ plane. The simulation runs conducted by *Oliveira and Raeder* (2014) were 20 times as larger as those seen in this figure (see section 8.3).

module that can map field aligned currents from the ionospheric boundary back to the magnetosphere. In addition, this model can compute electron precipitations using the Hall and Pedersen conductances obtained from empirical relations. The ionosphere-thermosphere system is modeled using the NOAA (National Oceanic and Atmospheric Administration) CTIM (Coupled Thermosphere Ionosphere Model (*Fuller-Rowell et al.*, 1996; *Raeder et al.*, 2001a)). OpenGGCM can be run at the CCMC website as a community model for model runs on demand as well (*Rastätter et al.*, 2013; *Pulkkinen et al.*, 2011, 2013).

The OpenGGCM code uses a modified version of the cartesian GSE coordinate system. In this coordinate system, the X axis points toward the Sun, the Y axis lies in the ecliptic plane and points dusk-ward (opposite direction of the Earth's motion around the Sun), and the Z axis completes the right-handed orthogonal set (positive to the North). Therefore, during computations, OpenGGCM modifies the GSE coordinates by taking $X = -X_{GSE}$, $Y = -Y_{GSE}$, and $Z = Z_{GSE}$. Simulation domains typically run from $30R_E$ upstream the Earth and $300R_E$ down the tail. To complete the simulation box, the geometrical domain reaches $50R_E$ in the Y and Z directions in a typical run.

The grids used in the OpenGGCM simulations are called "stretched-cartesian" grids (*Raeder*, 2003), for example, as shown in Figure 6. The stretched-cartesian grids are adaptable to each particular simulation because one can define the regions where large definitions are desired. Grid cells can be taken smaller in areas of desired larger resolutions. These regions are often close to the Earth and the magnetotail.

There are other MHD codes used by the space science community, but due to the purpose of this paper they will be mentioned briefly. Such codes are the LFM (Lyon-Fedder-Mobarry) MHD code (*Lyon et al.*, 2004), from the Dartmouth College, the GUMICS (Grand Unified Magnetosphere Ionosphere Coupling Simulation) (*Janhunsen*, 1996; *Janhunen et al.*, 2012), from the Finnish Meteorological Institute, and the FV-TVD (Finite Volume Total Variation Diminishing) scheme, (*Tanaka*, 1994), from the Kyushu University, in Japan, and the MHD code that solves the MHD and Maxwell equations using the two-step Lax-Wendroff method (*Ogino et al.*, 1992), from the Nagoya University, Japan, the SPBU global MHD code from St. Petersburg State University, Russia, based on the TVD Lax-Friedrichs 2nd order numerical scheme (*Samsonov et al.*, 2016).

Tóth et al. (2007) simulated the propagation of a very fast CME and its impact on the magnetosphere. Numerical results were successfully compared to observations. The BATS-R-US code has been used to simulate the interaction between IP shocks and the Earth's magnetosphere as well (*Koval et al.*, 2006; *Ridley et al.*, 2006; *Samsonov et al.*, 2007; *Tóth et al.*, 2007; *Němeček et al.*, 2011; *Samsonov and Sibeck*, 2013; *Goncharov et al.*, 2015; *Samsonov et al.*, 2015). The BATS-R-US, OpenGGCM, GUMICS, and LFM models are readily available at the CCMC website (`ccmc/gsfc/nasa.gov`) for requests of runs on demand.

In this paper, we focus mostly on results obtained by the PPMRL-MHD (*Guo et al.*, 2005; *Guo and Hu*, 2007; *Wang et al.*, 2012), BATS-R-US (*Ridley et al.*, 2006; *Samsonov and Sibeck*, 2013; *Samsonov et al.*, 2015), and OpenGGCM (*Oliveira and Raeder*, 2014; *Oliveira*, 2015; *Oliveira and Silveira*, 2016) MHD codes. Results of the other MHD codes can be found in the abovementioned papers and in the review paper by *Wang et al.* (2013). A summary of the MHD and space weather models mentioned in this review can be found in Table 3 with a sample of their respective references and their availability at CCMC (`ccmc.gsfc.nasa.gov`) with their runs on demand.

5. Properties of shocks at 1 AU

The Solar Cycle (SC) 23, or SC23, began in May 1996 and ended in January 2008. The maximum monthly-averaged

Model Acronym	CCMC[1] availability	Sample reference
BATS-R-US	yes	*Powell et al.* (1999); *Ridley et al.* (2004); *Tóth et al.* (2007)
CTIM[a]	yes	*Fuller-Rowell et al.* (1996)
ENLIL[b]	yes	*Odstrčil and Pizzo* (1999); *Odstrčil* (2003)
FV-TVD	no	*Tanaka* (1994)
GUMICS	yes	*Janhunsen* (1996); *Janhunen et al.* (2012)
Lax-Wendroff method	no	*Ogino et al.* (1992)
LFM	yes	*Lyon et al.* (2004)
OpenGGCM	yes	*Raeder et al.* (2001a,b); *Raeder* (2003)
PPMLR	no	*Hu et al.* (2005); *Guo and Hu* (2007)
SPBU	no	*Samsonov et al.* (2016)
SWMF[c]	yes	*Tóth et al.* (2005, 2007)

Runs on demand available at `https://ccmc.gsfc.nasa.gov`.
[a]Coupled to OpenGGCM.
[b]Coupled to LFM.
[c]Coupled to BATS-R-US.

Table 3: Summary of the MHD models briefly described in this review. Sample references and CCMC availability are given.

sunspot number (SSN) observed on the Sun was approximately 180, and its minimum number was near 2 according to the list compiled by the Solar Influences Data Analysis Center (SIDC), available at `http://sidc.oma.be`. During SC23 the Sun unleashed the famous Halloween storms caused by very fast CMEs (*Lopez et al.*, 2004; *Echer et al.*, 2008a,b). The last superstorm of this solar cycle, that is, an event with Dst < -250 nT, occurred on 15 May 2005 (*Shi et al.*, 2017; *Oliveira et al.*, 2017). With few exceptions that occurred on St. Patrick's day of 2013 and 2015, with minimum Dst around -200 nT, there have been no significant storm events during the following solar cycle, SC24. The reason for this lack of superintense storms is due to an extremely low level of the solar activity in SC24. The current SC has been the weakest solar cycle in the past century (*Russell et al.*, 2010; *Pesnell*, 2015). The maximum SSN of SC24, below the average, had been predicted before its first minimum occurrence (see, e.g., *Pesnell*, 2015, and references therein).

The occurrence of IP shocks at the Earth's orbit is well known to roughly follow solar activity (*Lindsay et al.*, 1994; *Berdichevsky et al.*, 2000; *Echer et al.*, 2003; *Oh et al.*, 2007; *Kilpua et al.*, 2015; *Oliveira and Raeder*, 2015). Although most of these studies agree that CMEs drive most of the observed FFSs, most of them reported different conclusions for the driving of shocks by CIRs (see, e.g., discussion by *Kilpua et al.*, 2015, and references therein). Using a statistical sample of 679 FFSs and FRSs observed between 1995 and 2013 by the Wind, ACE and STEREO spacecraft, *Kilpua et al.* (2015) concluded that CMEs drove most of the FFSs, while the majority of the FRSs were driven by CIRs. CIR-driven FFSs did not follow any particular trend in relation to any solar cycle phases. *Singh et al.* (2017) found that moderate and intense CME- and CIR-driven geomagnetic storms that occurred during the ascending phase of SC24 were led by shocks.

As discussed in section 3, the main physical properties of IP shocks are the shock speed, the compression ratio, Alfénic and magnetosonic Mach numbers, obliquity angle, impact angle, and clock angle of the shock normal (in the YZ plane). These parameters change significantly for each type of shocks and, not surprisingly, for periods of maximum and minimum solar activity. It should be noted that, extreme events, such as the Halloween events, might lack solar wind and IMF data due to instrument saturation, and are typically left out of statistical analyses. However, due to their low occurrence rate, this should not affect the general conclusions of such studies, as the ones here reviewed.

Several properties of all IP shock types were studied for the early minimum phase and maximum phase of SC23 by *Echer et al.* (2003). They found that the majority of the 82 IP shocks observed at 1 AU were FFSs during solar minimum and solar maximum. In general, FRSs were more numerous during solar minimum, while SRSs showed approximately the same numbers during both periods. However, SFSs were not observed by *Echer et al.* (2003) during solar maximum. In general, all downstream parameters were larger than upstream parameters during solar maximum, except for the proton number density. These authors attributed this different parameter behavior to the fact that the heliospheric current sheet has a larger density in comparison to the background medium, and it is more stable. Alfén Mach numbers were similar in both periods because the reduced solar wind speed is compensated by the increased proton density during solar minimum. During solar maximum, *Echer et al.* (2003) found that the dynamic pressure was in general twice as strong as the thermal and magnetic pressures and most of the energy carried by IP shocks in that period was related to the kinetic energy.

Different conclusions were obtained by *Berdichevsky et al.* (2000), who investigated the properties of the first 42

fast shocks observed by Wind in its first 2.5 years in orbit (December 1994 to May 1997), and *Oh et al.* (2007), who studied 249 IP shocks seen by Wind and ACE at Earth's orbit in the period 1995-2001. As opposed to the *Echer et al.* (2003) conclusions, these authors found that shock Mach numbers and proton plasma density correlated well with solar activity for FFSs. In agreement with *Echer et al.* (2003), *Kilpua et al.* (2015) did not find any particular correlation between sunspot number levels and shock strengths, since the Mach number for both FFSs and FRSs driven by CMEs and CIRs presented similar results.

Some of these studies also agree on the distribution of the impact angles of CME- and CIR-driven shocks. *Berdichevsky et al.* (2000) reported that CME-driven shocks had a broader distribution of shock normals in the equatorial plane in relation to CIR-driven shocks. However, *Lindsay et al.* (1994), who studied 45 shocks observed by Pioneer Venus orbiter at 0.72 AU, concluded quite the opposite, which lines with the discussion given for Figure 1. In addition, *Kilpua et al.* (2015)'s results generally agreed with *Lindsay et al.* (1994)'s results. However, *Kilpua et al.* (2015) found that θ_{x_n} showed similar trends during solar minima and maxima. Finally, these authors showed that the occurrence rate of FFSs correlated with solar activity, while the occurrence rate of FRSs did not.

A statistical study of the properties of 461 FFSs was carried out by *Oliveira and Raeder* (2015), regardless of the shock drivers. They used Wind and ACE data to calculate shock parameters (see equations (1-9) in this review and also *Oliveira* (2017)). It was found that most shocks were almost perpendicular, i.e., θ_{B_n} was usually larger than 45°. The clock angle φ_{y_n}, the angle between the shock normal and the Y axis in the YZ plane, was found to follow the Parker spiral, since most shocks had φ_{y_n} in multiples of 45°. The majority of shocks had compression ratios between 1.0 and 1.5. The same occurred for the magnetosonic Mach number, which is consistent with previous observations (*Tsurutani and Lin*, 1985; *Echer et al.*, 2011). It should be noted that these results are in particular for shocks at the Earth's orbit.

According to empirical calculations carried out by *Tsurutani and Lakhina* (2014), the Mach number of a shock driven by an extremely fast CME would be ∼45. In fact, the Mach number of the extreme CME of 23 July 2012 was ∼21, calculated by *Riley et al.* (2016) with STEREO-A data. Although *Kilpua et al.* (2015) and *Oliveira and Raeder* (2015) showed that a few shocks had Mach numbers larger than 5, as also noted by *Tsurutani et al.* (2014), the reason of the lack of extreme shocks at 1 AU should be explained by their rare occurrence there or by a lack of solar wind/IMF observations during intervals of very disturbed solar wind conditions. Thus FFSs in the solar wind at 1 AU are predominantly weak shocks. For more details, see Figure 3 of *Oliveira and Raeder* (2015) and the corresponding discussion there.

For this review, the most important results for shock properties obtained by *Oliveira and Raeder* (2015) are

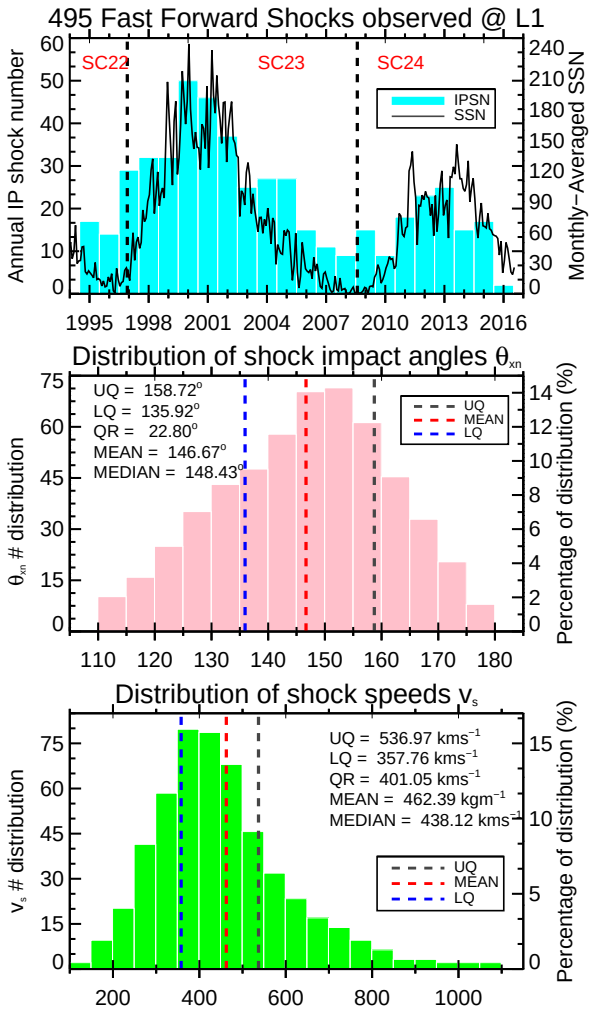

Figure 7: Properties of 495 fast forward interplanetary shocks observed by ACE and Wind in the time period January 1995 to January 2016, an extension of the shock list provided by *Oliveira and Raeder* (2015). Upper panel: bars, annual FFS distribution, black line: monthly averaged SSN. Middle panel: shock impact angle distribution. Lower panel, shock speed distribution.

shown in Figure 7. The top panel shows the number of registered FFSs between 1995 and 2016 and the corresponding time series of monthly-averaged SSNs. The second panel displays the distribution of shocks as a function of the impact angle θ_{x_n}. These shocks were almost frontal shocks since most shock normals had θ_{x_n} larger than 135° and are consistent with earlier ACE observations (*Wang et al.*, 2009, 2006). The third panel shows the distribution of shocks with the shock speed. Most shocks had speeds larger than 400 kms^{-1}, with average of 467 kms^{-1}. These results indicate that IP shocks at 1 AU are usually weak and strike the magnetosphere almost head-on.

The angle θ_{B_n} of shocks driven by CMEs and CIRs do not follow any particular trend with solar activity (*Kilpua et al.*, 2015). These authors showed that, in general, the larger the obliquity, the more numerous the shocks. Even though they used the criterium $B_2/B_1 \geq 1.2$, they argue that, due to their rarity, only a few quasi-parallel shocks,

if any, were ruled out. The only exception found by *Kilpua et al.* (2015) is that there are fewer almost perpendicular shocks ($80° < \theta_{B_n} < 90°$) for CIRs. *Oliveira and Raeder* (2015) found very similar results for the case in which the shock drivers were not discriminated.

The shock list of *Oliveira and Raeder* (2015) was used to study geomagnetic activity triggered by IP shocks with different inclinations. Substorms were studied by *Oliveira and Raeder* (2015) and nightside auroral power intensity by *Oliveira et al.* (2016). The results obtained by these studies will be reviewed later in this paper.

6. Modeling impacts of head-on shocks

Most MHD simulations in the past involving IP shock impacts on the Earth's magnetosphere were conducted assuming the shock normal vector parallel to the Earth-Sun line. Therefore, the subsequent compression was always symmetric. In this section some particular results obtained from studies of head-on shock impacts are reviewed.

The interaction of an IP shock with the magnetosphere begins when the IP shock collides with the bow shock. As noted above, most IP shocks are fast forward, while the bow shock is a stationary FRS. The interaction between the two shocks is a Riemann problem which can be solved using the RH conditions (*Grib et al.*, 1979). In a most simple case, when the IMF lies in the shock front plane, this interaction modifies the IP and bow shocks and creates a contact discontinuity between them (*Ivanov*, 1964; *Dryer et al.*, 1967; *Shen and Dryer*, 1972; *Dryer*, 1973; *Grib et al.*, 1979). For more realistic conditions, e.g., when the IMF was directed along the Parker spiral, *Grib* (1982) in an analytical 1-D solution, *Yan and Lee* (1996) in 1-D and *Samsonov et al.* (2006, 2007); *Samsonov and Sibeck* (2013) in 3-D numerical MHD solutions showed that the interaction between the two shocks at the Sun-Earth line resulted in: a modified FFS moving further ahead into the magnetosheath, a slow forward expansion wave, a contact discontinuity, a SRS, and a slightly modified bow shock. All these discontinuities, including the modified bow shock, after the interaction moved earthward in the Earth's frame. *Samsonov et al.* (2006) noted that the slow forward expansion wave, contact discontinuity and SRS usually propagate through the magnetosheath with similar speeds because the phase velocity of slow waves tends to zero if their wavevector is directed perpendicular to magnetic field and the contact discontinuity tends to diffuse, therefore the three discontinuities may form a single compound discontinuity extended in time. It would be true, at least, if we use observations in the magnetosheath with a relatively low time resolution of several seconds made relatively close to the origin of the discontinuities at the bow shock.

Šafránková et al. (2007a,b); *Pallocchia et al.* (2010); *Pallocchia* (2013) presented several events in which the compound discontinuity was observed in the magnetosheath. A main specific property of this discontinuity is a decrease

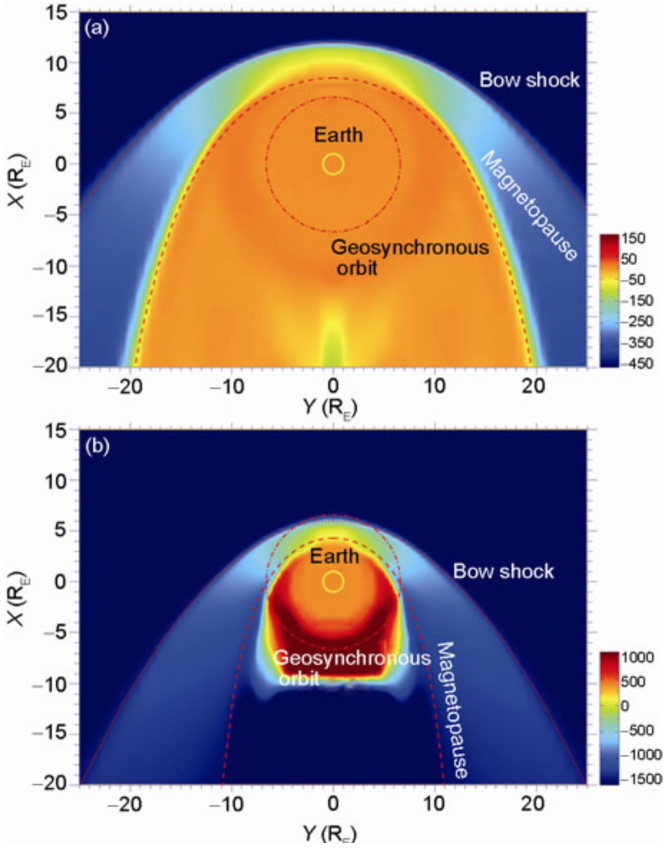

Figure 8: Magnetosphere large-scale structures as represented by the plasma velocity V_x in the equatorial plane for (a), undisturbed magnetosphere, and (b), 4 minutes after the violent shock impact. Note that due to the shock impact the bow shock and dayside magnetopause moved to regions smaller than $6.6R_E$, or within the geosynchronous orbit. After *Wang et al.* (2012)

of the temperature observed in all the events. Through the same discontinuity, the density decreases, the magnetic field magnitude whether increases or keeps nearly the same, and the velocity does not change at all. According to numerical simulations (e.g., *Yan and Lee*, 1996), the predicted slow forward expansion wave and SRS in a typical case are weak and bring only slight variations of MHD parameters, while the contact discontinuity brings significant changes of the density and temperature which are usually observed (but sometimes like smooth variations rather than a sharp discontinuity) downstream of the FFS.

Numerical MHD simulations conducted by *Samsonov et al.* (2006) also predicted that the modified FFS in the magnetosheath became weaker than in the solar wind and moved with a smaller speed, as confirmed by observations (*Koval et al.*, 2005, 2006).

The interaction between IP shocks and magnetopause launche a very weak fast shock or fast wave moving antisunward (Earthward in the subsolar region) through the magnetosphere (*Samsonov et al.*, 2007), while the dayside magnetopause also moves Earthward and the magnetic field magnitude in the magnetosphere gradually increases. As noted by *Grib et al.* (1979) and *Grib* (1982), a fast rar-

efaction wave is reflected back into the magnetosheath, but the 3-D MHD simulations (*Samsonov et al.*, 2007) show that this wave insignificantly changes the magnetosheath flow and probably is rapidly dumped.

In addition to the global magnetospheric compression, another immediate response to IP shock impacts is an enhancement of large scale FACs (field-aligned currents) between the magnetosphere and ionosphere (*Cowley*, 2000; *Zesta et al.*, 2000; *Oliveira*, 2014). Since the electric conductivity along the field lines is high, the magnetospheric currents can easily close through the ionosphere, at about 120 km altitude, forming a joint MI current system. When the solar wind plasma partly penetrates through the dayside magnetopause (usually for a southward IMF), it creates an electric potential drop between the magnetospheric flanks. Being projected along the field lines into the ionosphere, this potential results in a dawn-to-dusk ionospheric electric field. The electric currents flowing parallel to the electric field are called the Pedersen currents, and the currents flowing perpendicularly both to the horizontal electric field and vertical magnetic field are called the Hall currents (see, e.g., *Cowley*, 2000, for a comprehensive review). In the ionosphere, the MI currents depending on solar wind conditions can form three current systems (from high to low latitudes): Region 0 (R0), Region 1 (R1), and Region 2 (R2) FACs.

Several authors investigated FAC enhancements caused by the interaction of head-on IP shocks with the magnetosphere using numerical MHD simulations (*Keller et al.*, 2002; *Fujita et al.*, 2003a,b; *Luhmann et al.*, 2004; *Ridley et al.*, 2006; *Guo and Hu*, 2007; *Samsonov et al.*, 2010; *Wang et al.*, 2012; *Oliveira and Raeder*, 2014; *Oliveira and Silveira*, 2016; *Shi et al.*, 2017). For example, *Keller et al.* (2002) used the BATS-R-US model to simulate the impact of a solar wind dynamic pressure pulse (with an increase of density, but constant speed) on the magnetosphere. This pressure pulse results in a large magnetospheric compression and intensification of the MI currents. For a small constant northward IMF B_z, they predicted the intensifications of two current systems. First the high-latitude two-cell current pattern with the same polarity and position as northward B_z(NBZ) currents are amplified (*Araki*, 1977; *Moretto et al.*, 2000), then another current system with an opposite polarity (the same as R1 currents) is amplified at a little lower latitude. Similar results were obtained in other MHD simulations as well (e.g., *Fujita et al.*, 2003a; *Ridley et al.*, 2006; *Samsonov et al.*, 2010).

Strong FAC enhancements are readily detected by global simulations of extreme events. *Ridley et al.* (2006) used solar wind input conditions corresponding to a very strong CME-driven IP shock which led to a great magnetospheric distortion as in the famous Carrington event in 1859 (*Tsurutani et al.*, 2003; *Li et al.*, 2006). For the solar wind input conditions, the simulations used results of a CME modeled by *Manchester et al.* (2006) with BATS-R-US. The CME shock was purely frontal. In this event, the density increases from 40 to 150 cm^{-3}, while the IMF B_z decreases from less than 10 to almost -200 nT leading to a great magnetospheric compression with the magnetopause approaching to the inner numerical boundary of the code at $2.5R_E$.

In contrast, results of theoretical and empirical investigations as reported by *Tsurutani et al.* (2003) showed a different picture. In a more realistic scenario, calculations would produce a jump in density from a nominal value of 5 to the limit of 20 cm^{-3}. Later on, *Tsurutani and Lakhina* (2014) calculated the limit of the inward magnetopause motion and found $\sim 5R_E$, even though they considered a speed of 2700 kms^{-1}, much larger than the speed of 1500 $kms^{-1}$for the CME simulated by *Manchester et al.* (2006) and *Ridley et al.* (2006). Indeed, a closest to the Earth magnetopause position reached after the impact of a fastest CME with a speed of 3000 kms^{-1} near the Sun was reported by *Hoffman et al.* (1975) to be $\sim 5.2R_E$, in an excellent agreement with the *Tsurutani and Lakhina* (2014) results. Therefore, as pointed out by *Ridley et al.* (2006), the extreme $2.5R_E$ position should be explained by the unusually high solar wind density that was assumed to occur upstream of this particular shock. Similar consclusions were drawn by *Ngwira et al.* (2014), who simulated another extreme event as well.

In their simulation, *Ridley et al.* (2006) also noted the appearance of a secondary reflected shock moving sunward through the dayside magnetosphere and magnetosheath whose initiation and motion was later investigated and explained by *Samsonov et al.* (2007), *Samsonov et al.* (2010), and *Samsonov and Sibeck* (2013). Figure 8 shows the magnetosphere response to a very similar Carrington-like CME conducted with the PPMLR-MHD code by *Wang et al.* (2012). That figure shows that the subsolar magnetopause and bow shock shift inward to 4.3 and $6.0R_E$ respectively. A Space Weather event of this magnitude may pose severe risks to human assets that orbit Earth at the geosynchronous orbit, such as GPS satellites (*Lakhina et al.*, 2012), since they would be outside the magnetosphere protection and directly exposed to interplanetary radiation. In the *Wang et al.* (2012) simulation run, the cross polar cap potential drop increased by about 80 times after the artificial CME impact.

Figure 9 illustrates the temporal evolution of ionospheric currents simulated by *Ridley et al.* (2006). Immediately after the CME impact, a set of opposite currents appears in the high latitude ionosphere. Although they are similar to the NBZ currents, that is, same location and shape, these currents are not classified as NBZ currents due to their distinctive driving mechanism. Approximately 10 seconds later, the simulated currents travel pole-ward and become highly deformed. In the following 10 seconds, such currents almost fade away. At 04:46:40, another set of currents in the same direction as the R1 currents propagate toward the terminator along a near latitude line as opposed to the anti-sunward propagation of the first opposite current system. *Ridley et al.* (2006) associated this large R1-like current system to a high displace-

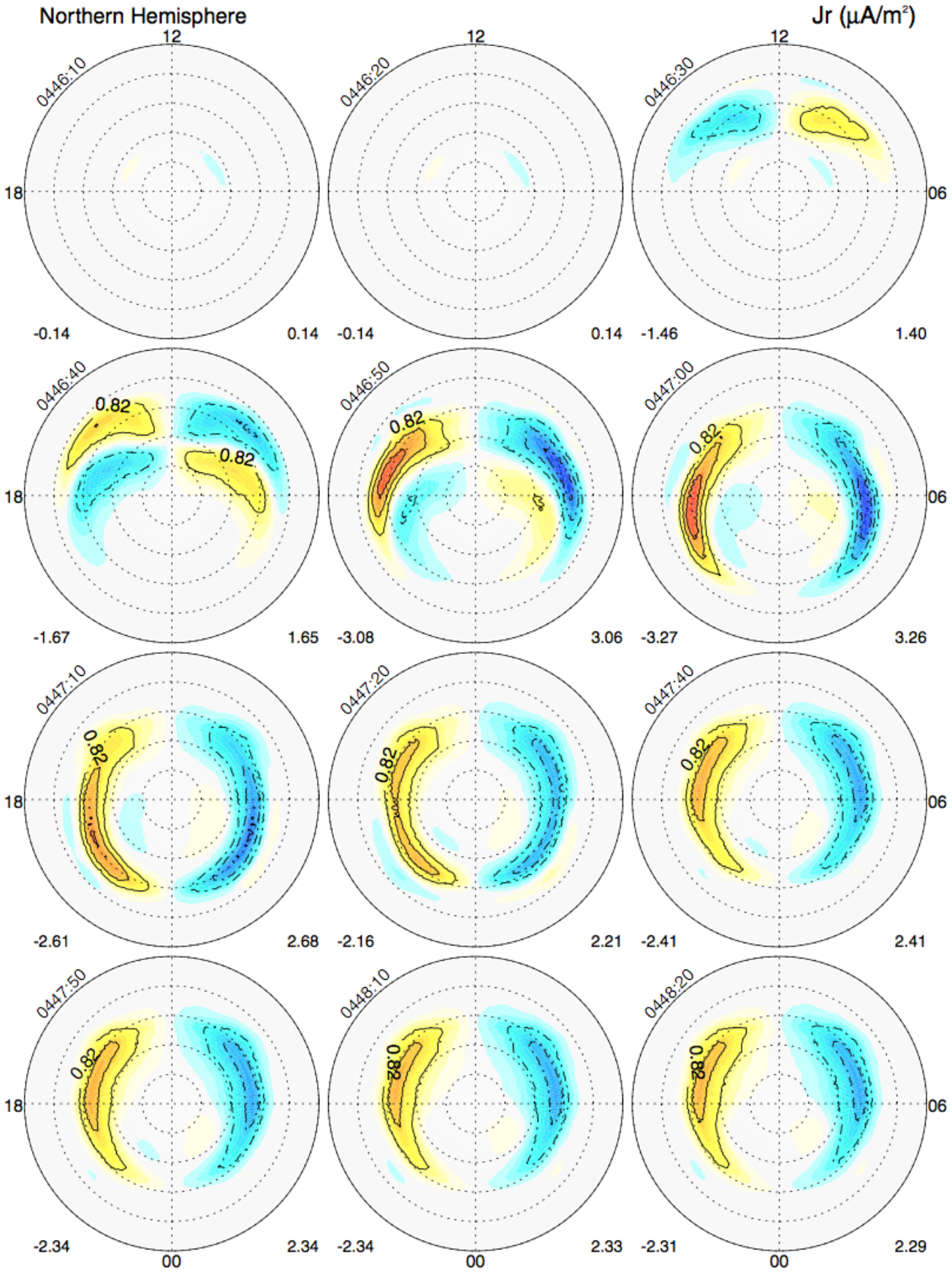

Figure 9: Field-aligned currents caused by the very strong CME-driven interplaneraty shock simulated by *Ridley et al.* (2006). Figure from *Ridley et al.* (2006).

ment of either the bow shock or magnetopause caused by the violent shock impact. In the subsequent 1-2 minutes this current system stays strong and steady because the magnetosphere was highly compressed by the CME shock. The symmetry of these current systems is associated with the head-on impact of the shock. *Guo and Hu* (2007) ran the PPMLR-MHD code for the impact of a moderate shock on the magnetosphere with no IMF B_z. These authors noted the appearance of an anomalous R1 current system as well, which flowed oppositely to the R1 current system. This anomalous R1 current formed at noon, developed and then moved toward the evening side until it vanished. *Guo and Hu* (2007) concluded that such a response depends on the strength of the IP shock.

The successive intensification of the two MI current systems in the MHD simulations well agrees with the SI^+ signatures well known from ground magnetic observations. At high latitudes, the sudden impulse consists of the preliminary impulse (which can be produced by the electric currents of NBZ type) and of the main impulse (which is related to the electric currents of R1 type). These two-pulse structure is superimposed by a step-like increase of the horizontal magnetic field resulted from a global magnetospheric compression. A comprehensive review of ground magnetic field variations resulted from IP shock impacts was performed by *Araki* (1994). Although MHD models can in general well reproduce the ground SI^+ signatures and predict a similar behavior of the MI currents, different authors interpret the generation of the transient currents in the magnetosphere in different ways.

A mechanism of the current system generation responsible for the preliminary and main impulses was initially proposed by *Tamao* (1964a) and *Tamao* (1964b) and further developed by *Araki* (1994). According to these authors, the current system of preliminary impulse can be formed if the electric current flowing along the fast shock (fast wave) front in the magnetosphere closes through the ionosphere. The FACs during the main impulse are generated by a duskward electric field connected with enhanced magnetospheric convection in the compressed magnetosphere (*Araki*, 1994). However these qualitative models do not specify the position of the magnetospheric dynamo for either current system.

Fujita et al. (2003a) analyzed results of global MHD simulations and, following the ideas of Tamao and Araki, concluded that the preliminary impulse current is a part of the current system formed by a dawn-to-dusk current flowing along the magnetopause and a dusk-to-dawn current flowing along the shock front in the magnetosphere. *Fujita et al.* (2003b) defined two stages constituting the main impulse phase. In the first stage, the generation of the FAC system continues in the same way as during the preliminary impulse. In the second stage, the magnetospheric dynamo is supposed to be on the tail-ward side of the cusp. Another generation mechanism also proposed by *Fujita et al.* (2003b) is related to the compression of the magnetospheric flanks and this idea is in general consistent with Araki's suggestion.

Keller et al. (2002), using results of MHD BATS-R-US simulations, found that the preliminary impulse FAC is connected with the pressure perturbation in the equatorial plane near the magnetospheric boundary. The second FAC in their simulations is supposed to be explained by the mode conversion of the fast compression wave in the magnetosphere following the initial ideas of *Tamao* (1964a) and *Tamao* (1964b).

Finally, *Samsonov et al.* (2010), using another simulation run of the same BATS-R-US model, suggested their own explanations of both FACs. They investigated a case with an artificial IP shock during northward IMF conditions. In that case, the magnetic reconnection occured at a high-latitude region behind the cusp, and they found a dynamo region for the first FAC located near the magnetopause just inward of the high-latitude reconnection site. The second FAC (responsible for main impulse) was related to vortices predicted by several MHD models (see also, e.g., *Slinker et al.* (1999) or *Fujita et al.* (2003b)) on the both flanks near the equatorial plane.

A mechanism of generation of these vortices and corresponding MI currents was suggested by *Samsonov and Sibeck* (2013) using another MHD run. An essential part of this mechanism is the reflection of fast compressional wave (shock) in the inner magnetosphere thoroughly investigated by *Samsonov et al.* (2007). In the *Samsonov and Sibeck* (2013) simulations, this reflection occurred when the compressional wave contacted with the impenetrable inner numerical boundary, however in reality this inner boundary may correspond to either the plasmasphere or ionosphere. Using a simplified 1-D MHD model at the Sun-Earth line, *Samsonov et al.* (2007) obtained that about 70% of the incident energy may penetrate into the plasmasphere and the rest 30% reflects back in the outer magnetosphere. Using THEMIS observations, *Samsonov et al.* (2014) showed that IP shock impacts really result in the magnetic field increase and velocity oscillations both outside and inside the plasmasphere. The reflection of the compressional wave and a sunward flow near the Sun-Earth line is the first stage of the formation of vortices. So the vortices first appear in the dayside inner magnetosphere, but then move tailward and outward through the dawn and dusk flanks. The reflected compressional wave moves sunward through the dayside magnetosphere, successively interacts with the magnetopause and bow shock and stops their inward motion. In particular, *Šafránková et al.* (2007b) presented a few real events with double bow shock crossings observed after an IP shock impact in which the sequence of discontinuities and variations of plasma and magnetic field parameters were consistent with MHD predictions. The MHD model also well reproduced the observations in the event presented by *Pallocchia et al.* (2010). Later, *Pallocchia* (2013) presented another observational confirmation that a fast reversed wave moving sunward occurred in the magnetosheath a few minutes after the initial IP shock passage.

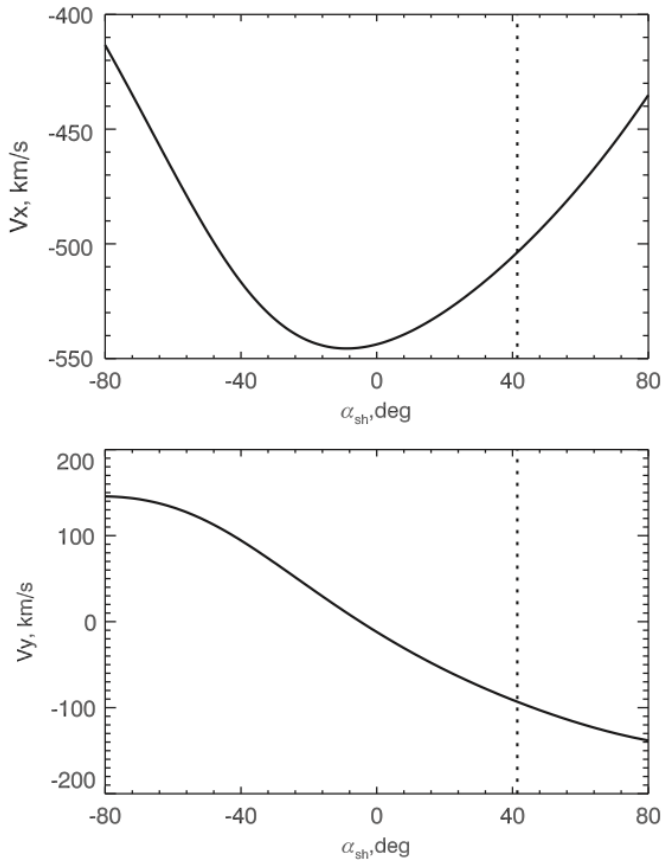

Figure 10: Dependence of the downstream velocity components in the Earth's frame on the shock normal angle α_{sh} (θ_{x_n} in this paper) if the upstream conditions $V_x = -400$ kms^{-1} and $V_y = 0$ are imposed. Vertical dotted lines mark the conditions used for the numerical simulation. After *Samsonov* (2011).

In several papers, the speed of fast compressional wave (or sudden impulse) in the inner and outer magnetosphere and in the magnetotail was estimated both from observations and MHD simulations (*Patel*, 1968; *Sugiura et al.*, 1968; *Wilken et al.*, 1982; *Huttunen et al.*, 2005; *Andréeová and Přech*, 2007; *Andréeová et al.*, 2008; *Keika et al.*, 2008). Most authors obtained that the speed of a sudden impulse in the magnetosphere is higher than that in the solar wind, varying from 700 to 1000 kms^{-1} or more, that is consistent with the fast wave speed in the magnetosphere. However, the speed in the magnetotail according to some observations may be of the order of the solar wind speed or even less (*Huttunen et al.*, 2005).

We can briefly mention here that the impact of IP shocks excites the magnetospheric pulsations, mostly standing Alfvén waves, over the entire frequency range (*Takao and Matsushtta*, 1967). And MHD models can reproduce the process of generation of ULF Alfvén waves from a compressional wave reasonably well (*Claudepierre et al.*, 2010; *Samsonov et al.*, 2011).

7. Asymmetric magnetospheric compression in response to impacts of inclined shocks

The interaction of IP shocks inclined with respect to the Sun-Earth line with the bow shock was investigated by *Grib and Pushkar* (2006). They considered an IP shock that first strikes the dawnside flank and numerically solved the RH conditions for different points along the bow shock surface. They found that the structure of discontinuities propagating through the magnetosheath after the shock-shock collision slightly varied between the dawn and dusk flanks, but it necessarily included a modified FFS and a contact discontinuity. An average density near the contact discontinuity was about 16% higher (in their particular case) on the dawn side than on the dusk side.

Andréeová et al. (2008) used the GUMICS numerical MHD model to simulate the magnetospheric response to the IP shock of 09 November 2002. According to the *Oliveira and Raeder* (2015) IP shock catalogue, that shock had a modest inclination of ∼15° in relation to the GSE X line in the equatorial plane. *Andréeová et al.* (2008) noted that because of the shock inclination the compression of the magnetic field was somewhat stronger in the dayside magnetosphere adjacent to the IP shock front than on the opposite side.

Samsonov (2011) investigated the interaction of an inclined shock with the Earth's magnetosphere using numerical simulations as well. He used a 3-D numerical MHD code to study the propagation of an artificial IP shock through the magnetosheath. That code solves MHD equations and makes corrections to keep $\nabla \cdot \mathbf{B} = 0$ constraint using the projection scheme (*Tóth*, 2000). The author considered the case in which the shock normal lay in the equatorial plane with the angle θ_{x_n} equal to 41° and the IMF directed along the Parker spiral. Since the numerical method keeps $\nabla \cdot \mathbf{B} = 0$, the author could change both the IMF B_x and B_y on the upstream solar wind boundary as follows from the RH conditions. Moreover, solving the RH equations, *Samsonov* (2011) found a dependence of the velocity components downstream of the IP shock in the Earth's frame on the θ_{x_n} angle. Figure 10 is a reproduction of Figure 2 from his paper which illustrates this dependence. Using this figure, *Samsonov* (2011) concluded that the ratio of the Y-directed (azimuthal) to X-directed (radial) solar wind dynamic pressure changed from 3–4% for $\theta_{x_n} = 40°$ to 10–12% for $\theta_{x_n} = 80°$. In particular, he obtained the downstream $V_y = -94$ kms^{-1} if the upstream $V_y = 0$ in the simulated case with $\theta_{x_n} = 41°$ was previously imposed.

Thus a strongly inclined shock may result in sudden impulses of different amplitudes on dawn and dusk ground stations at close latitudes. The magnetic field enhancement should be larger on the flank which was compressed first. In the same paper, *Samsonov* (2011) discussed a train of MHD discontinuities which followed the FFS on the dawn and dusk magnetosheath flanks.

Samsonov et al. (2015) studied the asymmetrical mag-

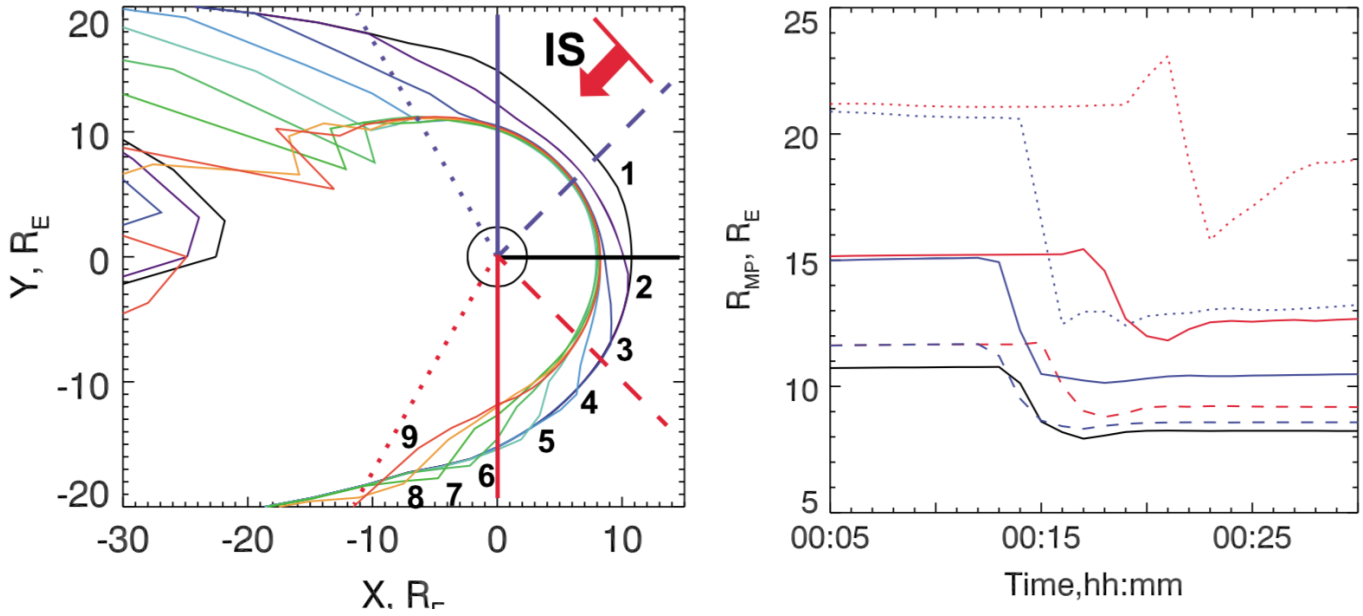

Figure 11: Left panel: equatorial cut of the magnetosphere. Lines from black to red indicate the positions of the magnetopause each minute beginning from the time of shock first impact the dusk magnetopause. Right panel: temporal variations of the magnetopause positions along several radial cuts (indicated by red/black/blue straight lines in the left panel). The uppermost dashed red line (a radial cut at 4 hr magnetic local time) illustrates the effect of magnetopause expansion before the compression. Taken from *Samsonov et al.* (2015).

netospheric compression also using numerical simulations but with the BATS-R-US global MHD code. Numerical computations were provided by CCMC. The authors analyzed a moderately strong IP shock with solar wind conditions very similar to those in *Samsonov* (2011). They imposed a shock with Alfvén Mach number $M_A = 4.45$ and $X = 2.84$, and the shock normal performed an angle of 41° with the GSE X axis in the equatorial plane. It led to a jump of the V_x component of the solar wind speed from -400 kms^{-1} to -505 kms^{-1} through the IP shock, while V_y changed from 0 to -94 kms^{-1}.

Figure 11 (left panel) shows the magnetopause positions in the equatorial plane obtained in the MHD simulations. The orientation of the IP shock normal is indicated by a red arrow in the upper right corner of the figure, and displays that the shock first strikes the duskside magnetosphere. Each color line represents the magnetopause position every minute beginning from the time when the shock just approached the magnetopause. The shock impact generates a stronger compression on the duskside. On the dawnside, the compression is weaker and preceded by a modest magnetopause expansion.

In addition to the asymmetric magnetospheric compression, *Samsonov et al.* (2015) explored a new phenomenon which can hardly be realized in simulations with head-on shocks. This is an expansion of the early morning magnetopause, i.e., on the opposite side of the shock impact, which occurs just 1-2 minutes before the compression. The uppermost dashed red line on the right panel of Figure 11 shows an overshoot of the magnetopause position, which indicates this expansion.

Although it may be difficult to check this numerical prediction with in-situ observations at the magnetopause flank, it can be more easily confirmed by ground magnetic data. Therefore *Samsonov et al.* (2015) used the SWMF model to simulate magnetic field variations at ground magnetometer stations artificially positioned in different local time regions. As expected, they observed overshoots in the ground horizontal magnetic (H) component consistently with the overshoot in the dawnside magnetopause position. In addition, they found an IP shock with a very similar inclination (see the 13 June 1998 event in the *Oliveira* (2015) appendix) which caused a very similar overshoot in the ground H component on the duskside, since the shock impacted on the dawnside magnetosphere. These results confirmed *Samsonov* (2011)'s predictions discussed above.

The possibility of magnetopause expansion before compression in response to a solar wind pressure pulse was first pointed out by *Kaufmann and Konradi* (1969). Moreover, the authors noted that a very inclined solar wind discontinuity can cause a large magnetospheric deformation on the opposite side than that from which the discontinuity came from. A very weak magnetospheric expansion before the global compression was also noted in the global MHD simulation with BATS-R-US by *Němeček et al.* (2011) on the nightside magnetopause in response to a head-on shock. The explanation of this phenomenon is that the speed of compressional waves in the magnetosphere is higher than the IP shock speed in the solar wind or magnetosheath, as discussed above. For example, the magnetosonic speed is usually about 1000 kms^{-1} inside the magnetosphere, while a moderate IP shock has a speed of 500 kms^{-1}. As a result,

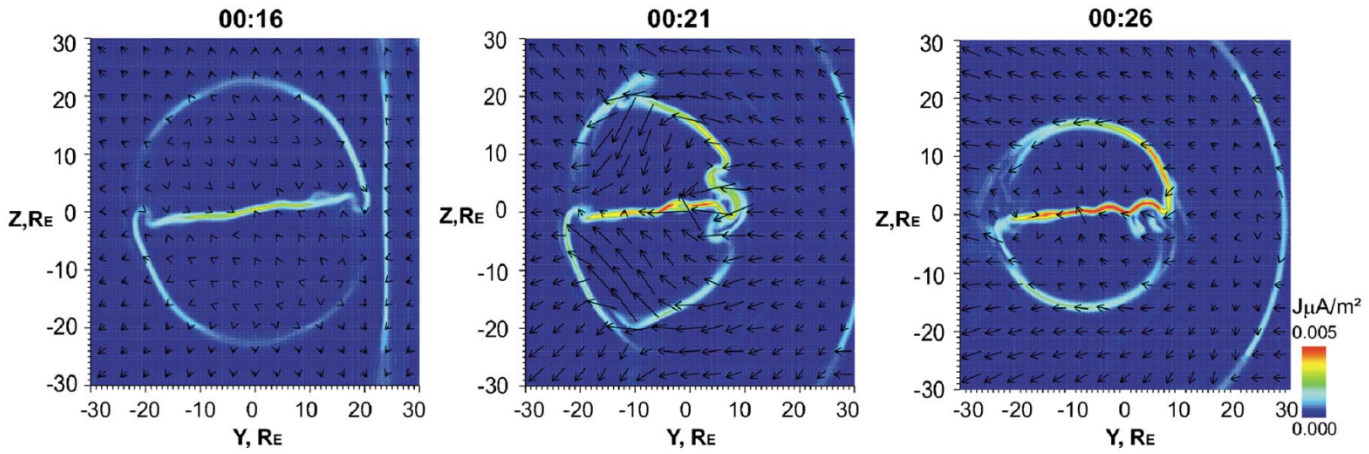

Figure 12: Electric current density color-coded and plotted in the YZ plane at X = $-30R_E$ down the tail. Arrows indicate velocity directions. After *Samsonov et al.* (2015).

the total pressure on the inner side of the magnetopause on nightside flanks increases slightly before the total pressure on the outer side, and the magnetopause initially moves outward.

Another interesting result obtained by *Samsonov et al.* (2015) corresponds to a large deformation of the magnetotail current layer during and after the inclined shock passage through the magnetotail. Figure 12 shows electric current density in the plane perpendicular to the Sun-Earth line at X = $-30R_E$ with a time lag between planes equal to 5 minutes. The left panel shows a slight deviation of the cross-tail current in relation to the ecliptic plane, probably due to a finite IMF B_y. The IP shock is seen on the right side as a vertical current sheet. After the shock impact, the magnetopause currents become very disturbed and both the magnetopause and bow shock move over $10R_E$ toward the midnight terminator. After the impact, the magnetopause deformations are relaxed, but the asymmetric shape continues to occur. *Samsonov et al.* (2015) attributed this large asymmetric effect to a high downstream V_y driven by the inclined IP shock, as predicted by *Samsonov* (2011).

A similar deflection of the far magnetotail caused by the passage of a very inclined IP shock was observed by *Grygorov et al.* (2014). That IP shock, with similar conditions to the shock simulated by *Samsonov* (2011) and *Samsonov et al.* (2015), occurred on 07 December 2003. *Grygorov et al.* (2014) took advantage of fortuitous mutual locations of the ACE (upstream), GEOTAIL and CLUSTER (bow shock flanks), and Wind (X = $\sim -240R_E$ down the tail) spacecraft for that event. Using data from these multiple satellites, *Grygorov et al.* (2014) found that the shock had a large inclination in both ecliptic and meridional planes corresponding to about 50°. They concluded that a very likely large magnetotail deflection of 30° was related to a large V_y solar wind speed, in accordance with predictions of *Samsonov* (2011) and *Samsonov et al.* (2015). Further investigations of the interaction of IP shocks with different inclinations with the magnetotail will bring about new understanding of magnetospheric physics, for example, the comprehension of substorm triggering mechanism (see, e.g., *McPherron*, 2015, and references therein).

8. Impact angle effects on geomagnetic activity

8.1. Ring current

The ring current is an electric current composed of electrically charged particles trapped in the Earth's magnetosphere (*Dessler and Parker*, 1959; *Sckopke*, 1966; *Carovillano and Siscoe*, 1973; *Daglis et al.*, 1999). The generation of the ring current results from the drift of these particles with energy 10-300 keV in the longitudinal direction. An intensification of the ring current during intervals of large magnetospheric disturbances, like magnetic storms, generates a horizontal magnetic field on the ground with an opposite orientation in comparison to the Earth's dipole field that may last for a few days (*Rostoker et al.*, 1997). Therefore, during the main phase of magnetic storms, ground magnetometers register a large negative perturbation of the H component. The Dst and SYM-H indices, discussed in section 4.2, correspond to a conventional measure to quantify geomagnetic storm intensities. According to a very common classification found in the literature, geomagnetic storms become intense when Dst(SYM-H) reaches a minimum value of −100 nT or less (*Gonzalez et al.*, 1994). The Dst and SYM-H indices can also be obtained from the World Data Center as well.

By using Wind solar wind plasma parameters and IMF data, *Jurac et al.* (2002) investigated 107 FFSs from 1995 to 2000. They focused primarily on the θ_{B_n} angle. Figure 13 extracted from *Jurac et al.* (2002) displays the relationship between geoeffectiveness triggered by IP shocks and θ_{B_n}. The upper panel shows the Dst index plotted as a function of θ_{B_n}. According to their results, quasi-perpendicular shocks, i.e., shocks with θ_{B_n} close to 90°, are associated with more intense geomagnetic storms. The

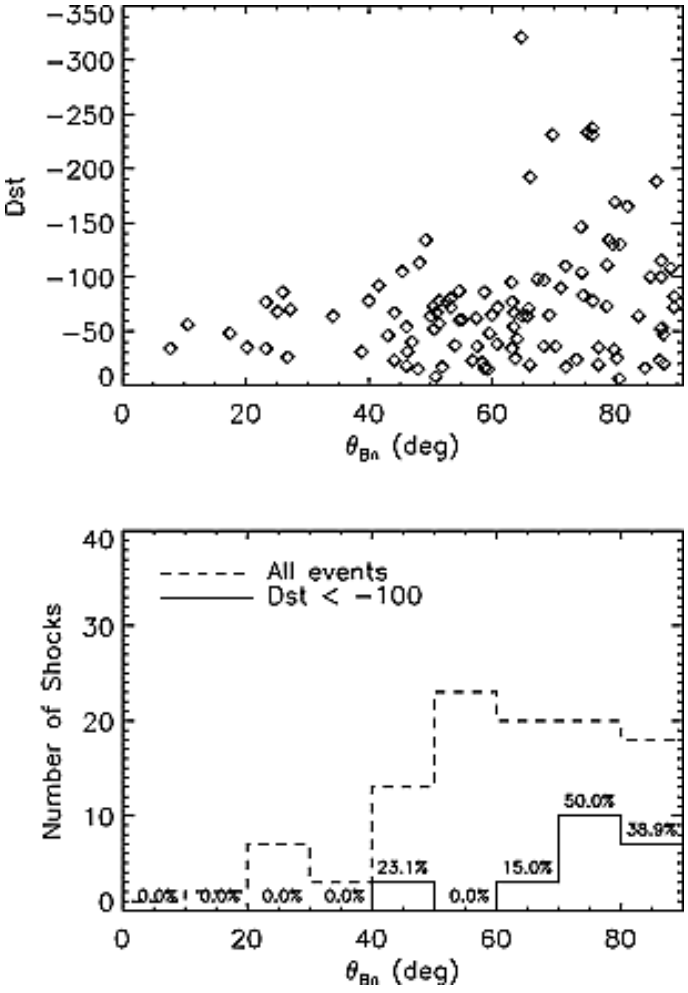

Figure 13: Upper panel: Dst strength plotted against θ_{B_n}, the angle between the upstream magnetic field vector and the shock normal. Almost perpendicular shocks (θ_{B_n} close to 90°) were followed by more intense geomagnetic storms. Lower panel: percentage of all shocks (dashed) and shocks associated with intense geomagnetic storms (Dst < -100 nT, solid). In the latter case, most intense geomagnetic activities were associated with almost perpendicular shocks. Figure taken from *Jurac et al.* (2002)

lower panel in Figure 13 indicates that most shocks have $\theta_{B_n} > 40°$ (dashed line). Interestingly, cases with Dst < -100 nT, or intense geomagnetic storms, following IP shocks (solid line) occured more frequently for $\theta_{B_n} > 70°$, and no events are reported for $\theta_{B_n} < 40°$. As a result, *Jurac et al.* (2002) concluded that quasi-perpendicular shocks were preceeded by storms more intense than those storms preceeded by quasi-parallel shocks because the fronts of quasi-perpendicular shocks are nearly parallel to the IMF, making it more likely to produce southward IMF B_z components in the downstream region. Therefore, variations of parameters through IP shocks play an important role in triggering geomagnetic activity followed by shock impacts. These results confirmed theoretical predictions of geomagnetic activity followed by the impacts with shocks with larger geomagnetic field of perpendicular shocks in comparison to their oblique counterparts (*Grib et al.*, 1979; *Grib*, 1982).

8.2. SI$^+$ rise times and magnetic field at geosynchronous orbit

The first dramatic response to an IP shock impact observed on the ground is a rapid increase of the SYM-H index. This is the onset of an SI$^+$ event, whose rise time is defined by the time interval between the SI$^+$ onset and its maximum amplitude (*Dessler et al.*, 1960). *Maeda et al.* (1962) observed that SI$^+$ rise times generally range from 2 to 10 minutes, and are centered at 4 minutes. Nevertheless, no assumptions were made about the influence of shock inclinations on SI$^+$ rise time.

Magnetic field variations on the Earth's surface during SI$^+$ events are a result of the superposition of hydromagnetic waves generated in different magnetospheric regions. Following to this assumption, *Dessler et al.* (1960) and *Ondoh* (1963) suggested that SI$^+$ rise times can be obtained from the difference between the arrival times of hydromagnetic waves generated in the magnetotail and in the subsolar magnetopause. *Nishida* (1964) also supposed that the time taken for an IP shock or discontinuity to pass through the geoeffective magnetosphere determines SI$^+$ rise times. Another aspect of this phenomenon is the relation between SI$^+$ rise times and amplitudes. In general, SI$^+$ events with large amplitudes are associated with short rise times (*Araki et al.*, 2004). However, none of these studies connected the angle of impact of IP shocks on the magnetosphere with SI$^+$ rise time determinations.

The effects of IP shock inclinations on the SI$^+$ rise time followed by a shock impact were first pointed out by *Takeuchi et al.* (2002). They observed an unusually long SI$^+$ rise time associated with an IP shock observed by Wind on 15 December 1995, shown in the left column of Figure 14, and another event on 01 November 1997 with a standard SI$^+$ rise time, shown in the right column of the same figure. Figure 14 compares these two events. Usually after an IP shock impact, the total pressure in the magnetosphere as well as the SYM-H index grow rapidly during a few minutes, however in the first case the pressure increases from 100 pPa to 170 pPa in approximately 30 minutes, as seen from GEOTAIL data at X = $-17.4 R_E$ in the magnetotail, shown in Figure 14(b). The SYM-H index also increases very gradually in 13 nT during the same time interval. The second event illustrates a more typical behavior when both the total pressure in the magnetotail and SYM-H index increase during about 7 minutes.

Takeuchi et al. (2002) introduced the concept of "geoeffective magnetopause" to explain the gradual increase of the dynamic pressure in the inner magnetosphere. The effect of a compression at the distant tail magnetopause is not detected on the Earth's surface, and there is a border on the nightside, within which the geoeffective magnetopause is confined. *Takeuchi et al.* (2002) argued that inclined IP shocks would take more time to sweep by the geoeffective magnetopause. However, by inspecting the IP shock normal associated with the 15 December 1995

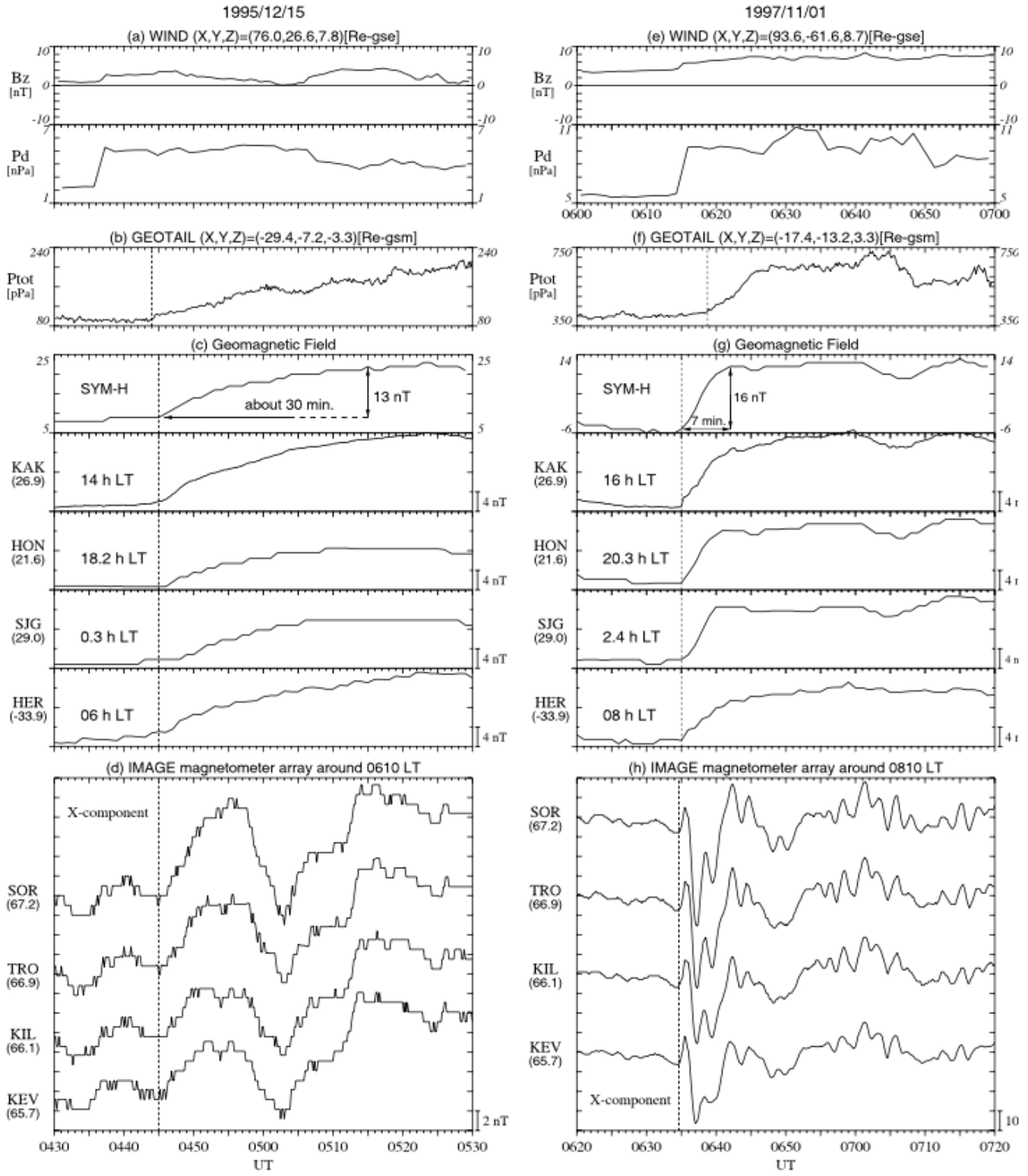

Figure 14: Comparison between two shock-related events, after *Takeuchi et al.* (2002): a typical SI^+ rise time, right column; an unusuall SI^+ rise time, left column.

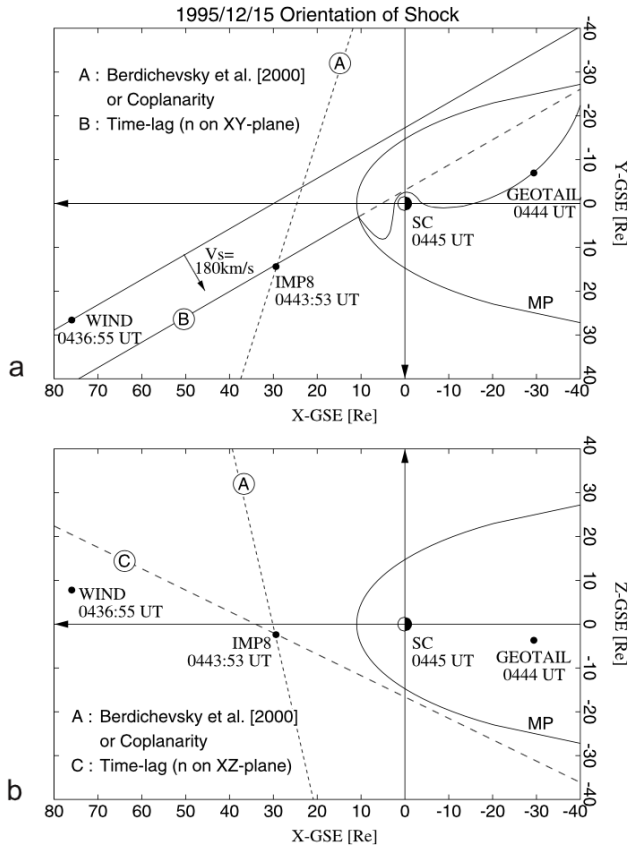

Figure 15: Shock frontal lines as calculated by *Berdichevsky et al.* (2000) (dashed) and *Takeuchi et al.* (2002) (solid) in the equatorial plane: equatorial plane (upper panel), and merisional plane (lower panel). The shock inclination in the equatorial plane was higher according to *Takeuchi et al.* (2002). This high angle explains an unusually high SI^+ rise time observed by ground stations after an IP shock impact on 15 December 1995.

shock published previously by *Berdichevsky et al.* (2000), they noticed that the angle of the shock normal with the Sun-Earth line in the equatorial plane should be larger than ∼11° as calculated by *Berdichevsky et al.* (2000). Figure 15 shows the difference in the shock front inclinations in the GSE XY and XZ planes as predicted by *Berdichevsky et al.* (2000) and found by *Takeuchi et al.* (2002). Later, *Oliveira and Raeder* (2015) obtained a shock inclination of about 30° for this particular event, which supports *Takeuchi et al.* (2002)'s explanation for their unusually high SI^+ rise time observation. Thus, the shock inclination is an important factor for accurate space weather forecast.

By using ACE and Wind satellite data from 1995 to 2004, *Wang et al.* (2006) reported that, in a survey of nearly 300 FFSs, 75% of them were followed by SSC's observed on the ground, confirming previous results (*Chao and Lepping*, 1974; *Smith et al.*, 1986). They found that the shock speeds were in the range 350-650 kms^{-1}, and that the average shock speed was near 500 kms^{-1}, and that most shocks had impact angles greater than 135°. Most shock impact angles were in the range 135°-180°, which suggests that shocks at 1 AU are almost frontal shocks.

In relation to shock geometry, *Wang et al.* (2006) statistically found that the shock impact angle plays an important role in determining the SI^+rise time, as previously suggested by observation (*Takeuchi et al.*, 2002) and simulations (*Guo et al.*, 2005, discussed later). They grouped their events according to the shock speed and impact angle. When the shock speed (shock strength) was fixed, the closer the shock normal was to the Sun-Earth line, the shorter was the SI^+ rise time. A similar behavior was found when they fixed the shock inclination and changed the shock speed. The faster the shock was, the shorter was the SI^+ rise time. Thus, *Wang et al.* (2006) confirmed previous MHD simulation results by *Fowler* (2005) which showed that faster IP shocks led to shorter SI^+ rise times. The highest correlation in *Wang et al.* (2006) occurred when the shock speed was fixed and the impact angle varied.

More recently, *Selvakumaran et al.* (2017) performed a statistical analysis of 179 FFSs and arrived at the same conclusions as *Takeuchi et al.* (2002) and *Wang et al.* (2006) about the relation between the shock impact angle and the SI^+ rise time. *Selvakumaran et al.* (2017) also found that shocks with slow speeds were associated with larger SI^+ rise times. In addition, these authors found that shocks associated with magnetic clouds produced events with small SI^+ rise times, while that time was larger for IP shocks associated with ejecta. *Selvakumaran et al.* (2017) investigated the role of SI^+ rise times in terms of radio emissions of CMEs as well. The authors classified CMEs as Radio Quiet (RQ) if they did not lead to detectable type II radiation in the metric decameter-hectometric and as Radio Loud (RL) otherwise (see, e.g,. explanations in *Gopalswamy et al.*, 2010). *Selvakumaran et al.* (2017) found that the CME speed better correlated with the SI^+ rise time for RL CMEs than for RQ CMEs, regardless the shock impact angle. By using the FV-TVD model to run numerical simulations, these authors also concluded, as expected, that CME-driven shocks with smaller shock impact angles produced higher geomagnetic activity. They observed such effects by means of intensifications of MI current systems, and downstream magnetic field and dynamic pressure.

The shock normal orientation may also play an important role in driving asymmetric responses of the magnetic field at geostationary orbit ($6.6R_E$). This aspect of IP shock geoeffectiveness was studied by *Wang et al.* (2005) with numerical MHD simulations. By using the PPMLR-MHD code, they showed that the magnetic field response at $6.6R_E$ depended upon the θ_{x_n} angle. They simulated one frontal shock and three inclined shocks. In the case of the frontal shock, the magnetic field at geostationary orbit increased nearly symmetrically, as expected, with maximum increase at 12 hours of local time. In the case of the inclined shocks, the magnetic field response was distinctly asymmetric. Since that shock impinged the bow shock on the duskside, the geostationary magnetic field

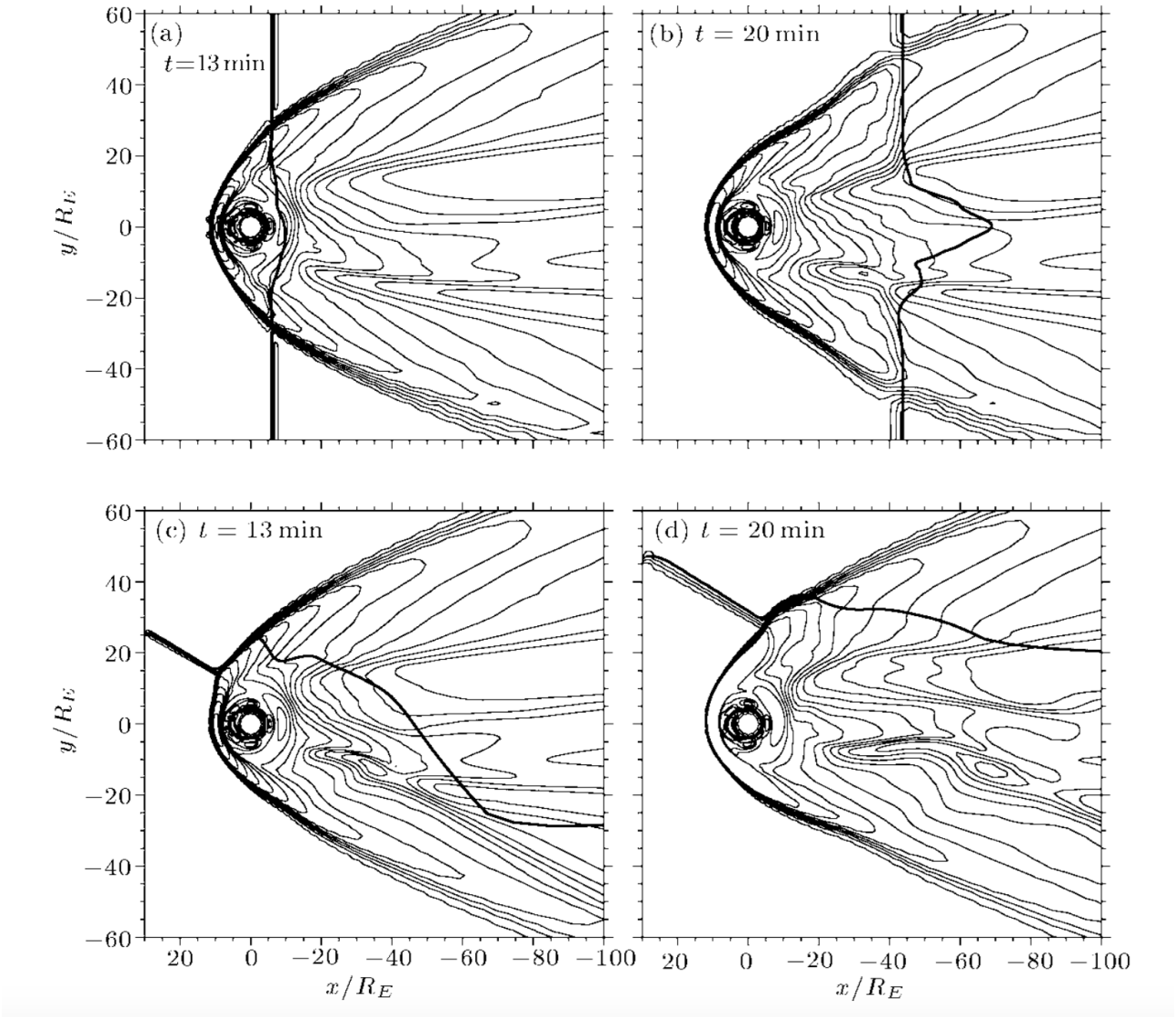

Figure 16: Contours of the thermal pressure resulted from global MHD simulations conducted by *Guo et al.* (2005) for two IP shocks with different shock normal inclinations. The case with a frontal IP shock is illustrated by two top panels, and the case with an inclined shock by two bottom panels. Shock normals in the both cases lie in the equatorial plane. The time to compress the geoeffective magnetopause is larger for the inclined shock than for the frontal shock.

enhancement was the largest at around 14 hours of local time, in agreement with previous results of *Takeuchi et al.* (2002) and *Guo et al.* (2005).

8.3. Field-aligned currents, cross-polar cap potential, auroral precipitation

The observational result reported by *Takeuchi et al.* (2002) stimulated the investigation of magnetospheric response to inclined IP shocks through global MHD simulations. *Guo et al.* (2005) performed a global numerical MHD simulation with different shock normal orientations to study the MI response followed by the shock impacts. Using the PPMLR-MHD code, they simulated two cases in which the IP shocks had different shock normal orientations while the IMF was directed along the Parker spiral and $B_z = 0$. In order to investigate the shock inclination effects only, the downstream dynamic pressure in both cases was held to the constant value of 2.98 nPa. Both shocks had similar strength, as represented by their Mach numbers. In the first case, the shock normal was parallel to the Sun-Earth line, and in the second case the shock normal was inclined to this line with an angle of 60°.

Figure 16, from *Guo et al.* (2005), displays the results of both runs. The four panels show thermal pressure contours in the XY plane in the frontal case (top row) and the inclined case (bottom row). In both cases, the bow shock moves along the X line from the position X = 13.8R_E to X = 11.7R_E, and the magnetopause moves from X = 10.1R_E to X = 9.0R_E due to the impact of the shocks. Note that the final magnetopause and bow shock positions are de-

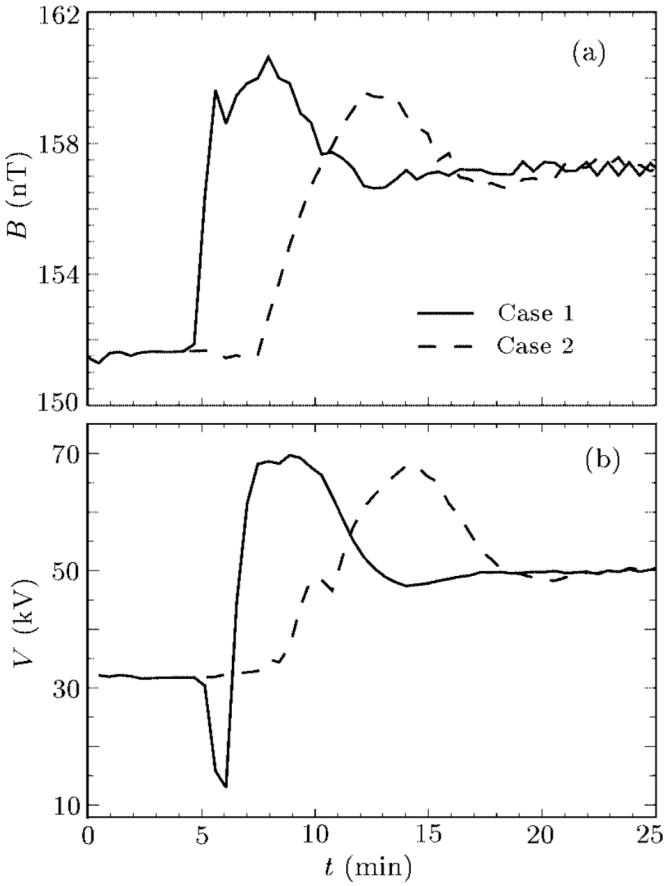

Figure 17: Total magnetic field (upper panel) and ionospheric potential difference (lower panel) evolutions due to IP shock impacts after *Guo et al.* (2005). In both cases, a frontal shock (solid line) and an inclined shock (dashed line) reached about the same final quasi-steady state. However, the system impacted by the inclined shock took a longer time to reach its final state.

termined by the downstream dynamic pressures which are similar in both cases. However, the inclined shock takes longer to sweep over the magnetosphere due to a larger distance covered to reach the tail, as suggested previously by *Takeuchi et al.* (2002). Similar results were also obtained by *Wang et al.* (2005) and *Selvakumaran et al.* (2017).

The MI response to the IP shock impacts with different impact angles simulated by *Guo et al.* (2005) is documented by Figure 17. The upper panel shows total magnetic field (B) response, and the lower panel shows the ionopheric potential difference (V) response. In both panels, solid lines indicate results for the frontal shock, and dashed lines indicate results for the inclined shock. The peaks in B and V coincide well in time and are shorter in the case of the frontal shock (δt ~4 min) than in the case of the inclined shock (δt ~10 min). *Guo et al.* (2005) attributed this more than twice time delay due to the fact that the inclined shock spends more time to travel in the magnetosphere in comparison to the frontal shock. This simulation result confirmed the suggestion of *Takeuchi et al.* (2002) related to the shock impact role in magnetospheric compression and subsequent geomagnetic response. Similar simulation results were obtained by *Selvakumaran et al.* (2017) for the SI^+ rise times followed by shocks with different impact angles.

Oliveira and Raeder (2014) investigated the geoeffectiveness of IP shocks with different orientations. These authors conducted numerical MHD simulations by using the OpenGGCM code to simulate the impact of three FFSs on the magnetosphere. *Oliveira and Raeder* (2014) used the RH jump solutions for oblique and perpendicular shocks summarized by *Oliveira* (2017) to calculate dowstream conditions from upstream conditions for two moderate shocks and one strong shock. The shocks were classified as follows: a moderate inclined oblique shock (IOS-1, θ_{x_n} = 30°, θ_{B_n} = 51°, M_A = 3.7), a strong inclined oblique shock (IOS-2, θ_{x_n} = 30°, θ_{B_n} = 45°, M_A = 7.4), and a moderate frontal perpendicular shock (FPS, θ_{x_n} = 0°, θ_{B_n} = 90°, M_A = 3.7). The strong shock was twice as stronger as the moderate shocks.

In all cases, the shock normals lay in the meridional (XZ) plane. The two inclined shock normals were directed toward the south, whereas the shock normal of the frontal shock was parallel to the X line. That made the two inclined shocks hit the magnetosphere in the Northern Hemisphere, and the frontal shock hit the magnetosphere well frontally. Since the IOSs were oblique shocks, the upstream and downstream IMF B_x components were not null. The same was applied to the solar wind V_z components. In the FPS case, however, these same conditions were not imposed. For this reason, both upstream and downstream IMF B_z components were directed strictly southward. Therefore the downstream B_z for the frontal shock was slightly more negative than those for the inclined shocks.

Results for that simulation are shown in Figure 18. That figure shows variations in the total magnetic field calculated as $\Delta B(t') = B(t + \Delta t)$ - $B(t)$, where Δt = 30 seconds, in intervals of 3-6 minutes from t = 17:00 min to t = 29:00 for the IOSs and from t = 18:30 min to t = 29:30 min for the FPS. ΔB is color coded with positive variations in red and negative variations in blue. The left column shows results for the IOS-1, the middle column for the IOS-2, and the right column for the FPS.

The magnetosphere responses to these IP shocks show very distinctive features when comparing the inclined shocks with the frontal shock. In the case of the IOSs, due to the shock inclination, the first bow shock-shock interaction occurs in the Northern Hemisphere behind the cusp at ~ 17:00 min. Three minutes later, for IOS-1 and IOS-2, high-speed Alfvén waves are launched due to the shock impact in the northern lobe and propagate obliquely ahead the shock toward the tail. At t = 20:00 min, it is evident that ΔB is stronger for the IOS-2. At t = 23:00 min, the IOSs sweep over the southern magnetosheath and at t = 26:00 min the tail is deflected toward the south by about 2-3R_E in both cases. Finally, at t = 29:00 min the shock completely paases over the magnetosphere. The main con-

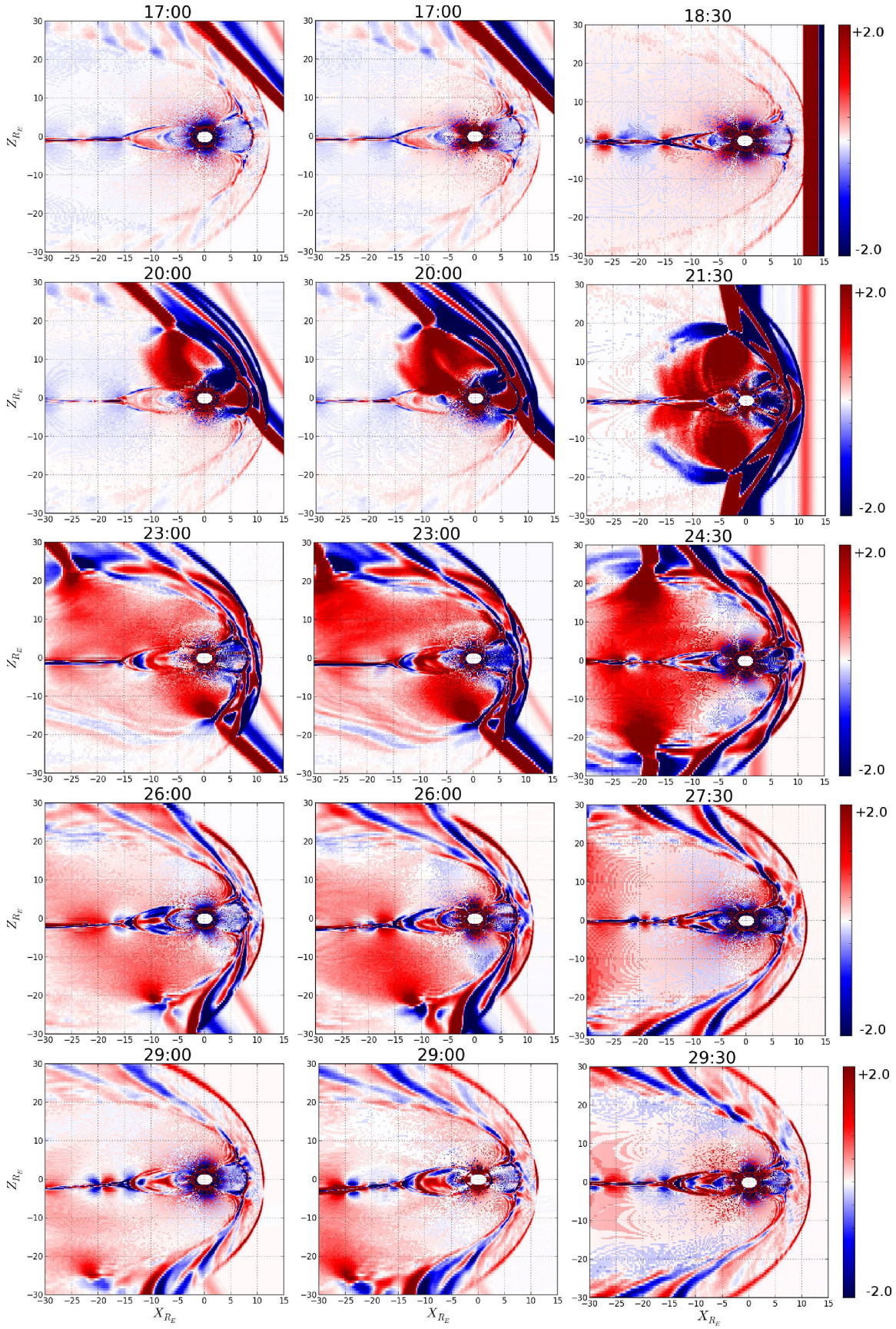

Figure 18: Total magnetic field difference (ΔB) calculated in 30 second increments for: IOS-1, left column; IOS-2, middle column; and FPS, right column. Figure extracted from *Oliveira and Raeder* (2014).

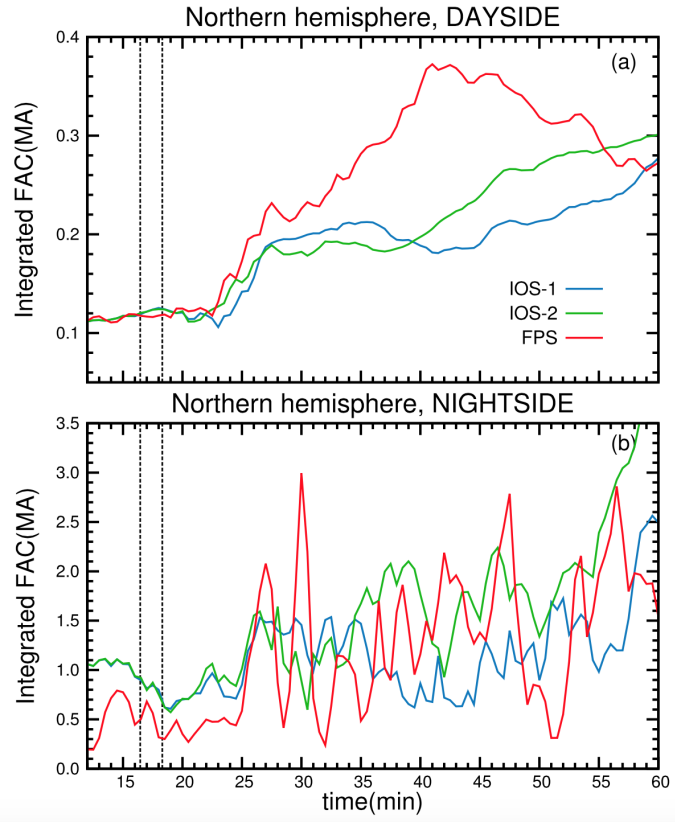

Figure 19: OpenGGCM simulation results for the integrated field-aligned currents (FACs) generated by the shock impacts on the Northern hemisphere (a), dayside, and (b), nightside. Lines in blue and green represent the moderate (IOS-1) and strong (IOS-2) inclined shocks. Lines in red indicate the moderate (FPS) frontal shock. Figure from *Oliveira and Raeder* (2014)

sequence of the shock inclination in both IOS cases is the asymmetric transient compression of all magnetospheric regions and magnetotail displacement.

In the FPS case, however, such transient asymmetric compression does not take place. The first bow shock-shock interaction occurs at t = 18:00 min at the subsolar region. Due to the symmetric impact, the northern and southern parts of the magnetosheath become highly turbulent, and Alfvén waves race ahead the shocks toward the tail symmetrically in both lobes (t = 21:30 min). Three minutes later, the FPS completes its passage through the magnetosphere. As opposed to the inclined cases, at t = 29:30 min, the tail is visibly more compressed in relation to the inclined shocks, even more compressed than the strong IOS-2. Also, the tail is not deflected during the transient FPS compression. The main difference occurs in magnetospheric transient leading to different geomagnetic responses, as we will show below.

Figure 19 shows results for the FACs integrated in the Northern Hemisphere above 50° magnetic latitude in the dayside (upper panel) and nightside (lower panel) for all three simulations. In both panels, lines in blue indicate IOS-1 results, lines in green IOS-2 results, and lines in red, FPS results. The first vertical dashed line at 17 minutes indicates the impact time of the inclined shocks, while the second vertical dashed line, at 19 minutes, marks the impact time of the frontal shock.

In the dayside, Figure 19a, the ionosphere is fairly steady before shock impact, with FACs showing magnitudes close to 0.12 MA. FACs start to increase 4 minutes after the FPS impact and 6 minutes after the IOS-1 and IOS-2 impacts. In general, the ionosphere shows a slightly weaker response to the IOS-1 in comparison to the IOS-2 since the latter was stronger than the former. However, the moderate FPS triggers a stronger and faster ionospheric response. *Oliveira and Raeder* (2014) attributed this effect to the symmetry of the frontal shock, as well as to its perpendicularity, favorable conditions for maximizing the negative B_z and V_x downstream components.

The nightside ionosphere shows more interesting results. As reported by *Oliveira and Raeder* (2014), the nightside ionosphere shows a stronger FAC density variation in regions between 65° and 75° magnetic latitude, in the same sense as ΔB discussed above (see their Figure 2). This is consistent with a typical substorm signature (*Akasofu*, 1964; *McPherron*, 1991). In contrast, the inclined cases do not show such effects, except some random FAC variations in mid-latitude regions, with the IOS-2 triggering a stronger response than IOS-1.

The quantification of those nightside FAC variations are seen in Figure 19b. Before the impact of all shocks, FACs showed some variations being stronger in both IOS cases. After the shock impact, both IOS-associated FACs show neither particular trend nor significant increases, with the IOS-2 triggering stronger FAC enhancements in comparison to the IOS-1. On the other hand, in the FPS case, FACs started to oscillate near 7 minutes after the shock impact with a period of about 5 minutes. Given the period, such oscillations are presumably related to ULF waves (*Hughes*, 1994). *Oliveira and Raeder* (2014) suggested that the transient FPS compression may excite cavity modes in the magnetosphere (*Samson et al.*, 1992; *Hughes*, 1994). This was likely due to the fact that the waves that converged on the tail and compressed the plasma sheet from there launching a wave back toward the nightside magnetosphere, which in turn excited the cavity mode. This effect has yet to be observed with experimental data.

The cross-polar cap potential (CPCP) and the integrated diffusive precipitating auroral energy flux (DPAEF) responses to the impact of the same IP shocks simulated by *Oliveira and Raeder* (2014) are shown by the upper and lower panel of Figure 20, respectively. Details for CPCP and DAPEF computations can be found in *Raeder et al.* (1998) and *Raeder* (2003). The blue, green and red lines indicate the results for the IOS-1, IOS-2, and FPS, respectively. Both CPCP and and DAPEF show very similar trends, except that the ionospheric response to the FPS impact is higher than the IOS impacts, particularly in the case of auroral precipitation. DAPEF starts to in-

crease at approximately t = 23:00 min reaching a peak of ∼370 GW in the subsequent 30 minutes, consistent with substorms signatures (*Akasofu*, 1964; *McPherron*, 1991). Again, *Oliveira and Raeder* (2014) used arguments of symmetric magnetospheric compressions and maximization of IMF/solar wind parameters in the downstream region to explain these simulation results.

As discussed in detail by *Oliveira and Raeder* (2014), all MI responses described above depend heavily upon the shock normal orientation. They also suggest that, in some cases, the shock normal orientation may play a more important role in comparison to the shock strength itself. In the case of the auroral substorm triggering, the role of preconditioning, i.e., whether the IMF B_z is southward or not, has already been discussed in the literature (*Craven et al.*, 1986; *Zhou and Tsurutani*, 1999, 2001; *Tsurutani and Zhou*, 2003; *Yue et al.*, 2010; *Echer et al.*, 2011; *Liu et al.*, 2013). However, as pointed out by *Jurac et al.* (2002), almost perpendicular shocks, i.e., shocks with θ_{B_n} near 90°, should be more geoeffective. Considering the shock geometry simulated by *Oliveira and Raeder* (2014), the FPS was highly favored because all of the IMF vector was directed southward behind and ahead the shock, since the B_z component does not share jumps with the other components. In addition, due to the head-on impact, the downstream IMF B_z component underwent the largest change. This was a favorable scenario for the release of electromagnetic energy stored in the tail toward the ionosphere and the subsequent substorm triggering there. The *Oliveira and Raeder* (2014) predictions were confirmed later with substorm response by *Oliveira and Raeder* (2015) and nightside auroral power response by *Oliveira et al.* (2016). Their results will be discussed below.

8.4. Substorms

Substorms can result from the release of magnetospheric energy due to tail reconnection which propagates from the magnetotail to the high latitude regions of the ionosphere (see, e.g., *Tsurutani and Meng*, 1972; *Pudovkin*, 1991). Substorms are different from storms in terms of response magnitude and temporal/spatial distributions. The former occurs in time interval of no more than a few hours and is generally located in the polar regions, whereas the latter lasts longer and is more pronounced in the equatorial region. The main energy source of substorms is the polar ionospheric electric field, whereas the ring current is the energy source for geomagnetic storms (*Pudovkin*, 1991; *Gonzalez et al.*, 1994). The only visual manifestation of substorms is the polar aurora.

The development of auroral substorms is well known since the pioneer observations using all-sky cameras by *Akasofu* (1964). Generally, auroral substorms are divided in three stages: initial or preliminary phase, expansion phase and recovery phase. During the preliminary phase, auroral arcs move fast toward the equator. Auroral arcs move poleward during the expansion phase, and during the recovery phase, the auroral oval returns to its steady and original position.

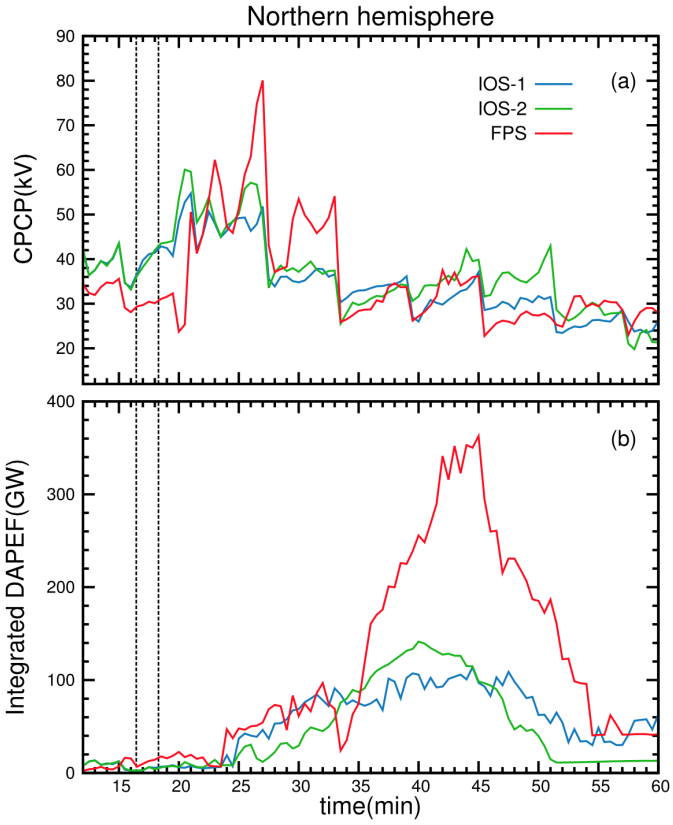

Figure 20: Upper panel: CPCP (kV); lower panel: norther hemisphere integrated DAPEF (GW) for the IOS-1 (blue lines), IOS-2 (green line), and FPS (red line). The first vertical dashed line indicates the instance of impact of the inclined shocks, and the second vertical dashed line indicates the same for the frontal shock. Figure from *Oliveira and Raeder* (2014).

The intensity of magnetospheric substorms depends heavily on the coupling between the solar wind and the magnetosphere, being highly amplified when IMF B_z is directed southward. The most common way to measure the intensity of magnetospheric substorms is through geomagnetic indices, particular by the AL index, described in section 4.2. Magnetospheric substorms are powered by increased electric fields applied to the conductive ionosphere. The strength of the AL index is highly correlated with the coupling function $\varepsilon = VB^2 \sin^4(\Theta/2)$, where Θ is the IMF clock angle (*Perreault and Akasofu*, 1978; *Akasofu*, 1979; *Kan and Lee*, 1979; *McPherron and Baker*, 1993).

Given the substorm morphology mentioned above and the fact that substorm intensity is highly correlated with auroral electrojet intensifications, the AL index may not be in some cases a good choice to measure the intensity of substorms triggered by IP shock impacts due to the limited number of ground stations used to construct the AL index. As discussed in section 4.2 and carefully detailed by *Oliveira and Raeder* (2015), the SuperMAG SML index corresponds to a more straightforward choice. The

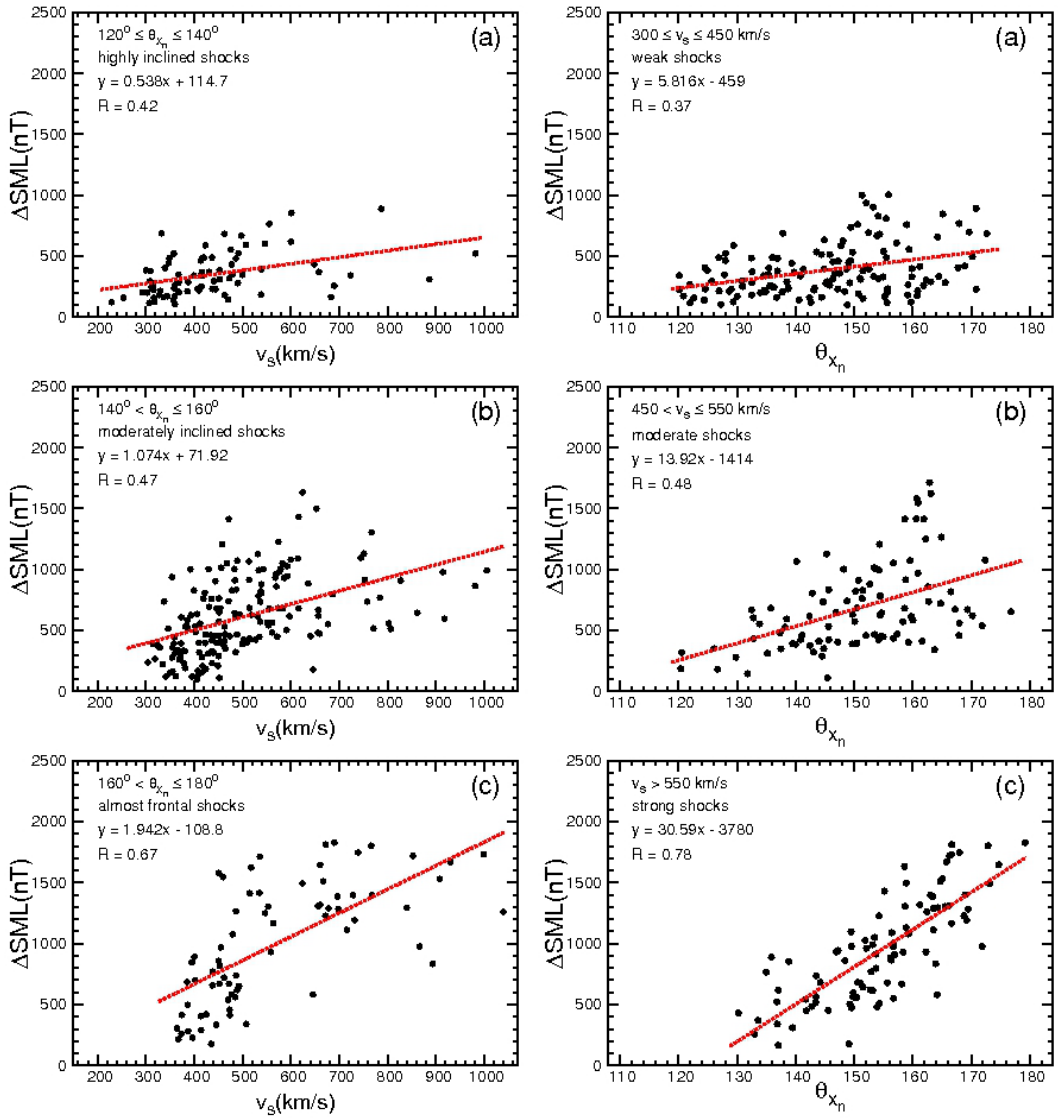

Figure 21: Jumps in SML triggered by IP shock impacts plotted in function of the shock speed V_s. The events were binned in three different groups in terms of the shock orientation in relation to the X-line: Figure 4(a), $120° \leq \theta_{x_n} \leq 140°$ (highly inclined shocks), Figure 4(b), $140° \leq \theta_{x_n} \leq 160°$ (inclined shocks), and Figure 4(c) $160° \leq \theta_{x_n} \leq 180°$ (almost frontal shocks). The shocks are more geoeffective for strong (high speed) and almost frontal shocks. Figure from *Oliveira and Raeder* (2015).

Oliveira and Raeder (2015) results are discussed below.

The results of the modeling work of *Oliveira and Raeder* (2014) were verified by *Oliveira and Raeder* (2015) with experimental data. As discussed in section 5, *Oliveira and Raeder* (2015) used an IP shock data base with over 450 events to correlate substorm activity, characterized by the SuperMAG SML index, with the shock impact angle and shock speed. The minimum SML index value was obtained for each event as the first minimum in a time interval of two hours after each shock impact. If there were other peaks inside this time interval, only the first one was considered for the correlation analysis.

The *Oliveira and Raeder* (2015) results are shown in Figure 21, a combination of their Figures 4 and 5. In that figure, shock speed V_s and shock impact angle θ_{x_n} are grouped in different ways to explore shock impact angle and shock strength influences on the substorm intensity. The left column of Figure 21 shows ΔSML, the difference between the SML peak and its background value before shock impact, in dependence on the shock speed separated by the impact angle: highly inclined shocks $120° \leq \theta_{x_n} \leq 140°$ (upper panel), moderately inclined shocks $140° \leq \theta_{x_n} \leq 160°$ (middle panel), and almost frontal shocks $160° \leq \theta_{x_n} \leq 180°$ (lower panel). The three panels in the right column of Figure 21 show θ_{x_n} plotted against ΔSML separated into the following groups of shock speed: upper panel, weak shocks ($300 \leq V_s \leq 400$ kms^{-1}); middle panel, moderate shocks ($450 \leq V_s \leq 550$ kms^{-1}); and bottom panel, strong shocks ($V_s \geq 550$ kms^{-1}).

The figure clearly reveals the correlation between the

shock speed and shock impact angle. If V_s is held constant, the correlation between θ_{x_n} and ΔSML increases when V_s increases. As seen in the top panel of the right column, highly inclined shocks tend to have low speeds. Only few shocks have speeds larger than 550 kms^{-1}. Shocks in this category trigger low geomagnetic activity, since only a few events are associated with ΔSML $>$ 500 nT. Moderately inclined shocks tend to be more geoeffective, since more events trigger substorms with ΔSML $>$ 500 nT, and fewer with ΔSML $>$ 1000 nT. In contrast, in the category of almost frontal shocks, more events are associated with ΔSML $>$ 1000 nT. Most shocks have $V_s > 550$ kms^{-1}. In general, the larger the shock speed and the more frontal the shock, the higher the shock geoeffectiveness followed by shock impact. The correlation coefficient increases from 0.42 (highly inclined shocks), to 0.47 (moderately inclined shocks), and then to 0.67 (almost frontal shocks).

The arrangement of the data in the other way around, i.e., fixing shock speed and then correlating θ_{x_n} with ΔSML, shows slight differences compared with the previous approach. One difference is that the number of events is more evenly distributed. As shown in the top panel of Figure 21, left column, only two events triggered ΔSML responses larger than 1000 nT. Weak shocks do not present any preference for θ_{x_n}. In the case of moderate shocks, however, only a few events have $\theta_{x_n} < 140°$, and fewer more trigger geomagnetic activity with ΔSML $>$ 1000 nT. Strong shocks have a preference to have θ_{x_n} more aligned with the Sun-Earth line in comparison to the other categories. In respect to geoeffectivenes, near half of the shocks trigger events with ΔSML $>$ 1000 nT. In relation to the category of almost frontal shocks plotted as $V_s \times \Delta$SML, events in the strong category plotted as $\theta_{x_n} \times \Delta$SML are more clustered. Finally, similarly to the other categories, the correlation coefficients R increase with shock strength as well: R = 0.37 for weak shocks, R = 0.48 for moderate shocks, and R = 0.78 for strong shocks.

In general, these results confirmed the model predictions of *Oliveira and Raeder* (2014): the more inclined and stronger the shock, the higher the geomagnetic activity triggered by the shock impacts. See more details on this study in *Oliveira and Raeder* (2015) and *Oliveira* (2015).

8.5. Auroral power intensifications

Oliveira et al. (2016) used the SME index as a proxy for auroral power (AP) determinations. This choice was based on a relation obtained by *Newell and Gjerloev* (2011b). *Newell and Gjerloev* (2011b) calibrated the SME index with both Polar UVI instantaneous images and DMSP instantaneous maps to find correlations between SME and AP. Due to differences in time resolution, a better correlation was found between SME and AP as determined by Polar UVI. The linear relationship found by *Newell and Gjerloev* (2011b) is:

$$\mathrm{AP} = 0.048 \times \mathrm{SME} + 0.241 \times (\mathrm{SME})^{1/2}\,, \qquad (10)$$

In their statistical analysis, *Oliveira et al.* (2016) focused on sharp increases of the AP intensity resulting from IP shock impacts on the Earth's magnetosphere. Similarly to the *Oliveira and Raeder* (2015) work, they took a maximum of the SME index during a time interval varying from approximately a half to two hours after the IP shock impact. If there was more than one SME peak in the time interval, the first one was chosen as the maximum associated with the IP shock.

The results of the correlation between V_s, θ_{x_n} and ΔAP are shown in Figure 3 of *Oliveira et al.* (2016). In general, their results agree well with the *Oliveira and Raeder* (2015) results: the higher is the shock speed and the more frontal is the shock, the stronger is the auroral power increase. In addition, the results of that study support the argument of *Newell and Gjerloev* (2014) that the SME index is the most appropriate index to calculate nightside auroral power variations triggered by external drivers. These results confirmed previous analyses of *Oliveira and Raeder* (2014) and *Oliveira and Raeder* (2015) corresponding to the correlation between shock impact angles and geomagnetic activity triggered by shock impacts.

9. Summary and conclusion

In this paper, several aspects of IP shocks and their triggering of geomagnetic activity were discussed. In particular, the paper focused on a specific characteristic of IP shocks: the IP shock impact angle. The main points reviewed in this paper are summarized as follows:

9.1. Properties of shocks at Earth's orbit

The constant monitoring of solar wind and IMF parameters at 1 AU since December 1994 by Wind and since August 1997 by ACE brought about new perspectives and improved our knowledge of solar-terrestrial relations. Using almost two decades of data, several authors studied properties of IP shocks at L1. In this review paper, we discussed results of these works (*Echer et al.*, 2003; *Oh et al.*, 2007; *Kilpua et al.*, 2015; *Oliveira and Raeder*, 2015) and summarized them below.

The occurrence of IP shocks at 1 AU shows a good agreement with solar activity. All authors mentioned above agree that FFSs are more numerous during solar maxima than in solar minima. Several authors agree that CMEs are the primary driver of FFSs which occur more frequently during periods of large solar activity (*Lindsay et al.*, 1994; *Berdichevsky et al.*, 2000; *Jian et al.*, 2006a; *Oh et al.*, 2007; *Kilpua et al.*, 2015), but the relation between CIR-driven occurrence and solar activity was still obscure before *Kilpua et al.* (2015)'s work. *Kilpua et al.* (2015) showed that the shocks related to CIRs poorly correlated with sunspot numbers. Due to the unusually quiet behavior of the Sun in the current solar cycle (*Pesnell*, 2015), the IP shock number observed during the SC24 maximum phase (2014) was 15, as opposed to the same number at the

SC23 maximum, that was 50 (*Oliveira and Raeder*, 2015). Surprisingly, the number of IP shocks during the ascending phase of SC24 was larger than during the maximum phase of the same solar cycle.

IP shocks are faster during solar maxima than during solar minima (*Echer et al.*, 2003; *Oh et al.*, 2007; *Kilpua et al.*, 2015). However, the shock strength does not vary considerably from cycle to cycle (*Echer et al.*, 2003; *Kilpua et al.*, 2015). *Echer et al.* (2003) suggested that this effect may be related to the fact that, during solar minima, a decrease of the solar wind speed is compensated by an increase of the medium density. During solar maxima, as suggested by *Kilpua et al.* (2015), due to an increase of the Alfvén speed (see equation (9)), an increase of pressure pulse in the solar wind should be larger in order to steep into a shock.

Kilpua et al. (2015) reported that, for CME-driven shocks, the value of θ_{B_n}increased almost linearly with the shock occurrence. In the case of CIRs, these authors showed that the number of events of shocks with obliquity between 80° and 90° was slightly smaller than those driven by CMEs. Similar results were obtained by *Oliveira and Raeder* (2015) for all shocks regardless of the shock driver.

In respect to the shock impact angle, *Kilpua et al.* (2015) reported that CMEs tend to drive shocks with normals close to the X line, whereas CIRs tend to drive shocks with normals between the Sun-Earth line and the Parker spiral. For all drivers, *Oliveira and Raeder* (2015) showed that approximately 68% of the 450 FFSs studied by them had θ_{x_n} larger than 140°.

9.2. Effects on asymmetric magnetospheric response

Kaufmann and Konradi (1969) suggested that a highly inclined discontinuity may result in asymmetric magnetospheric response. Later, *Samsonov* (2011) solved the RH jump conditions for inclined IP shocks and obtained that the downstream solar wind V_y component increases with θ_{x_n}. The dynamic pressure in the Y direction also increases with the impact angle, and this may result in a significant asymmetric magnetopause deformation for very inclined shocks. *Samsonov* (2011) predicted that such asymmetrical compression makes a visible difference in magnetic field response which can be observed by ground magnetometers located in different local time regions.

In continuation to this work, *Samsonov et al.* (2015) reported results of global MHD simulations on the impact of an inclined IP shock. In their simulation, the shock struck the magnetosphere on the duskside. The duskside magnetopause was highly compressed immediately after the impact, but the dawnside magnetopause suffered an expansion before the compression. This numerical result is the first evident confirmation of previous suggestions (e.g., *Kaufmann and Konradi* (1969)) that a magnetospheric disturbance related to a pressure pulse impact will propagate faster in the magnetosphere than in the magnetosheath, therefore the magnetopause will expand before being compressed. *Samsonov et al.* (2015) predicted that ground magnetometers should register an overshoot before an SI^+ in the dawnside (opposite to a shock impact) region. Indeed, *Samsonov et al.* (2015) reported such overshoots not only occurred in the simulations, but in observations as well. These modeling and experimental asymmetric dawn-dusk responses confirmed predictions of *Kaufmann and Konradi* (1969) and *Samsonov* (2011).

Another simulation result reported by *Samsonov et al.* (2015) was a very large deformation of the magnetopause and cross-tail current in the magnetotail at $X = -30$ R_E. Such asymmetric responses occurred during and after the sweeping over of the magnetosphere by the inclined IP shock. They attributed this effect to a large V_y velocity component in the solar wind downstream of the inclined shock. An observation of deflection of the far magnetotail at $X = -240$ R_E of approximately 30° was reported by *Grygorov et al.* (2014) in agreement with *Samsonov et al.* (2015)'s results.

9.3. Effects on geomagnetic storm intensity

Jurac et al. (2002) showed that the shock geometry corresponds to an important parameter in forecasting shock geoeffectiveness. They explored the relationship between the θ_{B_n} angle in the intensity of geomagnetic storms followed by IP shock impacts within a time interval of 48 hours. In general, *Jurac et al.* (2002) reported that the Dst index decreased when θ_{B_n} increased. They showed that intense geomagnetic storms, that is, events with Dst $< -$ 100 nT, were more numerously preceeded by almost perpendicular shocks. Specifically, they found that in general almost perpendicular shocks were 2-4 times more likely to be followed by intense geomagnetic storms in comparison to oblique shocks. These observations confirmed theoretical predictions by *Grib et al.* (1979) and *Grib* (1982), who predicted that perpendicular shocks should be more geoeffective than oblique or parallel shocks because the downstrem IMF B_z component is generally more compressed ad consequentely intensified by almost perpendicular IP shocks.

9.4. Effects on geomagnetic sudden impulse rise time

Pioneer observations suggested that IP shocks are a direct cause of the Chapman-Ferraro current system compression directly related to sharp increases in the horizontal magnetic field, namely SI^+ events (*Chao and Lepping*, 1974; *Smith et al.*, 1986). The SI^+ rise time, defined as the difference between the horizontal magnetic field at the SI^+ onset and at the maximum SI^+ amplitude, was reported by early works to have typical values of 4 minutes (*Maeda et al.*, 1962; *Ondoh*, 1963). Despite several explanations of models for SI^+ rise times suggested in the past (see, e.g. *Nishida*, 1964), no association between shock inclination and SI^+ rise times were addressed.

The first association between shock inclination and SI^+ rise time was reported by *Takeuchi et al.* (2002). These authors explained that the unusually large SI^+ rise time

recorded by ground magnetometer stations, corresponding to ∼30 minutes, was caused by the impact of an IP shock that should have had a shock normal highly inclined with respect to the X-line in the equatorial plane. They attributed that unusual long SI^+ rise time to a gradual and asymmetric compression of the magnetosphere associated with the shock inclination. This result was confirmed latter by experimental data (*Wang et al.*, 2006; *Selvakumaran et al.*, 2017) and modeling efforts as well (*Wang et al.*, 2005; *Guo et al.*, 2005; *Selvakumaran et al.*, 2017).

Another important field of Space Weather investigations corresponds to the understanding of the geomagnetic field at geosynchronous orbit, since field variations directly affect satellites orbiting Earth in that region (see, e.g., *Horne et al.*, 2013). This magnetic field may also be subjected to asymmetric response caused by impact of IP shocks with different orientations. *Wang et al.* (2005) showed with PPMLR-MHD numerical simulations that the largest changes in the magnetic field there occurred close to the local time of the first contact between the IP shock and the bow shock. In the case of the frontal shock, the occurrence of maximum magnetic field took place at noon. On the other hand, in the case of the inclined shock impact, the maximum magnetic field intensification at geosyncrounous orbit occurred at 14 hours local time because the shock hit the magnetosphere in the afternoon section.

9.5. Effects on ionospheric field-aligned currents, cross-polar cap potential, and auroral precipitation

Simulation results reported by *Guo et al.* (2005) showed that the θ_{x_n} angle in the equatorial plane plays a major role in the magnetosphere-ionosphere response followed by the shock impact. These authors used the PPMLR-MHD code to show that a frontal and an inclined shock with similar downstream dynamic pressures led the MI system to very similar final steady states, but the steady state resulting from the inclined shock impact took longer to take place. *Guo et al.* (2005) attributed this effect to the asymmetric and longer compression of the magnetosphere caused by the inclined shock impact. These results supported the *Takeuchi et al.* (2002) observation and were later confirmed by the statistical study of *Wang et al.* (2006).

Simulations of the impacts of inclined and frontal shocks conducted by *Oliveira and Raeder* (2014) showed that transient shock compressions may trigger different geomagnetic activity. These authors showed that a moderate perpendicular head-on shock may be more geoeffective than a strong inclined oblique shock. *Oliveira and Raeder* (2014) attributed this effect mainly to the shock geometry in relation to the shock impact angle θ_{x_n} and the shock obliquity θ_{B_n}, in accordance with previous experimental and modeling results (*Jurac et al.*, 2002; *Takeuchi et al.*, 2002; *Guo et al.*, 2005; *Wang et al.*, 2006). In the frontal perpendicular case, the triggering of auroral substorm and possible excitation of cavity modes were primarily due to a symmetric plasmasheet compression, and the occurrence of the lowest (more negative) downstream V_x and B_z components.

Oliveira and Raeder (2014) showed that the frontal and perpendicular shocks excited ULF waves with well-defined frequencies, while the inclined and oblique shocks, even the strongest one, excited waves with non-defined trends. The frontal shock triggered auroral substorms in the Northern Hemisphere magnetic latitude regions between 65° and 70°, a well-known substorm signature (*Akasofu*, 1964; *McPherron*, 1991; *Tsurutani*, 2001). This response was not obtained in the runs with either the weak or strong inclined shocks. Ionospheric effects were also reported to be dependent upon the shock impact angle. CPCP and auroral precipitation showed higher response levels in the case of the frontal and perpendicular shock impact. The impact of the inclined and oblique shocks led to much smaller responses, even the strong inclined shock. *Oliveira and Raeder* (2014) suggested that the θ_{B_n} and θ_{x_n} angles may play a stronger role than the shock strength in the triggering of geomagnetic activity by shock impacts.

9.6. Effects on auroral substorm activity and nightside auroral power intensity

Early works such as *Kokubun et al.* (1977) showed that substorm activity is highly correlated with the occurrence of SI^+ events (*Akasofu and Chao*, 1980; *Craven et al.*, 1986). Later on, the triggering of substorm was associated with IP shock impacts (*Lui et al.*, 1990; *Zhou and Tsurutani*, 1999, 2001). Effects of precondition, i.e., intensity and duration of southward IMF B_z before shock impact, were showed to directly affect the intensity of magnetospheric substorms (*Zhou and Tsurutani*, 1999, 2001; *Yue et al.*, 2010; *Echer et al.*, 2011; *Liu et al.*, 2013).

The first attention to the shock impact angle as a contolling factor of substorm intensity was later given by *Oliveira and Raeder* (2015). Inspired by the simulation results of *Oliveira and Raeder* (2014), they used a data base with 451 FFSs to associate shock impact angles with substorm activity. *Oliveira and Raeder* (2015) used the SuperMAG SML index to measure substorm intensity because this index offers a larger spatial coverage as opposed to the traditional IAGA index, in this case the AL index. *Oliveira and Raeder* (2015) carefully grouped the shocks in categories related to the shock strength and how inclined the shock normals were in relation the X line. They found that, in general, the higher the shock speed, that is, the stronger the shock, and the more frontal the shock, the higher the substorm activity followed by the shock impacts as measured by variations in the SML index.

Similar conclusions were obtained by *Oliveira et al.* (2016), who studied auroral power intensifications followed by impacts of IP shocks with different angles of impact. The AP intensifications were computed with the SuperMAG SME index as determined by *Newell and Gjerloev* (2011b). Again, the stronger and the frontal the shock,

the higher the auroral power dissipated in the nightside ionosphere.

As in the *Oliveira and Raeder* (2014) work, *Oliveira and Raeder* (2015) attributed the higher substorm activity followed by the impact of head-on shocks to a favorable mechanism of release of electromagnetic energy previously loaded in the magnetotail. As a result, all these works (*Oliveira and Raeder*, 2014, 2015; *Oliveira et al.*, 2016; *Oliveira*, 2017) suggest that the shock impact angle, in addition to preconditioning effects, has a significant importance in forecasting Space Weather events triggered by IP shocks impacts with different orientations.

Appendix A. List of acronyms and abbreviations

ACE	Advanced Composition Explorer
AE	Auroral Electroject
AL	Amplitude Lower
AU	Amplitude Upper (geomagnetic index)
AU	Astronomical Unit (distance unit)
AP	Auroral Power
BATS-R-US	Block Adaptive-Tree Solar wind Roe-type Upwind Scheme
CCMC	Coordinated Community Modeling Center
CDAWeb	Coordinated Data Analysis Web
CIR	Corotating Interaction Region
CME	Coronal Mass Ejection
CPCP	Dross Polar Cap Potential
CTIM	Coupled Thermosphere Ionosphere Model
DAPEF	Diffusive Auroral Precipitation Energy Flux
Dst	Disturbance Storm Time
EEJ	Equatorial Electroject
FAC	Field-Aligned Current
FFS	Fast Forward Shock
FRS	Fast Reverse Shock
FPS	Frontal Perpendicular Shock
FV-TVD	Finite Volume Total Variation Diminishing
GSE	Geocentric Solar Ecliptic
GIC	Geomagnetically Induced Current
GUMICS	Grand Unified Magnetosphere Ionosphere Coupling Simulation
IAGA	International Association of Geomagnetism and Aeronomy
IGY	International Geophysical Year
IOS	Inclined Oblique Shock
IP	Interplanetary
LFM	Lyon Fedder Mobarry
MC	Magnetic Coplanarity
MFI	Magnetic Fields Investigation
MLAT	Magnetic Latitude
MPI	Method Parsing Interface
MHD	Magnetohydrodynamic
MD(1,2,3)	Mixed Data Method (1,2,3)
NASA	National Aeronautics and Space Administration
NBZ	Northward B_z currents
NOAA	National Oceanic and Atmospheric Administration
$\mathbf{R}_E$	Earth's radius (6371 km)
RH	Rankine-Hugoniot
RL	Radio Loud
RQ	Radio Quiet
OpenGGCM	Open General Global Circulation Model
PMS	Planar Magnetic Structure
PPMLR	Piecewise Parabolic Method with a Lagrangian Remap
SC	Solar Cycle
SFS	Slow Forward Shock
$\mathbf{SI^+/SI^-}$	Positive/Negative Sudden Impulse
SIDC	Solar Influence Data Analysis Center
SRS	Slow Reverse Shock
SSC	Storm Sudden Commencement
SML	SuperMAG Lower
SME	SuperMAG Electroject
SMU	SuperMAG Upper
SSN	Sunspot Number
STEREO	Solar Terrestrial Relations Observatory
SWEPAM	Solar Wind Electron, Proton and Alpha Monitor
SWMF	Space Weather Modeling Framework
SYM-H	Symmetric ring current index
ULF	Ultra Low Frequency
UVI	Ultraviolet
VC	Velocity Coplanarity

Acknowledgments

I would like to thank the following agencies for sponsoring this work, partially and thoroughly, through grants NNX13AK31G and NNH13ZDA001N-HSR, by NASA, grant AGS-1143895, by NSF, and grant FA-9550-120264, by AFOSR. I also acknowledge the Wind and ACE teams for providing their data through NASA's CDAWeb interface. The author acknowledges the SuperMAG PI Dr. Jesper W. Gjerloev the whole SuperMAG team for data availability and the website convenience for data download.

References

Abraham-Shrauner, B. (1972), Determination of magnetohydronamic shock normals, *J. Geophys. Res.*, *77*(4), 736–739, doi:10.1029/JA077i004p00736.

Abraham-Shrauner, B., and S. H. Yun (1976), Interplanetary shocks seen by Ames Plasma Probe on Pioneer 6 and 7, *J. Geophys. Res.*, *81*(13), doi:10.1029/JA081i013p02097.

Acuña, M. H., D. C. L. Scheifele, C. T. Russell, P. Schroeder, A. Szabo, and J. G. Luhmann (2008), The STEREO/IMPACT magnetic field experiment, *Space Sci. Rev.*, *136*(1), 203–226, doi:10.1007/s11214-007-9259-2.

Adhikari, L., G. P. Zank, P. Hunana, and Q. Hu (2016), The interaction of turbulence with parallel and perpendicular shocks, *Journal of Physics: Conference Series*, *767*(1), 1–13, doi:10.1088/1742-6596/767/1/012001.

Akasofu, S.-I. (1964), The development of the auroral substorm, *Planet. Space Sci.*, *12*(4), 273–282, doi:10.1016/0032-0633(64)90151-5.

Akasofu, S.-I. (1979), Interplanetary energy flux associated with magnetospheric substorms, *Planet. Space Sci.*, *27*(4), 425–431, doi:10.1016/0032-0633(79)90119-3.

Akasofu, S.-I., and J. Chao (1980), Interplanetary shock waves and magnetospheric substorms, *Planet. Space Sci.*, *28*(4), 381–385, doi:10.1016/0032-0633(80)90042-2.

Akhiezer, A., G. Lubarski, and R. Polovin (1959), The stability of shock waves in magnetohydrodynamics, *Soviet Phys. JETP*, *8*, 507–511.

Allen, J., H. Sauer, L. Frank, and P. Reiff (1989), Effects of the March 1989 solar activity, *Eos Trans. AGU*, *70*(46), 1479–1488, doi:10.1029/89EO00409.

Anderson, D., A. Anghel, K. Yumoto, M. Ishitsuka, and E. Kudeki (2002), Estimating daytime vertical **E**×**B** drift velocities in the equatorial F-region using ground-based magnetometer observations, *Geophys. Res. Lett.*, *29*(12), 37–1–37–4, doi:10.1029/2001GL014562.

Andréeová, K., and L. Přech (2007), Propagation of interplanetary shocks into the Earth's magnetosphere, *Adv. Space Res.*, *40*(12), 1871–1880, doi:10.1016/j.asr.2007.04.079.

Andréeová, K., T. I. Pulkkinen, T. V. Laitinen, and L. Přech (2008), Shock propagation in the magnetosphere: Observations and MHD simulations compared, *J. Geophys. Res.*, *113*(A09224), doi:10.1029/2008JA013350.

Araki, T. (1977), Global structure of geomagnetic sudden commencements, *Planet. Space Sci.*, *25*(4), 373–384, doi:10.1016/0032-0633(77)90053-8.

Araki, T. (1994), A physical model of the geomagnetic sudden commencement, in *Solar Wind Sources of Magnetospheric Ultra-Low-Frequency Waves*, edited by M. J. Engebretson, K. Takahashi, and M. Scholer, pp. 183–200, American Geophysical Union, Washington, D.C., doi:10.1029/GM081p0183.

Araki, T., T. Takeuchi, and Y. Araki (2004), Rise time of geomagnetic sudden commencements statistical analysis of ground geomagnetic data, *Earth, Planets and Space*, *56*(2), 289–293, doi:10.1186/BF03353411.

Axford, W. I. (1962), The interaction between the solar wind and the earth's magnetosphere, *J. Geophys. Res.*, *67*(10), 3791–3796, doi:10.1029/JZ067i010p03791.

Banach, J. (1987), *Pipeline coatings - Evaluation, repair, and impact on corrosion protection design and cost*, chap. 29, p. 10, National Assoc. of Corrosion Engineers, Houston, TX.

Bartels, J. (1949), The standardized index, Ks, and the planetary index, Kp, *Int. Union Geod. Geophys. IATME Bull.*, *97*(12b).

Berdichevsky, D. B., A. Szabo, R. P. Lepping, A. F. Viñas, and F. Mariani (2000), Interplanetary fast shocks and associated drivers observed through the 23rd solar minimum by Wind over its first 2.5 years, *J. Geophys. Res.*, *105*(A12), 27,289 27,314, doi:10.1029/1999JA000367.

Blake, J. B., W. A. Kolasinski, R. W. Fillius, and E. G. Mullen (1992), Injection of electrons and protons with energies of tens of MeV into L < 3 on 24 March 1991, *Geophys. Res. Lett.*, *19*(8), 821–824, doi:10.1029/92GL00624.

Bolduc, L. (2002), GIC observations and studies in the Hydro-Québec power system, *J. Atmos. Sol. Terr. Phys.*, *64*(16), 1793–1802, doi:10.1016/S1364-6826(02)00128-1.

Boteler, D., R. Pirjola, and H. Nevanlinna (1998), The effects of geomagnetic disturbances on electrical systems at the Earth's surface, *Adv. Space Res.*, *22*(1), 17–27, doi:10.1016/S0273-1177(97)01096-X.

Burgess, D., E. A. Lucek, M. Scholer, S. D. Bale, M. A. Balikhin, A. Balogh, T. S. Horbury, V. V. K. H. Kucharek, B. Lembège, E. Möbius, S. J. Schwartz, M. F. Thomsen, and S. N. Walker (2005), Quasi-parallel shock structure and processes, in *Outer Magnetospheric Boundaries: Cluster Results*, edited by G. Paschmann, S. Schwartz, C. P. Escoubet, and S. Haaland, pp. 205–222, Springer Netherlands, Dordrecht, The Netherlands, doi:10.1007/1-4020-4582-4_7.

Burlaga, L., R. Lepping, R. Weber, T. Armstrong, C. Goodrich, J. Sullivan, D. Gurnett, P. Kellogg, E. Keppler, F. Mariani, F. Neubauer, H. Rosenbauer, and R. Schwenn (1980), Interplanetary particles and fields, November 22 to December 6, 1977: Helios, Voyager, and IMP observations between 0.6 and 1.6 au, *J. Geophys. Res.*, *85*(A5), 2227–2242, doi:10.1029/JA085iA05p02227.

Burlaga, L. F. (1971), Hydromagnetic waves and discontinuities in the solar wind, *Space Sci. Rev.*, *12*(5), 600–657, doi:10.1007/BF00173345.

Burlaga, L. F., and J. K. Chao (1971), Reverse and forward slow shocks in the solar wind, *J. Geophys. Res.*, *76*(31), 7516–7521, doi:10.1029/JA076i031p07516.

Cahill, L. J., and P. Amazeen (1963), The boundary of the geomagnetic field., *J. Geophys. Res.*, *68*(7), 1835–1843, doi:10.1029/JZ068i007p01835.

Carovillano, R. L., and G. L. Siscoe (1973), Energy and momentum theorems in magnetospheric processes, *Rev. Geophys.*, *11*(2), 289–353, doi:10.1029/RG011i002p00289.

Carter, B. A., E. Yizengaw, R. Pradipta, A. J. Halford, R. Norman, and K. Zhang (2015), Interplanetary shocks and the resulting geomagnetically induced currents at the equator, *Geophys. Res. Lett.*, *42*(16), 6554–6559, doi:10.1002/2015GL065060.

Chao, J. K., and R. P. Lepping (1974), A correlative study of SSC's, interplanetary shocks, and solar activity, *J. Geophys. Res.*, *79*(13), 1799–1807, doi:10.1029/JA079i013p01799.

Chao, J. K., and S. Olbert (1970), Observation of slow shocks in interplanetary space, *J. Geophys. Res.*, *75*(31), 6394–6397, doi:10.1029/JA075i031p06394.

Chao, J. K., L. H. Lyu, B. H. Wu, A. J. Lazarus, T. S. Chang, and R. P. Lepping (1993), Observations of an intermediate shock in interplanetary space, *J. Geophys. Res.*, *98*(A10), 17,443–17,450, doi:10.1029/93JA01609.

Claudepierre, S. G., M. K. Hudson, W. Lotko, J. G. Lyon, and R. E. Denton (2010), Solar wind driving of magnetospheric ULF waves: Field line resonances driven by dynamic pressure fluctuations, *J. Geophys. Res.*, *115*(A11), doi:10.1029/2010JA015399.

Colburn, D. S., and C. P. Sonett (1966), Discontinuities in the solar wind, *Space Sci. Rev.*, *439*(A11), 506, doi:10.1007/BF00240575.

Connor, H. K., E. Zesta, M. Fedrizzi, Y. Shi, J. Raeder, M. V. Codrescu, and T. J. Fuller-Rowell (2016), Modeling the ionosphere-thermosphere response to a geomagnetic storm using physics-based magnetospheric energy input: OpenGGCM-CTIM results, *J. Space Weather Space Clim.*, *6*(A25), 1–15, doi:10.1051/swsc/2016019.

Cowley, S. W. H. (2000), Magnetosphere-ionosphere Interactions: A Tutorial Review, in *Magnetospheric Current Systems*, edited by S. Ohtani, R. Fujii, M. Hesse, and R. L. Lysak, Geophys. Monogr. Ser. 118, pp. 91–106, American Geophysical Union, Washington, D.C., doi:10.1029/GM118p0091.

Craven, J. D., L. A. Frank, C. T. Russell, E. E. Smith, and R. P. Lepping (1986), Global auroral responses to magnetospheric compressions by shocks in the solar wind: Two case studies, in *Solar Wind-Magnetosphere Coupling*, edited by Y. Kamide and J. A. Slavin, pp. 367–380, Terra Scientific, Tokyo, Japan.

Daglis, I. A., R. M. Thorne, W. Baumjohann, and S. Orsini (1999), The terrestrial ring current: Origin, formation, and decay, *Rev. Geophys.*, *37*(4), 407–438, doi:10.1029/1999RG900009.

Davis, T. N., and M. Sugiura (1966), Auroral electrojet activity index AE and its universal time variations, *J. Geophys. Res.*, *71*(3), 785–801, doi:10.1029/JZ071i003p00785.

De Sterck, H., and S. Poedts (2000), Intermediate shocks in three-dimensional magnetohydrodynamic bow-shock flows with multiple interacting shock fronts, *Phys. Rev. Lett.*, *84*, 5524–5527, doi:10.1103/PhysRevLett.84.5524.

Dessler, A. J., and E. N. Parker (1959), Hydromagnetic theory of geomagnetic storms, *J. Geophys. Res.*, *64*(12), 2239–2252,

doi:10.1029/JZ064i012p02239.
Dessler, A. J., W. E. Francis, and E. N. Parker (1960), Geomagnetic storm sudden-commencement rise times, *J. Geophys. Res.*, *65*(9), 2715–2719, doi:10.1029/JZ065i009p02715.
Dryer, M. (1973), Bow shock and its interaction with interplanetary shocks, *Radio Science*, *8*(11), 893–901, doi:10.1029/RS008i011p00893.
Dryer, M., D. L. Merritt, and P. M. Aronson (1967), Interaction of a plasma cloud with the earth's magnetosphere, *J. Geophys. Res.*, *72*(11), 2955–2962, doi:10.1029/JZ072i011p02955.
Eastwood, J. P., H. Hietala, G. Tóth, T. D. Phan, and M. Fujimoto (2014), What controls the structure and dynamics of Earth's magnetosphere?, *Space Sci. Rev.*, pp. 1–36, doi:10.1007/s11214-014-0050-x.
Echer, E., W. D. Gonzalez, L. E. A. Vieira, A. Dal Lago, F. L. Guarnieri, A. Prestes, A. L. C. Gonzalez, and N. J. Schuch (2003), Interplanetary shock parameters during solar activity maximum (2000) and minimum (1995-1996), *Braz. Jour. Phys.*, *33*(1), 2301, doi:10.1590/S0103-97332003000100010.
Echer, E., M. V. Alves, and W. D. Gonzalez (2004), Geoefectiveness of interplanetary shocks during solar minimum (1995) and solar maximum (2000), *Solar Phys.*, *221*, 361–380, doi:10.1023/B:SOLA.0000035045.65224.f3.
Echer, E., W. D. Gonzalez, and B. T. Tsurutani (2008a), Interplanetary conditions leading to superintense geomagnetic storms (Dst < -250 nT) during solar cycle 23, *Geophys. Res. Lett.*, *35*(L06S03), doi:10.1029/2007GL031755.
Echer, E., W. D. Gonzalez, B. T. Tsurutani, and A. L. C. Gonzalez (2008b), Interplanetary conditions causing intense geomagnetic storms (Dst ≤ -100 nt) during solar cycle 23 (19962006), *J. Geophys. Res.*, *113*(A5), doi:10.1029/2007JA012744.
Echer, E., B. Tsurutani, F. Guarnieri, and J. Kozyra (2011), Interplanetary fast forward shocks and their geomagnetic effects: CAWSES events, *J. Atmos. Sol. Terr. Phys.*, *73*(11-12), 1330–1338, doi:10.1016/j.jastp.2010.09.020.
Eddy, J. A. (1976), The maunder minimum, *Science*, *192*(4245), 1189–1202, doi:10.1126/science.192.4245.1189.
Feng, H., and J. M. Wang (2008), Observations of a 2→3 type interplanetary intermediate shock, *Solar Phys.*, *247*(1), 195–201, doi:10.1007/s11207-007-9087-2.
Feng, H. Q., Q. H. Li, J. M. Wang, and G. Q. Zhao (2016), Observations of an interplanetary intermediate shock associated with a magnetic reconnection exhaust, *The Astrophysical Journal*, *826*(1), 1–5, doi:10.3847/0004-637X/826/1/15.
Fermi, E. (1949), On the origin of the cosmic radiation, *Phys. Rev.*, *75*, 1169–1174, doi:10.1103/PhysRev.75.1169.
Forbes, J. M. (1981), The equatorial electrojet, *Rev. Geophys.*, *19*(3), 469–504, doi:10.1029/RG019i003p00469.
Fowler, G. J. (2005), The compression of the geo-magnetosphere: A physical model and the effects of compression, Ph.D. dissertation, University of California, Los Angeles.
Fujita, S., T. Tanaka, T. Kikuchi, K. Fujimoto, K. Hosokawa, and M. Itonaga (2003a), A numerical simulation of the geomagnetic sudden commencement: 1. Generation of the field-aligned current associated with the preliminary impulse, *J. Geophys. Res.*, *108*(A12), doi:10.1029/2002JA009407.
Fujita, S., T. Tanaka, T. Kikuchi, K. Fujimoto, and M. Itonaga (2003b), A numerical simulation of the geomagnetic sudden commencement: 2. Plasma processes in the main impulse, *J. Geophys. Res.*, *108*(A12), doi:10.1029/2002JA009763.
Fuller-Rowell, T. J., D. Rees, S. Quegan, R. J. Moffet, M. V. Codrescu, and G. H. Millward (1996), A coupled thermosphere-ionosphere model (CTIM), in *STEP Report*, edited by R. W. Schunk, p. 217, Scientific Committee on Solar Terrestrial Physics (SCOSTEP), NOAA/NGDC, Boulder, Colorado.
Galvin, A. B., L. M. Kistler, M. A. Popecki, C. J. Farrugia, K. D. C. Simunac, L. Ellis, E. Möbius, M. A. Lee, M. Boehm, J. Carroll, A. Crawshaw, M. Conti, P. Demaine, S. Ellis, J. A. Gaidos, J. Googins, M. Granoff, A. Gustafson, D. Heirtzler, B. King, U. Knauss, J. Levasseur, S. Longworth, K. Singer, S. Turco, P. Vachon, M. Vosbury, M. Widholm, L. M. Blush, R. Karrer, P. Bochsler, H. Daoudi, A. Etter, J. Fischer, J. J. Opitz, M. Sigrist, P. Wurz, B. Klecker, M. E. E. Seidenschwang, R. F. Wimmer-Schweingruber, M. Koeten, B. Thompson, and D. Steinfeld (2008), The Plasma and Suprathermal Ion Composition (PLASTIC) investigation on the STEREO Observatories, *Space Sci. Rev.*, *136*(1), 437–486, doi:10.1007/s11214-007-9296-x.
Gideon, D. N., A. T. Hopper, and R. E. Thompson (1970), *Earth current effects on buried pipelines: Analysis of observations of telluric gradients and their effects*, American Gas Association, Washington, D.C.
Gillmor, C. S., and J. R. Spreiter (Eds.) (1997), *Discovery of the Magnetosphere*, *History of Geophysics*, vol. 7, American Geophysical Union, Washington, D.C., doi:10.1029/HG007.
Gjerloev, J. W. (2009), A global ground-based magnetometer initiative, *Eos Trans. AGU*, *90*(27), 230–231, doi:10.1029/2009EO270002.
Gjerloev, J. W. (2012), The SuperMAG data processing technique, *J. Geophys. Res.*, *117*(A09213), 1–19, doi:10.1029/2012JA017683.
Gold, T. (1955), Discussion on shock waves and rarefied gases, in *Gas Dynamics of Cosmic Clouds*, North Holland Publ. Co., Amsterdan, the Netherlands.
Goncharov, O., J. Šafránková, and Z. Němeček (2015), Interplanetary shockbow shock interaction: Comparison of a global mhd model and observation, *Planet. Space Sci.*, *2015*, 4–11, doi:10.1016/j.pss.2014.12.001.
Gonzalez, W. D., and B. T. Tsurutani (1987), Criteria of interplanetary parameters causing intense magnetic storms (Dst < -100 nT), *Planet. Space Sci.*, *35*(9), 1101–1109, doi:10.1016/0032-0633(87)90015-8.
Gonzalez, W. D., A. L. Cla de Gonzalez, O. Mendes, and B. T. Tsurutani (1992), Difficulties defining storm sudden commencements, *Eos Trans. AGU*, *73*(16), 180–181, doi:10.1029/91EO00148.
Gonzalez, W. D., J. A. Joselyn, Y. Kamide, H. W. Kroehl, G. Rostoker, B. T. Tsurutani, and V. M. Vasyliūnas (1994), What is a geomagnetic storm?, *J. Geophys. Res.*, *99*(A4), 5771–5792, doi:10.1029/93JA02867.
Gonzalez, W. D., B. T. Tsurutani, and A. L. Clúa de Gonzalez (1999), Interplanetary origin of geomagnetic storms, *Space Sci. Rev.*, *88*(3-4), 529–562, doi:10.1023/A:1005160129098.
Gonzalez, W. D., E. Echer, A. L. C. B. T., and Tsurutani (2007), Interplanetary origin of intense geomagnetic storms (Dst < -100 nT) during solar cycle 23, *Geophys. Res. Lett.*, *34*(6), doi:10.1029/2006GL028879.
Gopalswamy, N., H. Xie, P. Mäkelä, S. Akiyama, S. Yashiro, M. L. Kaiser, R. A. Howard, and J.-L. Bougeret (2010), Interplanetary shocks lacking type II radio bursts, *The Astrophysical Journal*, *710*(2), 1111–1126, doi:10.1088/0004-637X/710/2/1111.
Gosling, J. T. (1997), Coronal mass ejections: An overview, in *Coronal Mass Ejections*, edited by N. Crooker, J. A. Jocelyn, and J. Feynman, Geophys. Monogr. Ser. 99, pp. 9–16, American Geophysical Union, Washington, DC, Washington, D.C., doi:10.1029/GM099p0009.
Gosling, J. T., D. J. McComas, J. L. Phillips, L. A. Weiss, V. J. Pizzo, B. E. Goldstein, and R. J. Forsyth (1994), A new class of forward-reverse shock pairs in the solar wind, *Geophys. Res. Lett.*, *21*(21), 2271–2274, doi:10.1029/94GL02245.
Grib, S., B. Brunelli, M. Dryer, and W.-W. Shen (1979), Interaction of interplanetary shock waves with the bow shock-magnetopause system, *J. Geophys. Res.*, *84*(A10), 5907–5921, doi:10.1029/JA084iA10p05907.
Grib, S. A. (1982), Interaction of non-perpendicular/parallel solar wind waves with the Earth's magnetosphere, *Space Sci. Rev.*, *32*, 43–48, doi:10.1007/BF00225175.
Grib, S. A., and E. A. Pushkar (2006), Asymetry of nonlinear interactions of solar MHD discontinuities with the bow shock, *Geomagnetism and Aeronomy*, *46*(4), 417–423, doi:doi:10.1134/S0016793206040025.
Grygorov, K., L. Přech, J. Šafránková, Z. Němeček, and O. Goncharov (2014), The far magnetotail response to an interplanetary shock arrival, *Planet. Space Sci.*, doi:10.1016/j.pss.2014.07.016.
Gummow, R. A., and P. Eng (2002), GIC effects on pipeline corrosion

and corrosion control systems, *J. Atmos. Sol. Terr. Phys.*, *64*(16), 1755–1764, doi:10.1016/S1364-6826(02)00125-6.

Guo, X.-C., and Y.-Q. Hu (2007), Response of Earth's ionosphere to interplanetary shocks, *Chinese J. Geophys*, *50*(4), 817–823, doi:10.1002/cjg2.1099.

Guo, X.-C., Y.-Q. Hu, and C. Wang (2005), Earth's magnetosphere impinged by interplanetary shocks of different orientations, *Chinese Phys. Lett.*, *22*(12), 3221–3224, doi:10.1088/0256-307X/22/12/067.

Gurnett, D. A., and A. Bhattacharjee (2005), *Introduction to Plasma Physics With Space and Laboratory Applications*, Cambridge University Press, Cambridge, United Kingdom.

Hada, T. (1994), Evolutionary conditions in the dissipative MHD system: Stability of intermediate MHD shock waves, *Geophys. Res. Lett.*, *21*(21), 2275–2278, doi:10.1029/94GL02239.

Halford, A. J., S. L. McGregor, K. R. Murphy, R. M. Millan, M. K. Hudson, L. A. Woodger, C. A. Cattel, A. W. Breneman, I. R. Mann, W. S. Kurth, G. B. Hospodarsky, M. Gkioulidou, and J. F. Fennell (2015), BARREL observations of an ICME-shock impact with the magnetosphere and the resultant radiation belt electron loss, *J. Geophys. Res. Space Physics*, *120*(4), 2557–2570, doi:10.1002/2014JA020873.

Hapgood, M., and A. Thomson (2010), *Space Weather: its impact on Earth and implications for business*, Lloyd's 360 Risk Insight, London, U.K.

Heppner, J. P. (1955), Note on the occurrence of world-wide S.S.C.'s during the onset of negative bays at College, Alaska, *J. Geophys. Res.*, *60*(1), 29–31, doi:10.1029/JZ060i001p00029.

Heppner, J. P., N. F. Ness, C. S. Scearce, and T. L. Skillman (1963), Explorer 10 magnetic field measurements, *J. Geophys. Res.*, *68*(1), 1–46, doi:10.1029/JZ068i001p00001.

Hoffman, R. A., L. J. Cahill, R. R. Anderson, N. C. Maynard, P. H. Smith, T. A. Fritz, D. J. Williams, A. Konradi, and D. A. Gurnett (1975), Explorer 45 (S^3-A) observations of the magnetosphere and magnetopause during the August 4-6, 1972, magnetic storm period, *J. Geophys. Res.*, *80*(31), 4287–4296, doi:10.1029/JA080i031p04287.

Horne, R. B., S. A. Glauert, N. P. Meredith, D. Boscher, V. Maget, D. Heynderickx, and D. Pitchford (2013), Space weather impacts on satellites and forecasting the earth's electron radiation belts with SPACECAST, *Space Weather*, *11*(4), 169–186, doi:10.1002/swe.20023.

Hsieh, W.-C., J.-H. Shue, J.-K. Chao, T.-C. Tsai, Z. Němeček, and J. Šafránková (2014), Possible observational evidence of contact discontinuities, *Geophys. Res. Lett.*, *41*(22), doi:10.1002/2014GL062342.

Hu, Y.-Q., X.-C. Guo, G.-Q. Li, C. Wang, and Z.-H. Huang (2005), Oscillation of quasi-steady Earth's magnetosphere, *Chinese Phys. Lett.*, *22*(10), 2723–2726, doi:10.1088/0256-307X/22/10/073.

Hudson, M. K., S. R. Elkington, J. G. Lyon, V. A. Marchenko, I. Roth, M. Temerin, J. B. Blake, M. S. Gussenhoven, and J. R. Wygant (1997), Simulations of radiation belt formation during storm sudden commencements, *J. Geophys. Res.*, *102*(A7), 14,087–14,102, doi:10.1029/97JA03995.

Hudson, P. D. (1970), Discontinuities in an anisotropic plasma and their identification in the solar wind, *Planet. Space Sci.*, *18*(11), 1611–1622, doi:10.1016/0032-0633(70)90036-X.

Hughes, W. J. (1994), Magnetospheric ULF waves: A tutorial with a historical perspective, in *Solar Wind Sources of Magnetospheric Ultra-Low-Frequency Waves*, edited by M. J. Engebretson, K. Takahashi, and M. Scholer, Geophys. Monogr. Ser. 81, p. 1, American Geophysical Union, Washington D.C., doi:10.1029/GM081p0001.

Hundhausen, A. J., and R. A. Gentry (1969), Numerical simulation of flare-generated disturbances in the solar wind, *J. Geophys. Res.*, *74*(11), 2908–2918, doi:10.1029/JA074i011p02908.

Huttunen, K. E. J., H. E. J. Koskinen, and R. Schwenn (2002), Variability of magnetospheric storms driven by different solar wind perturbations, *J. Geophys. Res.*, *107*(A7), SMP 20–1–SMP 20–8, doi:10.1029/2001JA900171.

Huttunen, K. E. J., J. Slavin, M. Collier, H. E. J. Koskinen, A. Szabo, E. Tanskanen, A. Balogh, E. Lucek, and H. Rème (2005), Cluster observations of sudden impulses in the magnetotail caused by interplanetary shocks and pressure increases, *Ann. Geophys.*, *23*(2), 609–624, doi:10.5194/angeo-23-609-2005.

Ivanov, K. G. (1964), Interaction of running shock waves with strong discontinuities in the space vicinity of the Earth, *Geomagn. Aeron.*, *4*, 803–806.

Iyemori, T. (1990), Storm-time magnetospheric currents inferred from mid–latitude geomagnetic field variations, *J. Geomagn. Geoelectr.*, *42*(11), 1249–1265, doi:10.5636/jgg.42.1249.

Janhunen, P., M. Palmroth, T. Laitinen, I. Honkonen, L. Juusola, G. Facskó, and T. Pulkkinen (2012), The GUMICS-4 global MHD magnetosphereionosphere coupling simulation, *J. Atmos. Sol. Terr. Phys.*, *80*, 48–59, doi:10.1016/j.jastp.2012.03.006.

Janhunsen, P. (1996), GUMICS-3: A global ionosphere-magnetosphere coupling simulation with high ionospheric resolution, in *Environment Modeling for Space-Based Applications, Symposium Proceedings (ESA SP-392)*, edited by T.-D.Guyenne and A. Hilgers, pp. 233–239, ESA/TSTEC, Noordwijk, The Netherlands.

Jeffrey, A., and T. Taniuti (1964), *Nonlinear Wave Propagation*, Academic Press, New York.

Jian, L., C. Russell, J. Luhmann, and R. Skoug (2006a), Properties of stream interactions at one AU during 1995-2004, *Solar Phys.*, *239*(1-2), 337–392, doi:10.1007/s11207-006-0132-3.

Jian, L., C. Russell, J. Luhmann, and R. Skoug (2006b), Properties of interplanetary coronal mass ejections at one AU during 1995-2004, *Solar Phys.*, *239*(1-2), 393–436, doi:10.1007/s11207-006-0133-2.

Joselyn, J. A., and B. T. Tsurutani (1990), Geomagnetic Sudden impulses and storm sudden commencements: A note on terminology, *Eos Trans. AGU*, *71*(47), 1808–1809, doi:10.1029/90EO00350.

Jurac, S., J. C. Kasper, J. D. Richardson, and A. J. Lazarus (2002), Geomagnetic disturbances and their relationship to interplanetary shock parameters, *Geophys. Res. Lett.*, *29*(10), doi:10.1029/2001GL014034.

Kamide, Y. (2005), What determines the intensity of magnetospheric substorms?, in *Multiscale Coupling of Sun-Earth Processes*, edited by A. Lui, Y. Kamide, and G. Consolini, pp. 175–194, Elsevier Science B.V., Amsterdam, doi:10.1016/B978-044451881-1/50014-9.

Kamide, Y., and J. A. Slavin (Eds.) (1986), *Solar Wind - Magnetosphere Coupling*, vol. 126, Springer.

Kamide, Y., B.-H. Ahn, S.-I. Akasofu, W. Baumjohann, E. Friis-Christensen, H. W. Kroehl, H. Maurer, A. D. Richmond, G. Rostoker, R. W. Spiro, J. K. Walker, and A. N. Zaitzev (1982), Global distribution of ionospheric and field–aligned currents during substorms as determined from six IMS meridian chains of magnetometers: Initial results, *J. Geophys. Res.*, *87*(A10), 8228–8240, doi:10.1029/JA087iA10p08228.

Kan, J. R., and L. C. Lee (1979), Energy coupling function and solar wind–magnetosphere dynamo, *Geophys. Res. Lett.*, *6*(7), 577–580, doi:10.1029/GL006i007p00577.

Kantrowitz, A., and H. E. Petschek (1966), MHD characteristics and shock waves, in *Plasma physics in theory and application*, edited by W. B. Kunkel, pp. 148–207, McGraw-Hill, New York.

Kappenman, J. (2010), Geomagnetic storms and their impacts on the US power grid, *Tech. rep.*, Metatech Corp., Goleta, California.

Kataoka, R., S. Watari, N. Shimada, H. Shimazu, and K. Marubashi (2005), Downstream structures of interplanetary fast shocks associated with coronal mass ejections, *Geophys. Res. Lett.*, *32*(12), doi:10.1029/2005GL022777.

Kaufmann, R. L., and A. Konradi (1969), Explorer 12 magnetopause observations: Large-scale nonuniform motion, *J. Geophys. Res.*, *74*(14), 3609–3627, doi:10.1029/JA074i014p03609.

Keika, K., R. Nakamura, W. Baumjohann, A. Runov, T. Takada, M. Volwerk, T. L. Zhang, B. Klecker, E. A. Lucek, C. Carr, H. Rme, I. Dandouras, M. André, and H. Frey (2008), Response of the inner magnetosphere and the plasma sheet to a sudden impulse, *J. Geophys. Res.*, *113*(A7), doi:10.1029/2007JA012763.

Keller, K. A., M. Hesse, L. Rastätter, M. M. Kuznetsova, T. Moretto, P. J. Reitan, T. I. Gombosi, D. L. D. Zeeuw, and B. V. Beq (2002),

Global MHD modeling of the impact of a solar wind pressure change, *J. Geophys. Res.*, *107*(A7), doi:10.1029/2001JA000060.

Kellogg, P. J. (1962), Flow of plasma around the Earth, *J. Geophys. Res.*, *67*, 3805–3811, doi:10.1029/JZ067i010p03805.

Kennel, C. F., F. L. Scarf, F. V. Coroniti, C. T. Russell, K.-P. Wenzel, T. R. Sanderson, P. Van Nes, W. C. Feldman, G. K. Parks, E. J. Smith, B. T. Tsurutani, F. S. Mozer, M. Temerin, R. R. Anderson, J. D. Scudder, and M. Scholer (1984a), Plasma and energetic particle structure upstream of a quasi–parallel interplanetary shock, *J. Geophys. Res.*, *89*(A7), 5419–5435, doi:10.1029/JA089iA07p05419.

Kennel, C. F., J. P. Edmiston, F. L. Scarf, F. V. Coroniti, C. T. Russell, E. J. Smith, B. T. Tsurutani, J. D. Scudder, W. C. Feldman, R. R. Anderson, F. S. Mozer, and M. Temerin (1984b), Structure of the November 12, 1978, quasi–parallel interplanetary shock, *J. Geophys. Res.*, *89*(A7), 5436–5452, doi:10.1029/JA089iA07p05436.

Kennel, C. F., J. P. Edmiston, and T. Hada (1985), A quarter century of collisionless shock research, in *Collisionless Shocks in the Heliosphere: A Tutorial Review*, edited by R. G. Stone and B. Tsurutani, Geophys. Monogr. Ser. 34, pp. 1–36, American Geophysical Union, Washington, D.C., doi:10.1029/GM034p0001.

Kennel, C. F., R. D. Blandford, and P. Coppi (1989), MHD intermediate shock discontinuities. Part 1. Rankine-Hugoniot conditions, *Journal of Plasma Physics*, *42*(2), 299–319, doi:10.1017/S0022377800014379.

Kilpua, E. K. J., H. Hietala, H. E. J. Koskinen, D. Fontaine, and L. Turc (2013), Magnetic field and dynamic pressure ULF fluctuations in coronal-mass-ejection-driven sheath regions, *Ann. Geophys.*, *31*(9), 1559–1567, doi:10.5194/angeo-31-1559-2013.

Kilpua, E. K. J., E. Lumme, K. Andreeova, A. Isavnin, and H. E. J. Koskinen (2015), Properties and drivers of fast interplanetary shocks near the orbit of the Earth (1995-2013), *J. Geophys. Res. Space Physics*, *120*(6), 4112–4125, doi:10.1002/2015JA021138.

Klein, L. W., and L. F. Burlaga (1982), Interplanetary magnetic clouds at 1 AU, *J. Geophys. Res.*, *87*(A2), 613–624, doi:10.1029/JA087iA02p00613.

Kokubun, S., R. L. McPherron, and C. T. Russell (1977), Triggering of substorms by solar wind discontinuities, *J. Geophys. Res.*, *82*(1), 74–86, doi:10.1029/JA082i001p00074.

Koval, A., and A. Szabo (2008), Modified "Rankine-Hugoniot shock fitting technique: Simultaneous solution for shock normal and speed, *J. Geophys. Res.*, *113*(A10), doi:10.1029/2008JA013337.

Koval, A., and A. Szabo (2010), Multispacecraft observations of interplanetary shock shapes on the scales of the Earth's magnetosphere, *J. Geophys. Res.*, *115*(A12105), doi:10.1029/2010JA015373.

Koval, A., J. Šafránková, Z. Němeček, L. Přech, A. A. Samsonov, and J. D. Richardson (2005), Deformation of interplanetary shock fronts in the magnetosheath, *Geophys. Res. Lett.*, *32*(15), doi:10.1029/2005GL023009.

Koval, A., J. Šafránková, Z. Němeček, A. A. Samsonov, L. Přech, and J. D. Richardson (2006), Interplanetary shock in the magnetosheath: Comparison of experimental data with MHD modeling, *Geophys. Res. Lett.*, *33*(L1102), doi:10.1029/2006GL025707.

Kruparova, O., M. Maksimovic, Šafránková, Z. Němeček, O. Santolik, and V. Krupar (2013), Automated interplanetary shock detection and its application to Wind observations, *J. Geophys. Res.*, *118*(8), 4793–4803, doi:10.1002/jgra.50468.

Lakhina, G. S., S. Alex, B. T. Tsurutani, and W. D. Gonzalez (2012), Supermagnetic storms: Hazard to society, in *Extreme Events and Natural Hazards: The Complexity Perspective*, edited by A. S. Sharma, A. Bunde, V. P. Dimri, and D. N. Baker, Geophys. Monogr. Ser. 196, American Geophysical Union, Washington, D.C., doi:10.1029/2011GM001073.

Landau, L. D., and E. M. Lifshitz (1960), *Electrodynamics of continuous media*, Pergamon Press, Oxford, England.

Lanzerotti, L. J. (1979), Geomagnetic influences on man-made systems, *J. Atmos. Sol. Terr. Phys.*, *41*(7), 787–796, doi:10.1016/0021-9169(79)90125-9.

Lee, L. C., L. Huang, and J. K. Chao (1989), On the stability of rotational discontinuities and intermediate shocks, *J. Geophys. Res.*, *94*(A7), 8813–8825, doi:10.1029/JA094iA07p08813.

Lee, M. A. (1983), Coupled hydromagnetic wave excitation and ion acceleration at interplanetary traveling shocks, *J. Geophys. Res.*, *88*(A8), 6109–6119, doi:10.1029/JA088iA08p06109.

Lehtinen, M., and R. Pirjola (1985), Currents produced in earthed conductor networks by geomagnetically-induced electric fields, *Ann. Geophys.*, *3*(4), 479–484.

Lepping, R., M. Acuña, L. Burlaga, W. Farrell, J. Slavin, K. Schatten, F. Mariani, N. Ness, F. Neubauer, Y. Whang, J. Byrnes, R. Kennon, P. Panetta, J. Scheifele, and E. Worley (1995), The WIND Magnetic Field Investigation, *Space Sci. Rev.*, *71*(1–4), 207–229, doi:10.1007/BF00751330.

Lepping, R. P., and P. D. Argentiero (1971), Single spacecraft method of estimating shock normals, *J. Geophys. Res.*, *76*(19), 4349–4359, doi:10.1029/JA076i019p04349.

Lepping, R. P., and K. W. Behannon (1986), Magnetic field directional discontinuities: Characteristics between 0.46 and 1.0 AU, *J. Geophys. Res.*, *91*(A8), 8725–8741, doi:10.1029/JA091iA08p08725.

Li, X., M. Temerin, B. T. Tsurutani, and S. Alex (2006), Modeling of 12 September 1859 super magnetic storm, *Adv. Space Res.*, *38*, 273–279, doi:10.1016/j.asr.2005.06.070.

Lin, C. C., H. Q. Feng, D. J. Wu, J. K. Chao, L. C. Lee, and L. H. Lyu (2009), Two-spacecraft observations of an interplanetary slow shock, *J. Geophys. Res.*, *114*(A3), doi:10.1029/2008JA013154.

Lindsay, G. M., C. T. Russell, J. G. Luhmann, and P. Gazis (1994), On the sources of interplanetary shocks at 0.72 AU, *J. Geophys. Res.*, *99*(A1), 11–17, doi:10.1029/93JA02666.

Liou, K., P. T. Newell, C.-I. Meng, C.-C. Wu, and R. P. Lepping (2003), Investigation of external triggering of substorms with Polar ultraviolet imager observations, *J. Geophys. Res.*, *108*(A10), doi:10.1029/2003JA009984.

Liu, J.-J., H.-Q. Hu, D.-S. Han, Z.-Y. Xing, Z.-J. Hu, D.-H. Huang, and H.-G. Yang (2013), Response of nightside aurora to interplanetary shock from ground optical observation, *Chinese J. Geophys*, *56*(5), 598–611, doi:10.1002/cjg2.20056.

Lopez, R. E., D. N. Baker, and J. Allen (2004), Sun unleashes Halloween storm, *Eos Trans. AGU*, *85*(11), 105–108, doi:10.1029/2004EO110002.

Lugaz, N., C. J. Farrugia, R. M. Winslow, N. Al-Haddad, E. K. J. Kilpua, and P. Riley (2016), Factors affecting the geo-effectiveness of shocks and sheaths at 1 AU, *J. Geophys. Res. Space Physics*, *120*(11), 10,861–10,879, doi:10.1002/2016JA023100.

Luhmann, J. G., S. C. Solomon, J. A. Linker, J. G. Lyon, Z. Mikic, D. Odstrcil, W. Wang, and M. Wiltberger (2004), Coupled model simulation of a Sun-to-Earth space weather event, *Adv. Space Res.*, *66*(15–16), 1243–1256, doi:10.1016/j.jastp.2004.04.005.

Lui, A. T. Y., A. Mankofsky, C.-L. Chang, K. Papadopoulos, and C. S. Wu (1990), A current disruption mechanism in the neutral sheet: A possible trigger for substorm expansions, *J. Geophys. Res.*, *17*(6), 745–748, doi:10.1029/GL017i006p00745.

Lyon, J. G., J. A. Fedder, and C. M. Mobarry (2004), The Lyon-Fedder-Mobarry (LFM) global MHD magnetospheric simulation code, *J. Atmos. Sol. Terr. Phys.*, *66*(15–16), 1333–1350, doi:10.1016/j.jastp.2004.03.020.

Lyons, L. R. (1995), A new theory for magnetospheric substorms, *J. Geophys. Res.*, *100*(A10), 19,069–19,081, doi:10.1029/95JA01344.

Maeda, H., K. Sakurai, T. Ondoh, and M. Yamamoto (1962), A study of solar-terrestrial relationships during the IGY and IGC, *Ann. Geophys.*, *18*, 305–333.

Manchester, W., A. Ridley, T. Gombosi, and D. DeZeeuw (2006), Modeling the Sun-to-Earth propagation of a very fast CME, *Adv. Space Res.*, *38*(2), 253–262, doi:10.1016/j.asr.2005.09.044.

Manchester IV, W. B., T. I. Gombosi, D. L. De Zeeuw, I. V. Sokolov, I. I. Roussev, K. G. Powell, J. Kóta, G. Tóth, and T. H. Zurbuchen (2005), Coronal mass ejection shock and sheath structures relevant to particle acceleration, *The Astrophysical Journal*, *622*(2), 1225–1239, doi:10.1086/427768.

Martin, B. A. (1993), Telluric effects on a buried pipeline, *CORRO-*

SION, *49*(4), 343–350, doi:10.5006/1.3316059.

McComas, D., S. Bame, P. Barker, W. Feldman, J. Phillips, P. Riley, and J. Griffee (1998), Solar Wind Electron Proton Alpha Monitor (SWEPAM) for the Advanced Composition Explorer, *Space Sci. Rev.*, *86*(1–4), 563–612, doi:10.1023/A:1005040232597.

McPherron, M. L. (1991), Physical processes producing magnetospheric substorms and magnetic storms, in *Geomagnetism, Volume 4*, edited by J. Jacobs, Academic Press Ltd., Landing, Chapter 7.

McPherron, R. L. (2015), Earth's magnetotail, in *Magnetotails in the Solar System*, edited by A. Keiling, C. M. Jackman, and P. A. Delamere, Geophys. Monogr. Ser. 207, pp. 61–84, American Geophysical Union, Washington, D.C., doi:10.1002/9781118842324.ch4.

McPherron, R. L., and D. N. Baker (1993), Factors influencing the intensity of magnetospheric substorms, *J. Atmos. Sol. Terr. Phys.*, *55*(8), 1091–1122, doi:10.1016/0021-9169(93)90040-6.

Molinski, T. S. (2002), Why utilities respect geomagnetically induced currents, *J. Atmos. Sol. Terr. Phys.*, *64*(16), 1765–1778, doi:10.1016/S1364-6826(02)00126-8.

Moretto, T., A. J. Ridley, M. J. Engebretson, and O. Rasmussen (2000), High-latitude ionospheric response to a sudden impulse event during northward IMF conditions, *J. Geophys. Res.*, *105*(A2), 2521–2531, doi:10.1029/1999JA900475.

National Research Council (NRC) (2008), Severe space weather events - Understanding societal and economic impacts: A workshop report, *Tech. rep.*, National Research Council (NRC), Washington, D.C., Available at `http://www.nap.edu/openbook.php?record_id=12507`.

Ness, N. F., C. S. Scearce, and J. B. Seek (1964), Initial results of the IMP-1 magnetic field experiment, *J. Geophys. Res.*, *69*(17), 3531–3569, doi:10.1029/JZ069i017p03531.

Neugebauer, M. (2003), In-situ measurements of the solar wind, in *Solar Wind Ten: Proceedings of the Tenth International Solar Wind Conference*, vol. 679, edited by M. Velli, R. Bruno, and F. Malara, pp. 8–13, AIP Conference Proceedings, Am. Inst. of Phys., Washington, D.C., doi:10.1063/1.1618532.

Neugebauer, M., and J. Giacalone (2005), Multispacecraft observations of interplanetary shocks: Nonplanarity and energetic particles, *J. Geophys. Res.*, *110*(A12), doi:10.1029/2005JA011380.

Neugebauer, M., and C. W. Snyder (1962), Solar plasma experiment, *Science*, *138*(3545), 1095–1097, doi:10.1126/science.138.3545.1095-a.

Newell, P. T., and J. W. Gjerloev (2011a), Evaluation of SuperMAG auroral electrojet indices as indicators of substorms and auroral power, *J. Geophys. Res.*, *116*(A12), doi:10.1029/2011JA016779.

Newell, P. T., and J. W. Gjerloev (2011b), Substorm and magnetosphere characteristic scales inferred from the SuperMAG auroral electrojet indices, *J. Geophys. Res.*, *116*(A12211), 1–12, doi:10.1029/2011JA016936.

Newell, P. T., and J. W. Gjerloev (2014), Local geomagnetic indices and the prediction of auroral power, *J. Geophys. Res. Space Physics*, *119*(12), 9790–9803, doi:10.1002/2014JA020524.

Ngwira, C. M., A. Pulkkinen, M. M. Kuznetsova, and A. Glocer (2014), Modeling extreme "Carrington-type" space weather events using three-dimensional global MHD simulations, *J. Geophys. Res. Space Physics*, doi:10.1002/2013JA019661.

Nishida, A. (1964), Transmission of storm sudden commencements through the interplanetary space; shock wave mode and non-shock mode, *Report of Ionosphere and Space Research in Japan*, *18*, 295.

Němeček, Z., J. Šafránková, A. Koval, J. Merka, and L. Přech (2011), MHD analysis of propagation of an interplanetary shock across magnetospheric boundaries, *J. Atmos. Sol. Terr. Phys.*, *73*(1), 20–29, doi:10.1016/j.jastp.2010.05.017.

Odstrčil, D. (2003), Modeling 3-D solar wind structure, *Adv. Space Res.*, *32*(4), 497–506, doi:10.1016/S0273-1177(03)00332-6.

Odstrčil, D., and V. J. Pizzo (1999), Three-dimensional propagation of coronal mass ejections (CMEs) in a structured solar wind flow: 1. CME launched within the streamer belt, *J. Geophys. Res.*, *104*(A1), 483–492, doi:10.1029/1998JA900019.

Ogilvie, K., D. Chornay, R. Fritzenreiter, F. Hunsaker, J. Keller, J. Lobell, G. Miller, J. Scudder, J. Sittler, E.C., R. Torbert, D. Bodet, G. Needell, A. Lazarus, J. Steinberg, J. Tappan, A. Mavretic, and E. Gergin (1995), SWE, a comprehensive plasma instrument for the WIND spacecraft, *Space Sci. Rev.*, *71*(1–4), 55–77, doi:10.1007/BF00751326.

Ogino, T., R. J. Walker, and M. Ashour-Abdalla (1992), A global magnetohydrodynamic simulation of the magnetosheath and magnetosphere when the interplanetary magnetic field is northward, *IEEE Trans. Plasma Sci.*, *20*(6), 817–828, doi:10.1109/27.199534.

Oh, S. Y., Y. Yi, and Y. H. Kim (2007), Solar cycle variation of the interplanetary forward shock drivers observed at 1 AU, *Solar Phys.*, *245*(2), 391–410, doi:10.1007/s11207-007-9042-2.

Oliveira, D. (2014), Ionosphere-magnetosphere coupling and field-aligned currents, *Revista Brasileira de Ensino de Física*, *36*(1), 1305, doi:10.1590/S1806-11172014000100005.

Oliveira, D. M. (2015), A study of interplanetary shock geoeffectiveness controlled by impact angles using simulations and observations, Ph.D. thesis, University of New Hampshire.

Oliveira, D. M. (2017), Magnetohydrodynamic shocks in the interplanetary space: A theoretical review, *Braz. Jour. Phys.*, *47*(1), 81–95, doi:10.1007/s13538-016-0472-x.

Oliveira, D. M., and C. M. Ngwira (2017), Geomagnetically Induced Currents: Principles, *Braz. Jour. Phys.*, *47*(5), doi:10.1007/s13538-017-0523-y.

Oliveira, D. M., and J. Raeder (2014), Impact angle control of interplanetary shock geoeffectiveness, *J. Geophys. Res. Space Physics*, *119*(10), 8188–8201, doi:10.1002/2014JA020275.

Oliveira, D. M., and J. Raeder (2015), Impact angle control of interplanetary shock geoeffectiveness: A statistical study, *J. Geophys. Res. Space Physics*, *120*(6), 4313–4323, doi:10.1002/2015JA021147.

Oliveira, D. M., and M. V. D. Silveira (2016), Space weather and interplanetary shocks, *Revista Brasileira de Ensino de Física*, *38*(1), 1–18, doi:10.1590/S1806-11173812083.

Oliveira, D. M., and M. V. D. Silveira (2017), Thermosphere response to geomagnetic storms, *Revista Brasileira de Ensino de Física*, *39*(3), e3305, doi:10.1590/1806-9126-RBEF-2016-0219.

Oliveira, D. M., J. Raeder, B. T. Tsurutani, and J. W. Gjerloev (2016), Effects of interplanetary shock inclinations on nightside auroral power intensity, *Braz. Jour. Phys.*, *46*(1), 97–104, doi:10.1007/s13538-015-0389-9.

Oliveira, D. M., E. Zesta, P. W. Schuck, H. K. Connor, and E. K. Sutton (2017), Ionosphere-thermosphere global time response to geomagnetic storms, in *Proceedings of the 15$^{\text{th}}$ International Ionospheric Effects Symposium*, edited by K. M. Groves and M. S. Magoun, Alexandria, VA.

Ondoh, T. (1963), Longitudinal distribution of ssc rise time, *J. Geomagn. Geoelectr.*, *14*(4), 198–207, doi:10.5636/jgg.14.198.

Oughton, E. J., A. Skelton, R. B. Horne, A. W. P. Thomson, and C. T. Gaunt (2017), Quantifying the daily economic impact of extreme space weather due to failure in electricity transmission infrastructure, *Space Weather*, *15*(1), 65–83, doi:10.1002/2016SW001491.

Pallocchia, G. (2013), A sunward propagating fast wave in the magnetosheath observed after the passage of an interplanetary shock, *J. Geophys. Res.*, *118*(1), 331–339, doi:10.1029/2012JA017851.

Pallocchia, G., A. A. Samsonov, M. B. Bavassano-Cattaneo, M. F. Marcucci, H. Rme, C. M. Carr, and J. B. Cao (2010), Interplanetary shock transmitted into the Earth's magnetosheath: Cluster and Double Star observations, *Ann. Geophys.*, *28*(5), 1141–1156, doi:10.5194/angeo-28-1141-2010.

Palmerio, E., E. K. J. Kilpua, and N. P. Savani (2016), Planar magnetic structures in coronal mass ejection-driven sheath regions, *Ann. Geophys.*, *34*(2), 313–322, doi:10.5194/angeo-34-313-2016.

Parker, E. N. (1958), Superthermal particle generation on the solar corona, *The Astrophysical Journal*, *128*, 677–685, doi:10.1086/146580.

Parker, E. N. (1961), Sudden expansion of the corona following a large solar flare and the attendant magnetic field and cosmic ray effects, *The Astrophysical Journal*, *133*, 1014–1033, doi:10.1086/147105.

Parker, E. N. (1999), Space Physics before the Space Age, in *The Solar Wind Nine Conference*, vol. 471, edited by S. R. Habbal and C. D. Halas, AIP Conference Proceedings, Am. Inst. of Phys., Washington, D.C., doi:10.1063/1.58782.

Paschmann, G., Schwartz, S., C. Escoubet, and S. Haaland (Eds.) (2005), *Outer Magnetospheric Boundaries: Cluster Results*, vol. 20, Springer Netherlands, Amsterdam, The Netherlands, doi:10.1007/1-4020-4582-4.

Patel, V., and L. Cahill (1974), Magnetic field variations of the SI in the magnetosphere and correlated effects in interplanetary space, *Planet. Space Sci.*, *22*(7), 1117–1129, doi:10.1016/0032-0633(74)90066-X.

Patel, V. L. (1968), Sudden impulses in the geomagnetotail, *J. Geophys. Res.*, *73*(11), 3407–3419, doi:10.1029/JA073i011p03407.

Perreault, P., and S.-I. Akasofu (1978), A study of geomagnetic storms, *Geophys. J. Roy. Astron. Soc.*, *54*(3), 547–573, doi:10.1111/j.1365-246X.1978.tb05494.x.

Pesnell, W. D. (2015), Predictions of solar cycle 24: How are we doing?, *Space Weather*, doi:10.1002/2015SW001304.

Pesses, M. E., B. T. Tsurutani, J. A. Van Allen, and E. J. Smith (1979), Acceleration of energetic protons by interplanetary shocks, *J. Geophys. Res.*, *84*(A12), 7297–7301, doi:10.1029/JA084iA12p07297.

Petschek, H. E. (1958), Aerodynamic dissipation, *Rev. Mod. Phys.*, *30*, 966–974, doi:10.1103/RevModPhys.30.966.

Pirjola, R. (2012), Geomagnetically induced currents as ground effects of space weather, in *Space Science*, edited by H. J. M. Cuesta, pp. 27–44, InTech, Rijeka, Croatia, doi:10.5772/29840.

Pizzo, V. J. (1991), The evolution of corotating stream fronts near the ecliptic plane in the inner solar system: 2. Three-dimensional tilted-dipole fronts, *J. Geophys. Res.*, *96*(A4), 5405–5420, doi:10.1029/91JA00155.

Powell, K. G., P. L. Roe, T. J. Linde, T. I. Gombosi, and D. L. De Zeeuw (1999), A solution-adaptive upwind scheme for ideal magnetohydrodynamics, *Journal of Computational Physics*, *154*(2), 284–309, doi:10.1006/jcph.1999.6299.

Priest, E. F. (1981), *Solar Magnetohydrodynamics*, D. Reidel Publishing, Dordrecht, Holland.

Pudovkin, M. (1991), Physics of magnetospheric substorms: A review, in *Magnetospheric Substorms*, edited by J. R. Kan, S. K. T. A. Potemr and, and T. Iijima, Geophys. Monogr. Ser. 64, pp. 17–27, American Geophysical Union, Washington, D.C., doi:10.1029/GM064p0017.

Pulkkinen, A., K. Kuznetsova, A. Ridley, J. Raeder, A. Vapirev, D. Weimer, R. S. Weigel, M. Wiltberger, G. Millward, L. Rastätter, M. Hesse, H. J. Singer, and A. Chulaki (2011), Geospace environment modeling 2008-2009 challenge: Ground magnetic field perturbations, *J. Geophys. Res.*, *9*, doi:10.1029/2010SW000600.

Pulkkinen, A., L. Rastatter, M. Kuznetsova, H. Singer, C. Balch, D. Weimer, G. Tóth, A. Ridley, T. Gombosi, M. Wiltberger, J. Raeder, and R. Weigel (2013), Community-wide validation of geospace model ground magnetic field perturbation predictions to support model transition to operations, *Space Weather*, *11*, 369, doi:10.1002/swe.20056.

Raeder, J. (2003), Global Magnetohydrodynamics: A Tutorial Review, in *Space Plasma Simulation*, edited by J. Buchner, C. T. Dum, and M. Scholer, pp. 1–20, Springer Verlag, Berlin Heilderberg, New York, doi:10.1007/3-540-36530-3_11.

Raeder, J., J. Berchem, and M. Ashour-Abdalla (1998), The Geospace Environment Modeling Grand Challenge: Results from a Global Geospace Circulation Model, *J. Geophys. Res.*, *103*(A7), doi:10.1029/98JA00014.

Raeder, J., Y. Wang, and T. J. Fuller-Rowell (2001a), Geomagnetic storm simulation with a Coupled Magnetosphere-Ionosphere-Thermosphere model, in *Space Weather*, edited by P. Song and H. J. Siscoe, Geophys. Monogr. Ser. 125, pp. 377–384, American Geophysical Union, Washington, D.C., doi:10.1029/GM125p0377.

Raeder, J., R. L. McPherron, L. A. Frank, S. Kokubun, G. Lu, T. Mukai, W. R. Paterson, J. B. Sigwarth, H. J. Singer, and J. A. Slavin (2001b), Global simulation of the Geospace Environment Modeling substorm challenge event, *J. Geophys. Res.*, *106*(A1), 381–395, doi:10.1029/2000JA000605.

Rastätter, L., M. M. Kuznetsova, A. Glocer, D. Welling, X. Meng, J. Raeder, M. Wiltberger, V. K. Jordanova, Y. Yu, S. Zaharia, R. S. Weigel, S. Sazykin, R. Boynton, H. Wei, V. Eccles, W. Horton, M. L. Mays, and J. Gannon (2013), Geospace Environment Modeling 2008-2009 challenge: Dst index, *Space Weather*, *11*, 187, doi:10.1002/swe.20036.

Reames, D. V. (1999), Particle acceleration at the sun and in the heliosphere, *Space Sci. Rev.*, *9*(3), 413–491, doi:10.1023/A:1005105831781.

Reddy, C. A. (1989), The equatorial electroject, *Pure Appl. Geophys.*, *132*(3), 485–508, doi:10.1007/BF00876841.

Richardson, I. G., and H. V. Cane (2010), Interplanetary circumstances of quasi-perpendicular interplanetary shocks in 1996-2005, *J. Geophys. Res.*, *115*(A7), doi:10.1029/2009JA015039.

Richter, A. K., K. C. Hsieh, A. H. Luttrell, E. Marsch, and R. Schwenn (1985), Review of interplanetary shock phenomena near and within 1 AU, in *Collisionless Shocks in the Heliosphere: Reviews of Current Research*, edited by B. T. Tsurutani and R. G. Stone, Geophys. Monogr. Ser. 35, pp. 33–50, American Geophysical Union, Washington, D.C., doi:10.1029/GM035p0033.

Ridley, A. J., T. I. Gombosi, and D. L. DeZeeuw (2004), Ionospheric control of the magnetosphere: conductance, *Ann. Geophys.*, *22*(2), 567–584, doi:10.5194/angeo-22-567-2004.

Ridley, A. J., D. L. De Zeeuw, W. B. Manchester, and K. C. Hansen (2006), The magnetospheric and ionospheric response to a very strong interplanetary shock and coronal mass ejection, *Adv. Space Res.*, *38*, 263–272, doi:10.1016/j.asr.2006.06.010.

Riley, P., R. M. Kaplan, J. Giacalone, D. Lario, and Y. Liu (2016), Properties of the fast forward shock driven by the 2012 july 23 extreme coronal mass ejection, *The Astrophysical Journal*, *819*(1), 1–11, doi:10.3847/0004-637X/819/1/57.

Rostoker, G. (1972), Geomagnetic indices, *Rev. Geophys.*, *10*(4), 935–950, doi:10.1029/RG010i004p00935.

Rostoker, G., E. Friedrich, and M. Dobbs (1997), Physics of magnetic storms, in *Magnetic Storms*, edited by B. T. Tsurutani, W. D. Gonzalez, Y. Kamide, and J. K. Arballo, Geophys. Monogr. Ser. 98, pp. 149–160, American Geophysical Union, Washington, D.C., doi:10.1029/GM098p0149.

Russell, C. T. (1984), Reconnection at the Earth's magnetopause: Magnetic field observations and flux transfer events, in *Magnetic Reconnection in Space and Laboratory Plasmas*, edited by E. W. Hones Jr., Geophys. Monogr. Ser. 30, pp. 124–138, American Geophysical Union, Washington, D.C., doi:10.1029/GM030p0124.

Russell, C. T., and C. J. Alexander (1984), Multiple spacecraft observations of interplanetary shocks: Shock-normal oscillations and their effects, *Adv. Space Res.*, *4*(2-3), 277–282, doi:10.1016/0273-1177(84)90321-1.

Russell, C. T., J. T. Gosling, R. D. Zwickl, and E. J. Smith (1983a), Multiple spacecraft observations of interplanetary shocks: ISEE three-dimensional plasma measurements, *J. Geophys. Res.*, *88*(A12), 9941–9947, doi:10.1029/JA088iA12p09941.

Russell, C. T., M. M. Mellott, E. J. Smith, and J. H. King (1983b), Multiple spacecraft observations of interplanetary shocks: Four spacecraft determination of shock normals, *J. Geophys. Res.*, *88*(A6), 4739–4748, doi:10.1029/JA088iA06p04739.

Russell, C. T., M. Ginskey, and S. M. Petrinec (1994a), Sudden impulses at low-latitude stations: Steady state response for northward interplanetary magnetic field, *J. Geophys. Res.*, *99*(A1), 253–261, doi:10.1029/93JA02288.

Russell, C. T., M. Ginskey, and S. M. Petrinec (1994b), Sudden impulses at low-latitude stations: Steady state response for southward interplanetary magnetic field, *J. Geophys. Res.*, *99*(A7), 13,403–13,408, doi:10.1029/94JA00549.

Russell, C. T., Y. L. Wang, J. Raeder, R. L. Tokar, C. W. Smith, K. W. Ogivie, A. J. Lazarus, R. P. Lepping, A. Szabo, H. Kawano, T. Mukai, S. Savin, Y. L. Yermolaev, X. Zhou, and B. T. Tsurutani (2000), The interplanetary shock of September 24, 1998: Arrival at Earth, *J. Geophys. Res.*, *105*(A1), 25,143–25,154, doi:10.1029/2000JA900070.

Russell, C. T., J. G. Luhmann, and L. K. Jian (2010), How unprecedented a solar minimum?, *Rev. Geophys.*, *48*(2), doi:10.1029/2009RG000316.

Šafránková, J., Z. Němeček, L. Přech, A. Samsonov, A. Koval, and K. Andréeovaá (2007a), Interaction of interplanetary shocks with the bow shock, *Planet. Space Sci.*, *55*(15), 2324–2329, doi:10.1016/j.pss.2007.05.012.

Šafránková, J., Z. Němeček, L. Přech, A. A. Samsonov, and K. Koval, A. andAndréeovaá (2007b), Modification of interplanetary shocks near the bow shock and through the magnetosheath, *J. Geophys. Res.*, *112*(A8), doi:10.1029/2007JA012503.

Samson, J. C., D. D. Wallis, T. J. Hughes, F. Creutzberg, J. M. Ruohoniemi, and R. A. Greenwald (1992), Substorm intensifications and field line resonances in the nightside magnetosphere, *J. Geophys. Res.*, *97*(A6), 8495–8518, doi:10.1029/91JA03156.

Samsonov, A. A. (2011), Propagation of inclined interplanetary shock through the magnetosheath, *J. Atmos. Sol. Terr. Phys.*, *73*, 1–9, doi:10.1016/j.jastp.2009.10.014.

Samsonov, A. A., and D. G. Sibeck (2013), Large-scale flow vortices following a magnetospheric sudden impulse, *J. Geophys. Res.*, *118*(6), 3055–3064, doi:10.1002/jgra.50329.

Samsonov, A. A., Z. Němeček, and J. Šafránková (2006), Numerical MHD modeling of propagation of interplanetary shock through the magnetosheath, *J. Geophys. Res.*, *111*(A082), doi:10.1029/2005JA011537.

Samsonov, A. A., D. G. Sibeck, and J. Imber (2007), MHD simulation for the interaction of an interplanetary shock with the Earth's magnetosphere, *J. Geophys. Res.*, *112*(A12220), 1–9, doi:10.1029/2007JA012627.

Samsonov, A. A., D. G. Sibeck, and Y. Yu (2010), Transient changes in magnetospheric-ionospheric current caused by the passage of an interplanetary shock: Northward interplanetary magnetic field case, *J. Geophys. Res.*, *115*(A05207), doi:doi:10.1029/2009JA014751.

Samsonov, A. A., D. G. Sibeck, N. V. Zolotova, H. K. Biernat, S.-H. Chen, L. Rastätter, H. J. Singer, and W. Baumjohann (2011), Propagation of a sudden impulse through the magnetosphere initiating magnetospheric Pc5 pulsations, *J. Geophys. Res.*, *116*(A10), doi:10.1029/2011JA016706.

Samsonov, A. A., D. G. Sibeck, B. M. Walsh, and N. V. Zolotova (2014), Sudden impulse observations in the dayside magnetosphere by THEMIS, *J. Geophys. Res. Space Physics*, *119*(12), doi:10.1002/2014JA020012.

Samsonov, A. A., V. A. Sergeev, M. M. Kuznetsova, and D. G. Sibeck (2015), Asymmetric magnetospheric compressions and expansions in response to impact of inclined interplanetary shock, *Geophys. Res. Lett.*, *42*(12), 4716–4722, doi:10.1002/2015GL064294.

Samsonov, A. A., E. Gordeev, N. A. Tsyganenko, J. Šafránková, Z. Němeček, J. Šimůnek, D. G. Sibeck, G. Tóth, V. G. Merkin, and J. Raeder (2016), Do we know the actual magnetopause position for typical solar wind conditions?, *J. Geophys. Res. Space Physics*, *121*(7), 6493–6508, doi:10.1002/2016JA022471.

Schieldge, J., and G. Siscoe (1970), A correlation of the occurrence of simultaneous sudden magnetospheric compressions and geomagnetic bay onsets with selected geophysical indices, *J. Atmos. Sol. Terr. Phys.*, *32*(11), 1819–1830, doi:10.1016/0021-9169(70)90139-X.

Schrijver, C. J., R. Dobbins, W. Murtagh, and S. M. Petrinec (2014), Assessing the impact of space weather on the electric power grid based on insurance claims for industrial electrical equipment, *Space Weather*, doi:10.1002/2014SW001066.

Schwartz, S. J. (1998), Shock and discontinuity normals, Mach numbers, and related parameters, in *Analysis Methods for Multi-Spacecraft Data*, edited by G. Paschmann and I. S. R. P. W. Daly, ESA Publications Division, Netherlands.

Sckopke, N. (1966), A general relation between the energy of trapped particles and the disturbance field near the Earth, *J. Geophys. Res.*, *71*(13), 3125–3130, doi:10.1029/JZ071i013p03125.

Selvakumaran, R., B. Veenadhari, Y. Ebihara, S. Kumar, and D. S. V. V. D. Prasad (2017), The role of interplanetary shock orientation on SC/SI rise time and geoeffectiveness, *Adv. Space Res.*, *59*(5), 1425–1434, doi:10.1016/j.asr.2016.12.010.

Shen, W.-W., and M. Dryer (1972), Magnetohydrodynamic theory for the interaction of an interplanetary double-shock ensemble with the earth's bow shock, *J. Geophys. Res.*, *77*(25), 4627–4644, doi:10.1029/JA077i025p04627.

Shi, Y., E. Zesta, H. K. Connor, Y.-J. Su, E. K. Sutton, C. Y. Huang, D. M. Ober, C. Christodoulo, S. Delay, and D. M. Oliveira (2017), High-latitude thermosphere neutral density response to solar wind dynamic pressure enhancement, *J. Geophys. Res. Space Physics*, submitted.

Singh, A., V. Rathore, R. P. Singh, and A. K. Singh (2017), Source identification of moderate (-100 nT $<$ Dst $<$ -50 nT) and intense geomagnetic storms (Dst $<$ -100 nT) during ascending phase of solar cycle 24, *Adv. Space Res.*, *59*(1), 1209–1222, doi:10.1016/j.asr.2016.12.006.

Slinker, S. P., J. A. Fedder, W. J. Hughes, and J. G. Lyon (1999), Response of the ionosphere to a density pulse in the solar wind: Simulation of traveling convection vortices, *Geophys. Res. Lett.*, *26*(23), 3549–3552, doi:10.1029/1999GL010688.

Smith, C., J. L'Heureux, N. Ness, M. Acuña, L. Burlaga, and J. Scheifele (1998), The ACE magnetic fields experiment, *Space Sci. Rev.*, *86*(1–4), 613–632, doi:10.1023/A:1005092216668.

Smith, E. J. (1973), Identification of interplanetary tangential and rotational discontinuities, *J. Geophys. Res.*, *78*(13), 2054–2063, doi:10.1029/JA078i013p02054.

Smith, E. J. (1985), Interplanetary shock phenomena beyond 1 AU, in *Collisionless Shocks in the Heliosphere: Reviews of Current Research*, edited by B. T. Tsurutani and R. G. Stone, Geophys. Monogr. Ser. 35, pp. 69–83, American Geophysical Union, Washington, D.C., doi:10.1029/GM035p0069.

Smith, E. J., and J. H. Wolfe (1976), Observations of interaction regions and corotating shocks between one and five AU: Pioneers 10 and 11, *Geophys. Res. Lett.*, *3*(3), 137–140, doi:10.1029/GL003i003p00137.

Smith, E. J., J. A. Slavin, B. T. Tsurutani, W. C. Feldman, and S. J. Bame (1984), Slow mode shocks in the Earth's magnetotail: ISEE-3, *Geophys. Res. Lett.*, *11*(10), 1054–1057, doi:10.1029/GL011i010p01054.

Smith, E. J., J. A. Slavin, R. D. Zwickl, and S. J. Bame (1986), Shocks and storm sudden commencements, in *Solar Wind and Magnetosphere Coupling*, edited by Y. Kamide and J. A. Slavin, p. 345, Terra Scientific, Tokyo, Japan.

Sonett, C. P., D. S. Colburn, L. Davis, E. J. Smith, and P. J. Coleman (1964), Evidence for a collision-free magnetohydrodynamic shock in interplanetary space, *Phys. Rev. Lett.*, *13*, 153–156, doi:10.1103/PhysRevLett.13.153.

Spreiter, J. R., A. L. Summers, and A. Y. Alksne (1966), Hydromagnetic flow around the magnetosphere, *Planet. Space Sci.*, *14*(3), 223–253, doi:10.1016/0032-0633(66)90124-3.

Stone, R. G., and B. T. Tsurutani (Eds.) (1985), *Collisionless Shocks in the Heliosphere: A Tutorial Review, Geophys. Monogr. Ser.*, vol. 34, American Geophysical Union, Washington, D.C., doi:10.1029/GM034.

Sugiura, M. (1964), Hourly values of equatorial Dst for the IGY, *Ann. Int. Geophys. Year*, *35*(5).

Sugiura, M., T. L. Skillman, B. G. Ledley, and J. P. Heppner (1968), Propagation of the sudden commencement of july 8, 1966, to the magnetotail, *J. Geophys. Res.*, *73*(21), 6699–6709, doi:10.1029/JA073i021p06699.

Szabo, A. (1994), An improved solution to the "Rankine-Hugoniot" problem, *J. Geophys. Res.*, *99*(A8), 14,737–14,746, doi:10.1029/94JA00782.

Szabo, A. (2005), Multi-spacecraft observations of interplanetary shocks, in *4th Annual IGPP International Astrophysics Conference on the Physics of Collisionless Shocks*, edited by G. Li, G. Zank, and C. T. Russell, pp. 37–41, AIP Conference Proceedings, Am. Inst. of Phys., Washington, D.C., doi:10.1063/1.2032672.

Takao, S., and S. Matsushtta (1967), Geomagnetic pulsations associated with sudden commencements and sudden impulses, *Planet. Space Sci.*, *15*(3), 573–587, doi:10.1016/0032-0633(67)90163-8.

Takeuchi, T., C. T. Russell, and T. Araki (2002), Effect of the orientation of interplanetary shock on the geomagnetic sudden commencement, *J. Geophys. Res.*, *107*(A12), 1423, doi:10.1029/2002JA009597.

Tamao, T. (1964a), The structure of three-dimensional hydromagnetic waves in a uniform cold plasma, *J. Geomagn. Geoelectr.*, *18*, 89–114.

Tamao, T. (1964b), A hydromagnetic interpretation of geomagnetic SSC*, *Rept. Ionosphere Space Res. Japan*, *18*, 16–31.

Tanaka, T. (1994), Finite volume TVD scheme on an unstructured grid system for three-dimensional MHD simulation of inhomogeneous systems including strong background potential fields, *Journal of Computational Physics*, *111*(2), 381–389, doi:10.1006/jcph.1994.1071.

Thomsen, M. F. (1988), Multi–spacecraft observations of collisionless shocks, *Adv. Space Res.*, *8*(9–10), 157–166, doi:10.1016/0273-1177(88)90126-3.

Toptyghin, I. N. (1980), Acceleration of particles by shocks in a cosmic plasma, *Space Sci. Rev.*, *26*(2), 157–213, doi:10.1007/BF00167370.

Tóth, G. (2000), The $\nabla \cdot \mathbf{B}$ constraint in shock-capturing magnetohydrodynamics codes, *Journal of Computational Physics*, *161*(2), 605–652, doi:10.1006/jcph.2000.6519.

Tóth, G., I. V. Sokolov, T. I. Gombosi, D. R. Chesney, C. R. Clauer, D. L. De Zeeuw, K. C. Hansen, K. J. Kane, W. B. Manchester, R. C. Oehmke, K. G. Powell, A. J. Ridley, I. I. Roussev, Q. F. Stout, O. Volberg, R. A. Wolf, S. Sazykin, A. Chan, B. Yu, and J. Kóta (2005), Space Weather Modeling Framework: A new tool for the space science community, *J. Geophys. Res.*, *110*(A12), doi:10.1029/2005JA011126.

Tóth, G., D. L. De Zeeuw, T. I. Gombosi, W. B. Manchester, A. J. Ridley, I. V. Sokolov, and I. I. Roussev (2007), Sun-to-thermosphere simulation of the 28–30 October 2003 storm with the Space Weather Modeling Framework, *Space Weather*, *5*(6), 1–16, doi:10.1029/2006SW000272.

Tsai, T. C., L. H. Lyu, J. K. Chao, M. Q. Chen, and W. H. Tsai (2009), A theoretical and simulation study of the contact discontinuities based on a vlasov simulation code, *J. Geophys. Res.*, *114*(A12), doi:10.1029/2009JA014121.

Tsurutani, B., W. D. Gonzalez, G. S. Lakhina, and S. Alex (2003), The extreme magnetic storm of 1-2 september 1859, *J. Geophys. Res.*, *108*(A7), doi:10.1029/2002JA009504.

Tsurutani, B., E. Echer, F. L. Guarnieri, and O. P. Verkhoglyadova (2008), Interplanetary causes of middle latitude ionospheric disturbances, in *Midlatitude Ionospheric Dynamics and Disturbances*, Geophys. Monogr. Ser., pp. 99–119, American Geophysical Union, Washington, D.C., doi:0.1029/GM181.

Tsurutani, B., G. Lakhina, O. Verkhoglyadova, W. Gonzalez, E. Echer, and F. Guarnieri (2011), A review of interplanetary discontinuities and their geomagnetic effects, *J. Atmos. Sol. Terr. Phys.*, *73*(1), 5–19, doi:10.1016/j.jastp.2010.04.001.

Tsurutani, B. T. (2001), The interplanetary causes of magnetic storms, substorms and geomagnetic quiet, in *Space Storms and Space Weather Hazards*, edited by I. A. Daglis, NATO Science Series (Series II: Mathematics, Physics and Chemistry), vol 38, Springer, Dordrecht, Holland, doi:10.1007/978-94-010-0983-6_4.

Tsurutani, B. T., and G. S. Lakhina (2014), An extreme coronal mass ejection and consequences for the magnetosphere and Earth, *Geophys. Res. Lett.*, *41*, 287–292, doi:10.1002/2013GL058825.

Tsurutani, B. T., and R. P. Lin (1985), Acceleration of >47 keV ions and >2 keV electrons by interplanetary shocks at 1 AU, *J. Geophys. Res.*, *90*(A1), 1–11, doi:10.1029/JA090iA01p00001.

Tsurutani, B. T., and C.-I. Meng (1972), Interplanetary magnetic-field variations and substorm activity, *J. Geophys. Res.*, *77*(16), 2964–2970, doi:10.1029/JA077i016p02964.

Tsurutani, B. T., and P. Rodriguez (1981), Upstream waves and particles: An overview of ISEE results, *J. Geophys. Res.*, *86*(A6), 4317–4324, doi:10.1029/JA086iA06p04317.

Tsurutani, B. T., and E. J. Smith (1979), Interplanetary discontinuities: Temporal variations and the radial gradient from 1 to 8.5 AU, *J. Geophys. Res.*, *84*(A6), 2773–2787, doi:10.1029/JA084iA06p02773.

Tsurutani, B. T., and R. G. Stone (Eds.) (1985), *Collisionless Shocks in the Heliosphere: Reviews of Current Research*, *Geophys. Monogr. Ser.*, vol. 35, American Geophysical Union, Washington, D.C., doi:10.1029/GM035.

Tsurutani, B. T., and X. Y. Zhou (2003), Interplanetary shock triggering of substorms: Wind and Polar, *Adv. Space Res.*, *31*(4), 1063–1067, doi:10.1016/S0273-1177(02)00796-2.

Tsurutani, B. T., E. J. Smith, K. R. Pyle, and J. A. Simpson (1982), Energetic protons accelerated at corotating shocks: Pioneer 10 and 11 observations from 1 to 6 AU, *J. Geophys. Res.*, *87*(A9), 7389–7404, doi:10.1029/JA087iA09p07389.

Tsurutani, B. T., E. J. Smith, and D. E. Jones (1983), Waves observed upstream of interplanetary shocks, *J. Geophys. Res.*, *88*(A7), 5645–5656, doi:10.1029/JA088iA07p05645.

Tsurutani, B. T., W. D. Gonzalez, F. Tang, and Y. T. Lee (1992), Great magnetic storms, *Geophys. Res. Lett.*, *19*(1), 73–76, doi:10.1029/91GL02783.

Tsurutani, B. T., G. S. Lakhina, J. S. Pickett, F. L. Guarnieri, N. Lin, and B. E. Goldstein (2005), Nonlinear alfvén waves, discontinuities, proton perpendicular acceleration, and magnetic holes/decreases in interplanetary space and the magnetosphere: intermediate shocks?, *Nonlin. Processes Geophys.*, *12*(3), 321–336, doi:10.5194/npg-12-321-2005.

Tsurutani, B. T., W. D. Gonzalez, A. L. C. Gonzalez, F. L. Guarnieri, N. Gopalswamy, M. Grande, Y. Kamide, Y. Kasahara, G. Lu, I. Mann, R. McPherron, F. Soraas, and V. Vasyliūnas (2006), Corotating solar wind streams and recurrent geomagnetic activity: A review, *J. Geophys. Res.*, *111*(A7), 1–25, doi:10.1029/2005JA011273.

Tsurutani, B. T., E. Echer, K. Shibata, O. P. Verkhoglyadova, A. J. Mannucci, W. D. Gonzalez, J. U. Kozyra, and M. Pätzold (2014), The interplanetary causes of geomagnetic activity during the 7-17 March 2012 interval: A CAWSES II overview, *J. Space Weather Space Clim.*, *4*(A02), doi:10.1051/swsc/2013056.

Tylka, A. J., and M. A. Lee (2006), A model for spectral and compositional variability at high energies in large, gradual solar particle events, *The Astrophysical Journal*, *646*(2), 1319–1334, doi:10.1086/505106.

Viljanen, A., A. Pulkkinen, R. Pirjola, K. Pajunpää, P. Posio, and A. Koistinen (2006), Recordings of geomagnetically induced currents and a nowcasting service of the Finnish natural gas pipeline system, *Space Weather*, *4*(10), doi:10.1029/2006SW000234.

Viñas, A. F., and J. D. Scudder (1986), Fast and optimal solution to the "Rankine-Hugoniot" problem, *J. Geophys. Res.*, *91*(A1), 39–58, doi:10.1029/JA091iA01p00039.

Wang, C., Z. H. Huang, Y. Q. Hu, and X. C. Guo (2005), 3D global simulation of the interaction of interplanetary shocks with the magnetosphere, in *4th Annual IGPP International Astrophysics Conference on the Physics of Collisionless Shocks*, vol. 781, edited by G. Li, G. Zank, and C. T. Russell, pp. 320–324, AIP Conference Proceedings, Am. Inst. of Phys., Washington, D.C., doi:10.1063/1.2032716.

Wang, C., C. X. Li, Z. H. Huang, and J. D. Richardson (2006), Effect of interplanetary shock strengths and orientations on storm sudden commencement rise times, *Geophys. Res. Lett.*, *33*(L14104), 1–3, doi:10.1029/2006GL025966.

Wang, C., J. B. Liu, H. Li, Z. H. Huang, J. D. Richardson, and J. R. Kan (2009), Geospace magnetic field responses to interplanetary shocks, *J. Geophys. Res.*, *114*(A5), doi:10.1029/2008JA013794.

Wang, C., X. G. H. Li, K. Ding, and Z. Huang (2012), Numerical study on the response of the Earth's magnetosphere-ionosphere system to a super solar storm, *Science China: Earth Sciences*, *55*(6), 1037, doi:10.1007/s11430-012-4405-4.

Wang, C., X.-C. Guo, Z. Peng, B.-B. Tang, T.-R. Sun, W.-Y. Li, and Y.-Q. Hu (2013), Magnetohydrodynamics (MHD) numerical simulations on the interaction of the solar wind with the magnetosphere: A review., *Science China: Earth Sciences*, *56*, 1141–1157, doi:10.1007/s11430-013-4608-3.

Webb, D. F., and T. A. Howard (2012), Coronal mass ejections: Observations, *Living Rev. in Solar Phys.*, *9*(3), doi:10.12942/lrsp-

2012-3.
Whang, Y. C. (1982), Slow shocks around the Sun, *Geophys. Res. Lett.*, *9*(9), 1081–1084, doi:10.1029/GL009i009p01081.
Whang, Y. C., J. Zhou, R. P. Lepping, and K. W. Ogilvie (1996), Interplanetary slow shock observed from WIND, *Geophys. Res. Lett.*, *23*(10), 1239–1242, doi:10.1029/96GL01358.
Wilken, B., C. K. Goertz, D. N. Baker, P. R. Higbie, and T. A. Fritz (1982), The SSC on July 29, 1977 and its propagation within the magnetosphere, *J. Geophys. Res.*, *87*(A8), 5901–5910, doi:10.1029/JA087iA08p05901.
Wu, C. C. (1988), Effects of dissipation on rotational discontinuities, *J. Geophys. Res.*, *93*(A5), 3969–3982, doi:10.1029/JA093iA05p03969.
Wu, C. C. (1990), Formation, structure, and stability of MHD intermediate shocks, *J. Geophys. Res.*, *95*(A6), 8149–8175, doi:10.1029/JA095iA06p08149.
Yan, M., and L. C. Lee (1996), Interaction of interplanetary shocks and rotational discontinuities with the Earth's bow shock, *J. Geophys. Res.*, *101*(A3), 4835–4848, doi:10.1029/95JA02976.
Yizengaw, E., E. Zesta, M. B. Moldwin, B. Damtie, A. Mebrahtu, C. E. Valladares, and R. F. Pfaff (2012), Longitudinal differences of ionospheric vertical density distribution and equatorial electrodynamics, *J. Geophys. Res.*, *117*(A7), doi:10.1029/2011JA017454.
Yue, C., Q. G. Zong, H. Zhang, Y. F. Wang, C. J. Yuan, Z. Y. Pu, S. Y. Fu, A. T. Y. Lui, B. Yang, and C. R. Wang (2010), Geomagnetic activity triggered by interplanetary shocks, *J. Geophys. Res.*, *115*(A00I05), 1–13, doi:10.1029/2010JA015356.
Zesta, E., H. J. Singer, D. Lummerzheim, C. T. Russell, L. R. Lyons, and M. J. Brittnacher (2000), The effect of the January 10, 1997, pressure pulse on the magnetosphere–ionosphere current system, in *Magnetospheric Current Systems*, edited by S.-I. Ohtani, R. Fujii, M. Hesse, and R. L. Lysak, Geophys. Monogr. Ser. 118, pp. 217–226, American Geophysical Union, Washington, D.C., doi:10.1029/GM118p0217.
Zhou, X., and B. T. Tsurutani (2001), Interplanetary shock triggering of nightside geomagnetic activity: Substorms, pseudobreakups, and quiescent events, *J. Geophys. Res.*, *106*(A9), 18,957–18,967, doi:10.1029/2000JA003028.
Zhou, X.-Y., and B. T. Tsurutani (1999), Rapid intensification and propagation of the dayside aurora: Large scale interplanetary pressure pulses (fast shocks), *Geophys. Res. Lett.*, *26*(8), 1097–1100, doi:10.1029/1999GL900173.
Zong, Q.-G., X.-Z. Zhou, Y. F. Wang, X. Li, P. Song, D. N. Baker, T. A. Fritz, P. W. Daly, M. Dunlop, and A. Pedersen (2009), Energetic electron response to ULF waves induced by interplanetary shocks in the outer radiation belt, *J. Geophys. Res.*, *114*(A10204), 1–13, doi:10.1029/2009JA014393.

List of changes